NASA CONTRACTOR REPORT

NASA CR-1323

EXPERIMENTAL INVESTIGATION IN AN ANNULAR CASCADE SECTOR OF HIGHLY LOADED TURBINE STATOR BLADING

Volume II. Performance of Plain Blade and Effect of Vortex Generators

by James L. Bettner

EXPERIMENTAL INVESTIGATION IN AN ANNULAR CASCADE SECTOR

OF HIGHLY LOADED TURBINE STATOR BLADING

Volume II.   Performance of Plain Blade and Effect of Vortex Generators

By James L. Bettner

Distribution of this report is provided in the interest of information exchange.   Responsibility for the contents resides in the author or organization that prepared it.

FOREWORD

The research described herein, which was conducted by the Allison Division of General Motors, was performed under NASA Contract NAS3-9494. The work was done under the technical management of Mr. Edward L. Warren and Mr. Stanley M. Nosek, Airbreathing Engines Division and Fluid System Components Division, respectively, NASA-Lewis Research Center. The report was originally issued as Allison EDR 5315, Volume II, October 1968.

TABLE OF CONTENTS

LIST OF TABLES

LIST OF ILLUSTRATIONS

Figure	Title	Page

EXPERIMENTAL INVESTIGATION IN AN ANNULAR CASCADE SECTOR

OF HIGHLY LOADED TURBINE STATOR BLADING

Volume II. Performance of Plain Blade and Effect of Vortex Generators

by

J. L. Bettner
Allison Division of General Motors

SUMMARY AND CONCLUSIONS

An annular cascade of six blades was designed and fabricated to exhibit the following aerodynamic characteristics:

- Equivalent weight flow per passage $\dfrac{\dot{m}_p \sqrt{\theta_{cr}}}{\delta_0}$: 1.05 lb/sec

- Equivalent change in tangential velocity:

    Hub : 1247.87 ft/sec
    Mean: 1027.65 ft/sec
    Tip : 873.71 ft/sec

- Blade suction surface diffusion factor, Ds: 0.4

The plain blade was tested and the program base-line level of experimental performance was determined.

PLAIN BLADE

Both flow visualization studies and aerodynamic measurements determined that flow separation occurred on the plain blade suction surface. The region of separated flow on the blade surface exhibited strong radial and circumferential variations. All of the blade configurations of the experimental program were designed for a radially constant suction surface diffusion factor of 0.4; however, plain blade diffusion factors of only 0.330, 0.332 and 0.312 were realized experimentally at the hub, mean, and tip sections, respectively. Also, the hub, mean, and tip sections were 9.0, 8.5, and 11.1% deficient in achieving the required change in tangential velocity across the blade row. Because of the existence of flow separation, the plain blade could not satisfy either the theoretical surface velocity distribution or the radial distribution of downstream gas angle.

VORTEX GENERATOR BLADES

The application of the co-rotating vane vortex generator effected only a very slight reduction in the amount of blade suction surface that experienced flow separation. This boundary layer control device did effect an improvement over the plain blade, however, in achieving the theoretical surface velocity distribution by effecting larger accelerations in the trailing edge region. Also, the radial distribution of downstream gas angle was considerably improved over that of the plain blade. There was, however, no significant increase over the plain blade of the maximum velocity obtained on the suction surface. Because of the reduced differential between the maximum and trailing edge velocity, the co-rotating vane vortex generator actually had less diffusion on the suction surface than did the plain blade. The radial distribution of suction surface diffusion factor was 0.278, 0.303, and 0.208 for the hub, mean, and tip sections, respectively. The hub, mean, and tip sections for this vortex generator configuration were 0.86, 5.48, and 4.77% deficient in achieving the required change in tangential velocity across the blade row. Loss computations demonstrated that the co-rotating vane vortex generator had a lower loss level at the trailing edge but a higher loss level downstream of the trailing edge than did the plain blade.

Application of the triangular plow vortex generators did not, in general, contribute to improved blade performance. A level of velocity, larger than both the plain and co-rotating vane vortex generator blades, was observed on the blade surfaces. This surface velocity distribution resulted in a radial distribution of diffusion factor of 0.238, 0.265, and 0.288 for the hub, mean, and tip sections, respectively. The level of loss was larger for the plow vortex generator than it was for the plain blade in planes located both at and downstream of the blade trailing edge. Also, measurements of the downstream gas angle showed that this blade configuration was quite ineffective in achieving the required amount of gas turning. The combined effect of the large loss level at the blade trailing edge and the reduced amount of gas turning resulted in the plow vortex generator blade design being unable to accomplish the design change in tangential velocity across the blade row. The triangular plow vortex generator was 16.6, 7.8, and 10.7% low at the hub, mean, and tip sections in achieving the design change in tangential velocity across the blade row.

INTRODUCTION

Increasing interest in developing lightweight, highly loaded gas turbine engines confronts the designer with the problem of maintaining a high level of engine performance. A major cause of performance loss in present engines is the condition of the gas flow separating from the blading surfaces. When flow separation is experienced in a blade passage, there is a loss in available kinetic energy, mixing losses are increased, and the desired change in tangential momentum of the gas is not attained. The use of boundary layer control devices offers a possible means of preventing flow separation in maintaining performance in turbomachinery. The NASA Lewis Research Laboratory contracted the Allison Division, GMC, to evaluate the aerodynamic performance of highly loaded turbine stator blades incorporating several kinds of boundary layer control devices. The concepts are:

Vortex generators
Tandem airfoils
Jet-flapped blowing
Tangential jet blowing

This report covers the establishment of the program base-line level of aerodynamic performance generated by the plain blade and subsequent evaluation of the co-rotating vane and the triangular plow type vortex generators with respect to that plain blade performance. Presented are the blade surface static pressure and velocity distributions along with flow visualization results, aerodynamic loss, and boundary layer data. The aerodynamic performance of the tandem, jet-flapped, and tangential jet blades is reported in Volumes III, IV, and V, respectively.

SYMBOLS

A	Area, in.^{2}
D	Vortex generator spacing, in.
$\bar{e}$	Kinetic energy loss coefficient
F_y	Tangential force, lb_f
H	Boundary layer shape factor
h	Vortex generator height, in.
L	Pressure probe foot length, in.
ℓ	blade height, in.
$\dot{m}$	Mass flow rate, lb_m/sec
no	Potential line length, in.
n	Number of data readings in a circumferential sweep
P	Pressure, psia
R	Radial position, in.
Rc	Radius of curvature, in.
s	Blade spacing, in.
T	Temperature, °R
u	Integration variable in tangential direction, in.
W	Velocity, ft/sec
α	Angle of incidence on vortex generator, degrees
β	Gas angle measured from tangential, degrees
γ	Ratio of specific heats
Δ	Incremental change of a variable

δ	Boundary layer displacement thickness, in.
δ_0	Ratio of inlet air total pressure to standard sea level conditions
δ^*	Dimensionless boundary layer displacement thickness
θ	Boundary layer momentum thickness, in.
θ^*	Dimensionless boundary layer momentum thickness
Θ_{cr}	Squared ratio of critical velocity at blade row inlet to critical velocity at standard sea level conditions
ψ	Gas angle measured from axial, degrees
$\bar{\omega}$	Total pressure loss coefficient

Subscripts

0	Station at stator inlet
3	Station immediately downstream of blade trailing edge
4	Station two inches, measured in the axial direction, downstream of the blade trailing edge
amb	Ambient
cr	Conditions at Mach number of unity
f	Force
h	Hub radius
i	Incompressible
ℓ	Local
m	Mass
ma	Mass averaged
min	Minimum
p	Primary

6

st	Static
T	Total
t	Tip
w	Wake
w/o	Without
x	Axial component
y	Tangential component

Superscripts

'	Ideal or isentropic conditions

TEST PROCEDURES AND TYPES OF MEASURED DATA

The test instrumentation, kind of experimental data, and test operational procedures are detailed in reference 1. In addition to obtaining the blade surface static pressure distribution, total pressure information was obtained at three axial locations. A radial survey of total pressure and gas angle was performed approximately 0.75 in. upstream of the cascade on the center passage extended midchannel line with a yawing prism probe. Also, the total pressure immediately behind the two center blades of the cascade was surveyed both radially and circumferentially. Lastly, total pressure, total temperature, and gas angle were surveyed radially and circumferentially in a plane normal to the psuedo-axis of rotation 2 in. downstream of the blade trailing edge. Static pressure was measured by pressure taps located on the extended midchannel lines of the five blade passages at the hub and tip casing walls in planes normal to the psuedo-axis of rotation 0.125 in. upstream of the blade leading edge, 0.125 in. and 2 in. downstream of the trailing edge.

INLET TOTAL PRESSURE AND GAS ANGLE SURVEY

The results of the inlet total pressure survey are shown in Figure 1. In the radial-circumferential plane where the survey was conducted, a reasonably flat total pressure profile (0.67% radial variation) existed upstream of the cascade blade row.

Figure 2 presents the experimental and design values of the inlet gas angle. The inlet gas conditions were controlled by guide walls contoured to generate free-vortex flow. The experimental data points are quite smooth but they exhibit a slightly larger positive radial gradient than that required for free-vortex flow. The plain blade design of reference 1 resulted in 2 degrees of positive incidence at the mean section and zero incidence at the hub and tip. In addition to the design incidence, in the radial-circumferential plane where the survey was conducted, the contoured guide walls were generating positive incidence on the blade row that varied from nearly 5 degrees at the hub section to about 2 degrees at the tip.

BLADE EXIT TOTAL PRESSURE SURVEY

A total pressure survey was performed approximately 0.03 in. downstream of the blade trailing edge with a 0.008-in. dia opening total pressure probe, fixed at 50° from the axial direction. The purpose of the survey was to establish the wake boundary layer behavior and loss characteristics of the various blade configurations being tested. The survey was conducted with a bifurcated probe which permitted data acquisition very near the hub and tip walls. In the case of the plain blade, the probe moved to within 0.040 and

0.050 in. of the hub and tip casings, respectively. Contact between the probe elements and the casing walls was purposely avoided to prevent damage to the probe. Data were recorded via pressure transducer outputs on the Systems Engineering Laboratory (SEL) data acquisition system.

Starting close to the tip casing wall and using the upper pressure sensing element, the probe was swept circumferentially to define the wakes of at least the two center blades of the cascade. The probe was then inserted radially approximately 0.5 in. into the gas stream and another circumferential sweep performed. It was demonstrated that the circumferential sweep rate was low enough that the probe gave essentially the same response irrespective of the direction of circumferential travel. It was also observed, however, that when the probe remained fixed in the separated flow wake of an airfoil, pressure fluctuation of the order of 6% existed. The upper element of the bifurcated probe was only used to survey from the tip casing down to the mean section. From the mean section down to near the hub casing the lower element was used to complete the survey. When 10 radial depths had been surveyed, the mean section circumferential survey was repeated and the probe response compared with the original mean section survey. This provided a positive check on whether the probe element might have become progressively clogged during the survey test.

An example of a circumferential total pressure survey performed at one radial depth immediately behind the blade trailing edge is shown in Figure 3. All measured values were corrected to standard day inlet conditions. At each radial location, the static pressure was obtained by linearly interpolating between the measured values of static pressure at the hub and tip casing walls. The interpolated value of static pressure was assumed constant along the circumferential path at each respective radius. The hub and tip casing values of static pressure were those values indicated by the center pressure taps of the five taps distributed circumferentially at each respective measuring station.

DOWNSTREAM AERODYNAMIC SURVEY

The total pressure, total temperature, and gas angle survey was performed at 10 radial depths, 2 in. downstream of the blade trailing edge by a conventional right-angle yaw probe. As the radial portion of the probe was swept circumferentially, the probe tip yawed in an oscillating fashion as it sought the correct gas angle. This yawing motion of the probe stem resulted in both a radial and circumferential oscillation of the probe tip and is illustrated in Figure 4. Thus, the spatial location of the probe tip had to be calculated at each instant data were recorded. For a given probe foot length, L, and the radial position, R, of the intersection of the centerlines of the probe foot and the probe stem, as the probe hunted for the gas angle, ψ, (measured

from the axial direction) the probe tip oscillated through the circumferential angle of

$$\Delta\theta = \tan^{-1}\left(\frac{L \sin\psi}{R}\right) \tag{1}$$

with a radial oscillation of

$$\Delta R = R\left(\frac{1}{\cos\Delta\theta} - 1\right) \tag{2}$$

The position of the probe tip then was given to be

$$\theta_{\substack{probe \\ tip}} = \theta_{stem} + \Delta\theta \tag{3}$$

and

$$R_{\substack{probe \\ tip}} = R_{\substack{probe \\ elbow}} + \sum_{i=1}^{n} \frac{\Delta R_i}{n} \tag{4}$$

where n is the number of points along the circumferential sweep at which data were taken (usually of the order of 600). Examples of downstream total pressure and gas angle circumferential surveys are shown in Figures 5 and 6, respectively. A relatively large variation in gas angle can be observed as the sensing probe moved from the pressure surface, across the blade trailing edge to the suction surface. A smooth curve has been drawn through the downstream gas angle circumferential survey data; thus, Figure 6 does not show the effects of the hunting characteristics of the prism probe.

FLOW VISUALIZATION STUDY

In addition to the aforementioned aerodynamic measurements, a flow visualization study was performed to locate regions of separated flow on the blade suction surfaces. In a separated flow regime, the free stream flow is detached from and does not necessarily flow tangent to the nearby solid boundary. Also, downstream of the point of separation, very near the wall there is a velocity component which is in a direction opposite the free stream. A flow indicator (a fluid mixture of lampblack and mineral oil) was placed in line from the hub to the tip section very near the suction surface trailing edge and this reverse flow velocity component carried the indicator upstream to define the regions on the blade surfaces that were experiencing flow separation.

DATA REDUCTION

LOSS PARAMETERS

The philosophy for reduction and presentation of the experimental data for the present investigation followed very closely that of Reference 2. In that work, equations were presented and derived for the calculation of local circumferentially mass averaged loss and boundary layer parameters. The local kinetic energy loss coefficient was defined as

$$\bar{e}_\ell = 1 - \frac{W^2}{W'^2} \tag{5}$$

and represents loss in kinetic energy. The velocity W is the actual velocity existing in the blade wake and is calculated from measured total pressure and interpolated static pressure data. The velocity W' is the theoretical value that exists in the blade wake and is likewise calculated from the interpolated static pressure in the wake and the plenum total pressure. Figures 7 and 8 are examples of $\bar{e}_\ell$ calculated at one radial depth from data obtained immediately behind and two in. downstream of the blade trailing edge, respectively.

The circumferential positions of minimum total pressure of the two center blades of the cascade are shown in Figure 3. These circumferential positions determine the upper and lower integration limits for mass averaging quantities over a blade passage. The expression for the mass averaged kinetic energy loss at one radial depth is

$$\bar{e}_{ma} = \frac{\int_0^1 \left[1 - \left(\frac{W^2}{W'}\right)\right]\left(\frac{\rho_{st} \, W}{\rho'_{st} \, W'}\right) d\left(\frac{u}{s}\right)}{\int_0^1 \left(\frac{\rho_{st}}{\rho'_{st}} \frac{W}{W'}\right) d\left(\frac{u}{s}\right)} \tag{6}$$

This mass averaging process was performed, using the trapezoidal integration technique, at each of the 10 radial depths both at and 2 in. downstream of the blade trailing edge. Finally, an integration was performed from the blade hub-to-tip to obtain one value of $\bar{e}$ that was representative of the kinetic energy loss for each blade configuration. The expression for the overall mass averaged $\bar{e}$ was

13

$$\bar{e}_{\substack{\text{over all} \\ \text{ma}}} = \frac{\int_{r_h}^{r_t}\left\{\int_0^1\left[1 - \left(\frac{W^2}{W'}\right)\right]\left(\frac{\rho_{st}}{\rho_{st}'}\frac{W}{W'}\right)\ d\left(\frac{u}{s}\right)\right\}\ dr}{\int_{r_h}^{r_t}\left\{\int_0^1\left(\frac{\rho_{st}}{\rho_{st}'}\frac{W}{W'}\right)\ d\left(\frac{u}{s}\right)\right\}\ dr} \tag{7}$$

Similarly, a local total pressure loss coefficient, $\bar{\omega}$, was defined as

$$\bar{\omega}_\ell = \frac{1 - \dfrac{P_{T_w}}{P_{T_0}}}{1 - \dfrac{P_{st_w}}{P_{T_0}}} \tag{8}$$

and represents a loss in total pressure. It can be shown that for incompressible flow $\bar{e}$ and $\bar{\omega}$ are identical. However, for compressible flow, $\bar{\omega}$ values of loss are consistently larger than $\bar{e}$, the deviation between the two definitions of loss getting larger as compressibility effects become more pronounced. The local values of $\bar{\omega}$ were also integrated circumferentially from the minimum total pressure points of the two center blade wakes to obtain one value of mass averaged $\bar{\omega}$ at each of 10 radial depths. The expression used was

$$\bar{\omega}_{\text{ma}} = \frac{\int_0^1\left[1 - \dfrac{P_{T_w}}{P_{T_0}}\right]\left(\dfrac{\rho_{st}}{\rho_{st}'}\dfrac{W}{W'}\right)\ d\left(\dfrac{u}{s}\right)}{\left[1 - \dfrac{P_{st_w}}{P_{T_0}}\right]\int_0^1\left(\dfrac{\rho_{st}}{\rho_{st}'}\dfrac{W}{W'}\right)\ d\left(\dfrac{u}{s}\right)} \tag{9}$$

Again, a hub-to-tip radial integration using the trapezoidal technique was performed to establish one value of the total pressure loss coefficient that was representative of each blade configuration. The computed expression was

$$\bar{\omega}_{\substack{\text{over all} \\ \text{ma}}} = \frac{\int_{r_h}^{r_t} \left\{ \int_0^1 \left[1 - \frac{P_{T_W}}{P_{T_0}} \right] \left(\frac{\rho_{st} W}{\rho'_{st} W} \right) d \left(\frac{u}{s} \right) \right\} dr}{\int_{r_h}^{r_t} \left\{ \left[1 - \frac{P_{st_W}}{P_{T_0}} \right] \int_0^1 \left(\frac{\rho_{st} W}{\rho'_{st} W'} \right) d \left(\frac{u}{s} \right) \right\} dr} \tag{10}$$

BOUNDARY LAYER PARAMETERS

Basic nondimensional boundary layer parameters of displacement thickness, momentum thickness, and shape factor were defined and calculated over one blade spacing at each radial depth. The equations used were:

Equation (1)   Boundary layer displacement thickness, $\delta*$:

$$\delta* = \frac{\delta}{s \cos \beta_3} = 1 - \int_0^1 \left(\frac{\rho_{st} W}{\rho'_{st} W'} \right) d \left(\frac{u}{s} \right) \tag{11}$$

Equation (2)   Boundary layer momentum thickness:

$$\theta* = \frac{\theta}{s \cos \beta_3} = \int_0^1 \left[1 - \frac{W}{W'} \right] \left(\frac{\rho_{st} W}{\rho'_{st} W'} \right) d \left(\frac{u}{s} \right) \tag{12}$$

Equation (3)   Boundary layer shape factor H:

$$H = \delta*/\theta* \tag{13}$$

In addition to the boundary layer parameters and local circumferentially mass-averaged and overall values of loss above mentioned, several types of data were presented as contour plots. The local values of $\bar{e}$ and $\bar{\omega}$ were presented in contour form at the trailing edge of the blade row. Also, $\bar{e}$ and the downstream gas angle, ψ, were presented as contours in the plane 2 in. downstream of the trailing edge.

All of the data were corrected to NASA standard atmospheric conditions of:

$$W_{cr} = 1019.5 \text{ ft/sec}$$

$$T_{T_0} = 518.7°R$$

$$P_{T_0} = 14.696 \text{ psia}$$

$$\gamma = 1.4$$

PLAIN BLADE PERFORMANCE

The plain blade was designed to establish a base line of performance against which all subsequent blades, incorporating boundary layer control devices, would be compared. The plain blade cascade assembly is shown in Figure 9. A total of 50 static pressure taps were distributed on the two center blades to define the surface static pressure distribution. This assembly is shown installed in the test rig in Figure 10. The vortex generator blades were obtained by merely attaching the vortex generators to the plain blade suction surface. Therefore, the plain and vortex generator blades are identical with respect to solidity, aspect ratio, etc. Pertinent design data for the plain and vortex generator blades are listed in Table I.

EFFECT OF DOWNSTREAM GUIDE WALLS ON PLAIN BLADE PERFORMANCE

It was desired to determine what influence guiding the gas out of the blade row would have on the plain blade performance. A pair of mahogany downstream guide walls contoured to give free-vortex flow conditions was installed in the rig as shown in Figures 63 and 64 of reference 1.

The effects of the downstream guide walls on the plain blade performance can best be illustrated by examining the resulting blade surface velocity distribution and radial variation of the downstream gas angle, ψ. Figures 11, 12, and 13 show that the presence of the guide walls effected a reasonably good agreement of blade surface velocity distribution with the theoretical prediction. The critical velocity ratio data points were calculated using isentropic flow relations and the measured local static to plenum total pressure ratio on the blade surface, and therefore do not reflect an axial gradient in total pressure through the cascade. Similarly, the theoretical velocity distributions shown on Figures 11, 12, and 13 were based on a constant total pressure through the cascade. The agreement of measured and predicted surface velocity was least satisfactory at the blade hub section, being most apparent in the area of high suction surface velocity. Regions of large surface velocity in blade passages are usually synonymous with large surface curvature. A basic assumption of the stream filament blade-to-blade velocity calculations procedure (used in the present blade designs and described in Appendix C of reference 1) is that, on a potential line, the velocity is a function of streamline curvature and the curvature varies linearly over the potential line across the blade passage. As the blade suction surface curvature increases in magnitude, the passage geometry begins to deviate from that required by channel flow theory and begins to approach, at least locally on the suction surface, an isolated airfoil. A useful rule-of-thumb is that when the ratio of the local potential line to the local radius of curvature, $no/Rc \geq 1$, channel flow theory assumptions become questionable.

The plain blade minimum radius of curvature (i. e., maximum curvature) occurred on the hub section suction surface and was of the order of 0.3 in. and $(no/Rc_{min})_{plain\ blade\ hub} \approx 1$. It is suspected the locally large values of hub suction surface curvature placed that portion of the blade in the region where the stream filament calculation technique gave unreliable results. This suspicion is further emphasized when noting the relatively good agreement between measured and predicted surface velocities on the pressure surface. The pressure surface curvature is generally of small value and it satisfies the geometrical constraints required for channel flow theory.

The flow experienced a fairly large acceleration around the leading edge of the blade reaching sonic velocity at the hub and mean sections. This may have been due in part to the incidence generated on the blades by the inlet guide walls.

Figure 6 depicted a typical circumferential variation of the gas angle measured from the axial direction 2 in. downstream of the blade trailing edge. At each radial depth, these data were graphically integrated with a polar planimeter to obtain an average and representative downstream gas angle. A radial variation of this gas angle is shown in Figure 14. Examination of Figure 14 indicates that the presence of the downstream guide walls consistently overturned the gas stream. This comparison is made with respect to the theoretical free-vortex flow radial distribution of gas angle that would exist if the total pressure downstream of the blade row was 96% of the inlet total pressure as designed.

The presence of the downstream guide walls precipitated two undesirable consequences. First, the flow was essentially being turned through a bend by the system of inlet and downstream guide walls resulting in a fairly strong positive static pressure gradient in the circumferential direction, particularly at the hub section. This condition is illustrated in Figure 15. The existence of a strong circumferential variation in static pressure makes assessment of blade performance quite difficult since the mass flow into the blade passages of the cascade will also exhibit circumferential variations. Secondly, a fairly thick boundary layer built up on the exit guide walls which resulted in a contraction of flow area and an acceleration of the mainstream. This condition is depicted in Figure 16. Without the guide walls the free-stream velocity at the hub and tip surfaces approached a constant value downstream of the blade row. With the guide walls installed, the design inlet and exit velocity level requirements were satisfied, but the flow continued to accelerate to the exit of the test rig. The flow was sonic, at least in the hub region of the passage, at the exit plane of the rig.

18

This restriction to the flow caused by the boundary layer buildup resulted in a large value of plenum pressure required to establish the design inlet Mach number level. A direct result of these flow conditions was large tangential loads being developed on the blades. These loads were computed by graphically integrating the static pressure distribution data corresponding to the critical velocity information with the guide walls in place of Figures 11, 12, and 13. These results showed that when the guide walls were installed the tangential blade load was 71.50 lb$_f$ whereas the design value was only 31.33 lb$_f$.

It was decided that, since

● The downstream walls were generating large circumferential gradients in the flow conditions across the cascade, and
● Excessively large loads were imposed on the blades

all subsequent testing of the plain blade and blades incorporating the boundary layer control devices would be tested without the downstream guide walls installed in the rig. Experimental results for the plain blade tests with the exit guide walls installed are listed in Table II.

EXPERIMENTAL PERFORMANCE OF THE PLAIN BLADE WITHOUT THE DOWNSTREAM GUIDE WALLS

Surface Velocity Distributions

Removal of the downstream guide walls had several pronounced effects on the performance of the plain blade. The effects can best be demonstrated by comparing the surface velocity distributions obtained both with and without the downstream guide walls installed in the rig as shown in Figures 11, 12, and 13.

The plain blade was designed to give a radially constant suction surface diffusion factor of 0.4. The measured surface velocities produced experimental hub, mean, and tip diffusion factors of 0.243, 0.362, 0.354 with the guide walls in place and 0.330, 0.332, 0.312 without the guide walls. Since loss data were not obtained at the trailing edge of the plain blade when the exit guide walls were in place, the diffusion factor data are presented on an isentropic velocity distribution basis. The data are shown in Table III.

Figure 98 of reference 3 is a schematic representation of the surface velocity distribution on a cascaded airfoil that is experiencing flow separation. In that figure the velocity is shown to increase to its maximum value on the suction surface and then decrease monotonically until the point of flow separation is reached. From that point on to the trailing edge, the suction surface velocity is essentially constant. It was expected that a similar type of suction surface velocity distribution would be observed in the present

investigation. However, the experimental results of Figures 11, 12, and 13 do not provide any real definition of the location of flow separation from the suction surface. Flow visualization results, which are discussed later, demonstrate that, when the downstream guide walls were omitted, flow separation occurred on the suction surface of the blades. In the case where the guide walls were in place, it is felt that they were guiding the gas through the cascade and keeping it attached to the plain blade suction surface. Flow separation was present where the guide walls were omitted, but, apparently, the difference between the surface static pressure both upstream and downstream of the separation point was so slight that no discontinuity in the suction surface static pressure was discernible and a smooth axial distribution of static pressure was measured.

The experimental surface static pressure distributions corresponding to Figures 11, 12, and 13 are given in Figures 17, 18, and 19. With the guide walls in place, the flow was turned toward the tangential direction and remained attached to the suction surface downstream of the throat. When the walls were removed, the flow could not negotiate the required turning; flow separation from the suction surface was experienced, and the velocity (and, therefore, pressure) distributions on the blade surfaces were altered to indicate a reduction in lift on the airfoil.

Tangential blade loads were computed by graphically integrating the area under the hub, mean, and tip surface static pressure distributions of Figures 17, 18, and 19 with consideration of test plenum conditions. This was accomplished by performing the integration under a smooth curve drawn through the static pressure data points to obtain a force per unit length of blade height at the hub, mean, and tip sections. This force per unit length was then integrated radially to obtain the total tangential blade force. The results presented here include the mean section value of the blade force per unit length.

	Mean section tangential force, $\dfrac{F_{y_m}}{L} - \dfrac{lb_f}{in.}$	Total blade force, F_y-lbf	Flow rate per passage, $\dot{m}_p$-lb$_m$/sec	Mean section tan force/lb primary flow, $\dfrac{F_{y_m}/L}{\dot{m}_p}$	Total blade force/lb primary flow, $F_y/\dot{m}_p$
Plain blade with guide walls	15.89	71.5	2.33	6.819	30.70
Plain blade w/o guide walls	6.98	31.86	1.24	5.629	25.69
Design value (based on area under hub, mean, and tip theoretical static pressure distribution curves)	7.04	31.33	1.05	6.705	29.80

20

On a per pound of primary flow basis, the experimental tangential blade load with the guide walls present was nearly the design value, while without them the load was about 14% less than the design value.

Flow Visualization Results

Regions of strongly separated flow were made evident by using the lamp-black-mineral oil flow visualization technique. Standing aft of the rig and looking forward, the lampblack solution was placed in a thin line along the suction surface side of the trailing edge of the right-most blade. The resulting pattern of separated flow formed immediately and a photograph was taken. This process was repeated sequentially on each blade in a counterclockwise fashion. The entire process was performed at three values of inlet hub static-to-plenum total pressure of 0.82, 0.74, and 0.65 which correspond to approximately 110%, 100%, and 90% of design flow rate in the blade passage, respectively. The results are shown in Figures 20, 21, and 22. Examination of the figures indicates that the amount of blade surface covered by a separated flow region was larger (by a very small amount) at the design flow rate than at flow rates both less than and greater than the design value. The most interesting characteristic of the flow visualization studies is that there was a very strong circumferential variation in the separated flow patterns on adjacent blades. Also, the patterns of separated flow had a definite radial character with the lower portion (from the hub to approximately the mean section) having the flow remaining attached all the way to the trailing edge. From the mean section to the blade tip; however, the blade was covered with regions of separated flow.

The circumferential nature of the separated flow can be attributed wholly to the fact that the flow passages of the cascade form only a segment of and not a complete annulus. This is in contrast to assuming that the circumferential nature of the separated flow regions was due to the circumferential variation of fluid properties, e.g., static pressure. Figure 23 illustrates, when compared with Figure 15, that the circumferential variation of static pressure was greatly reduced when the downstream guide walls were removed.

Consider the flow in the passage between blades 5 and 6 in Figure 24. As the fluid moves off of blade 6 (which is really only a pressure surface) at some angle from the axial direction that is less than the design value, it expands to atmospheric conditions. It may form a streamline depicted by line (a) on Figure 24. Since line (a) does not have the correct downstream angle, it does not form a strong interface for assisting blade 5 in satisfying its (blade 5) turning requirements and gross separation is noted on the suction surface of blade 5. Streamlines (b) and (c) define the large wake of blade 5. Now streamline (c) is turned slightly more from the axial direction than was streamline (a). Therefore, as far as providing assistance to adjacent blades

in meeting their turning requirements, streamline (c) provided more assistance to blade 4 than streamline (a) provided to blade 5. The same logic can be applied all the way across the cascade resulting in a continuously decreasing wake size from blade 6 to blade 1. It was experimentally observed that the wake of blade 3 was generally of smaller size than the wake of blade 4.

Downstream Gas Angle and Tangential Velocity

Average Downstream Gas Angle Radial Distribution

Heavily loaded turbine blades, such as the ones concerned in the present investigation, rely on a portion of the gas turning (13° for the plain blade) to be accomplished on the blade suction surface between the throat and the blade trailing edge. This may be contrasted to a straight back blade where all of the turning has been accomplished by the time the gas travels to the blade throat. If, on a blade designed with gas turning downstream of the throat, the flow separates from the blade suction surface anywhere upstream of the blade trailing edge, then the downstream velocity triangle requirements will not be satisfied.

This appears to be the case for the plain blade as illustrated by the radial variation in downstream gas angle in Figure 14. The plain blade, without the presence of the downstream guide walls, appears to be consistently underturning the gas except perhaps near the hub section. At a given radial depth there is a 4 to 5 degree variation in gas angle, depending on whether or not the downstream guide walls were present.

Change in Tangential Velocity Across Blade Row

The change in equivalent tangential velocity across the blade row was computed by assuming (1) the flow entered and left the cascade at the design inlet angles of Table I and the measured exit average gas angles of Figure 14, respectively, and (2) the hub, mean, and tip velocity levels were those at the leading and trailing edges of Figures 11, 12, and 13, respectively, modified only to include loss effects at the blade trailing edge. The loss computations are discussed later and presented in Table II. The tangential velocity calculation results are:

	Plain blade	Design value
Hub	1136.01	1247.87
Mean	940.59	1027.65
Tip	776.91	873.71

These results show that the plain blade was 9.0, 8.5, and 11.1% deficient at the hub, mean, and tip sections, respectively, in achieving the required change in tangential velocity across the blade row.

Contour Plots

Results at Blade Trailing Edge (Station 3)

The purpose of the total pressure survey, performed at 10 radial stations immediately downstream of the trailing edge (station 3), was to establish the boundary layer and loss characteristics of the blade. The local kinetic energy loss coefficient data at station 3 (e.g., Figure 6) for all 10 radial depths were assembled in contour fashion to delineate a complete graphical representation of the distribution of $\bar{e}_\ell$ as the fluid left the trailing edge of the airfoil. Contours of $\bar{e}_\ell$ at station 3 for the plain blade are shown in Figure 25. Similarly, contours of $\bar{\omega}_\ell$ are shown in Figure 26. In those figures the loss patterns are viewed aft of the blade row looking forward. That is, the rightmost loss coefficient pattern represents the loss distribution in the wake of blade 4 of the cascade. The adjacent loss pattern to the left of blade 4 represents the loss distribution in the wake of blade 3.

Two interesting observations can be made concerning the contours of loss distributions when viewed in light of the total pressure surveys and the flow visualization results. Repeating those results, the total pressure survey showed that, in general, the wake of blade 4 was larger than that of blade 3. This observation was also substantiated by the flow visualization studies which further showed a pronounced radial variation in the size of the separated flow regions on the blade surfaces. Finally, the lampblack patterns indicated that at least on blades 4 and 5 there were two large counter-rotating vortices formed on the suction surfaces.

The contour plots also illustrate the experimentally observed conditions. First, the loss contour patterns of blade 4 are of greater extent than blade 3. Not only do the low loss regions (e.g., $\bar{e}_\ell$ = 0.10) of blade 4 extend over a larger circumferential area than blade 3, but also there are local islands of higher loss ($\bar{e}_\ell$ = 0.980 for blade 4 as compared to $\bar{e}_\ell$ = 0.850 for blade 3). Also, a region of low loss was concentrated near the blade hub section. Second, two high loss cores are clearly discernible on Figures 25 and 26. These cores may be a result of the two counter-rotating vortices on the suction surface which were made evident in the flow visualization study.

Results Downstream of Blade Trailing Edge (Station 4)

Kinetic Energy Loss Coefficient

The local values of $\bar{e}$ for 10 radial depths were computed in a plane 2 in. downstream of the trailing edge and are presented in the contour plot of

Figure 27. The locus of points of minimum total pressure in the wakes of blades 3 and 4 is indicated. The wake characteristics 2 in. downstream of the trailing edge are similar to those at the trailing edge in that the fairly strong circumferential variation of loss coefficient is still evident. Significant mixing of the wake and free stream have occurred to diffuse the wake over more of the blade passage, however. The interesting fact about Figure 27 is the amount of obliquity of the wake in this downstream plane with respect to the wake at the blade trailing edge. The skewed characteristic is a result of the relatively large radial variation in downstream gas angle which was depicted in Figure 14. In that figure, the gas was turned only about 40° from axial at the tip section whereas approximately 57° turning was noted at the hub.

It was nearly impossible to define the wakes of the individual blades from the total pressure survey performed near the hub section at station 4. The level of corrected total pressure was markedly less than 14.696 psia and it was essentially constant in the circumferential direction. This condition was attributed to the gas separating from the rig hub casing wall somewhere between the blade trailing edge and station 4. The result of this is manifested in the high losses shown in the hub region in Figure 27.

Downstream Gas Angle

An example of the circumferential variation in downstream gas angle at the radial position of 13.00 in. is shown in Figure 6. The magnitude of the gas angle varied markedly across the blade trailing edge. Figure 28 shows the complete field of the downstream gas angle distribution for the plain blade. In that figure, lines of constant gas angle from 44 to 56° in 2-degree increments were traced through the flow field. The radial positions at which the experimental surveys were performed are shown as the left hand ordinate of Figure 28. The right hand ordinate is the theoretical value of downstream gas angle (based on a 4% drop in total pressure across the cascade) that corresponds to those experimental radial positions. Because of the large amount of gas turning downstream of the throat on the suction surface of these highly loaded blades, the suction and pressure surfaces in the neighborhood of the trailing edge are not parallel. A gas particle leaves the trailing edge suction surface at a larger angle measured from the axial direction than it would have if it left the trailing edge pressure surface. The effects of this fact on the gas angle distribution are shown in Figure 6, where the gas angle showed a fluctuation of about 4 degrees in the circumferential direction across the wakes of blades 3 and 4. Examination of the measured and theoretical values of gas angle again show that, in general, the gas is under turned except in the passage region very close to the hub section.

Mass Averaged Loss and Boundary Layer Parameters

Results at Blade Trailing Edge (Station 3)

Radial variations of circumferentially mass averaged values of kinetic energy and total pressure loss coefficients are shown in Figures 29 and 30. Similarly δ^*, θ^*, and H values were computed at each radial depth surveyed and are shown in Figures 31, 32, and 33. The total pressure surveys performed immediately behind the two center blades of the cascade, their resulting loss contour plots, and the flow visualization studies have each shown that the flow separated from the blade surface radially outward from about the blade mean sections to the tip sections but remained attached from about the mean section to the blade hub. The mass averaged results of Figures 29 and 30 further substantiate these findings by demonstrating that the loss coefficients, in general, decrease in magnitude as the hub region is approached.

When fluid separates from blading surfaces there results a reduction of the available flow area for the free-stream flow to pass through. The amount of area reduction or blockage is described in the relative sense by the displacement thickness. That is, regions of large blockage are described by large displacement thicknesses. Also, the blocked areas are filled with low energy boundary layer flow. Since the boundary layer momentum thickness is a measure of energy dissipated due to viscous and mixing actions, separated flow regions are characterized by large momentum thickness.

The radial variation of the boundary layer displacement and momentum thicknesses, shown in Figures 31 and 32, exhibit the aforementioned characteristics. Known regions of separated flow are identified with relatively larger values of δ^* and θ^*. Likewise, when flow remains attached both δ^* and θ^* have small values.

In most analytical boundary layer studies reported in the literature, the location of incipient flow separation is identified by the magnitude of the incompressible boundary layer shape factor, $H_i = \delta_i^* / \theta_i^*$. Sufficient experimental incompressible boundary layer data exist in the literature to correlate the behavior of H_i with the location of flow separation. A range of $H_i = 1.8$ to 2.2 has been experimentally shown to correspond to a separating boundary layer. Turbulent, compressible boundary layer calculations are usually performed by transforming the compressible equations of motion into an equivalent incompressible form and then using the incompressible shape factor criteria, $H_i = 1.8$ to 2.2, as an indication of flow separation.

The compressible boundary layer shape factor, $H = \delta^* / \theta^*$, has been computed, and is shown in Figure 33. The Culick-Hill transformation, described in reference 4, introduces the effects of compressibility on the boundary layer shape factor by the expression

$$H + 1 = (H_i + 1) \frac{T_{T_\infty}}{T_{st_3}} \tag{14}$$

where:

H is the compressible shape factor

H_i is the incompressible shape factor

T_{T_∞} is the gas stagnation temperature in the freestream

T_{st_3} is the gas static temperature at the edge of the boundary layer at station 3

It was of interest to estimate the value of H that would exist if the turbulent, compressible boundary layer experienced separation in the trailing edge region of the plain blade.

$$\left.\frac{W}{W_{cr}}\right)_3 \approx 0.65 \text{ (See Figures 11, 12, and 13)}$$

$$\frac{T_{T_\infty}}{T_{st_3}} \approx 1.075$$

H_i = 1.8 for separation in the incompressible flow field

H = (1.8 + 1.0) 1.075 - 1.0 $\approx$ 2.0 for separation in the compressible flow field

The result shows that the shape factor distribution of Figure 33 indicates that the flow in the trailing edge region of the plain blade in most cases is just at the threshold of incipient separation. In several instances the value of H was significantly larger (H $\approx$ 3.0-4.0) than 2.0. The radial distribution of the compressible shape factor augments the other experimental findings of this investigation by showing that the plain blade probably functioned with the flow detached from the blade surfaces at least in the neighborhood of the blade trailing edge.

Results Downstream of Blade Trailing Edge (Station 4)

When fluid leaves the trailing edge of the blade, nonuniformities in the circumferential direction of the flow field are generated by the formation of the blade wake. In the present investigation, nonuniformity of flow was also observed in the radial direction due to the flow having a preference for separating from only the radially outward half of the suction surface. As the fluid

proceeds downstream, mixing takes place between the free stream and wake flows until at some distance downstream flow conditions again become uniform. At this downstream station, the blade loss is larger than that computed at the blade trailing edge; the difference being attributed to losses generated by the mixing of the free stream and wake flows. The loss at the downstream station represents the true loss of the blade.

Figures 34 and 35 show the radial distribution of the circumferentially mass averaged values of kinetic energy and total pressure loss coefficients evaluated in the radial-circumferential plane of station 4. These results illustrate that the loss was nearly uniform in the region of the mean section of the blade, indicating a smoothing of the nonuniformities in the flow which existed at the blade trailing edge, but increased in magnitude as both the hub and tip walls were approached. The reason the loss appears larger in the hub than in the tip region is that, as explained earlier, the total pressure survey results near the hub section indicated that the flow was separating from the rig hub casing wall.

Overall mass averaged values of $\bar{e}$ and $\bar{\omega}$ were computed from Equations 7 and 10, respectively, at stations 3 and 4, and are presented here and are listed in Table II. Other pertinent experimental data are also shown in Table II.

Overall mass averaged	Station	
	3	4
$\bar{e}$	0.0959	0.1133
$\bar{\omega}$	0.1061	0.1308

These data show 18.14% and 23.28% increase in $\bar{e}$ and $\bar{\omega}$, respectively, as the gas proceeded from station 3 to station 4.

The expressions for δ^*, θ^*, and H were defined earlier and are rewritten here.

$$\delta^* = 1 - \int_0^1 \left(\frac{\rho_{st}\ W}{\rho_{st}'\ W'}\right)\ d\left(\frac{u}{s}\right) \tag{15}$$

$$\theta^* = \int_0^1 \left[1 - \frac{W}{W'}\right] \left(\frac{\rho_{st}\ W}{\rho_{st}'\ W'}\right)\ d\left(\frac{u}{s}\right) \tag{16}$$

$$H = \delta^*/\theta^* \tag{17}$$

As the flow proceeds downstream of the blade trailing edge and uniform conditions are approached, the boundary layer parameters approach constant values. That is:

$$\delta^*)_4 \rightarrow 1 - \frac{\rho_{st}\, W}{\rho_{st'}\, W'} \tag{18}$$

$$\theta^*)_4 \rightarrow \left(1 - \frac{W}{W'}\right) \frac{\rho_{st}\, W}{\rho_{st'}\, W'} \tag{19}$$

$$H)_4 \rightarrow \frac{1 - \dfrac{\rho_{st}\, W}{\rho_{st'}\, W'}}{\left(1 - \dfrac{W}{W'}\right) \dfrac{\rho_{st}\, W}{\rho_{st'}\, W'}} \tag{20}$$

An analogy of the asymptotic behavior of the shape factor in cascade flow may be drawn to the behavior of H downstream of an isolated airfoil. For an isolated airfoil with an approach velocity, W_0, the velocity W_3 at the edge of the trailing edge boundary layer increases with increasing distance downstream of the trailing edge until at some large distance W_3 equals W_0. Simultaneously, H decreases from its value at the trailing edge, H_3, until it reaches a value of unity at the large distance. In cascade flow, H will decrease from its value at the trailing edge H_3 to a value at a distance downstream where complete mixing has taken place and conditions are uniform. The value of H existing in this downstream station will be determined primarily by the value of the downstream total pressure. For instance, if it is assumed that, in the present plain blade investigation, the experimental conditions which were observed at station 4 represented conditions after complete mixing had occurred (this was not quite the case since the blade wakes were still discernible), then the following estimates of after mixing boundary layer parameters can be made:

At station 4

$$\overline{\omega}_{\substack{\text{overall} \\ \text{ma}}} = \frac{1 - \dfrac{P_{T_w}}{P_{T_0}}}{1 - \dfrac{P_{st_w}}{P_{T_0}}}$$

For

$$\bar{\omega}_{oa_{ma}} = 0.131 \quad \text{(See Table II)}$$

$$\left.\begin{array}{l} P_{T_0} = 18.42 \text{ psia} \\[2ex] P_{st_w} = 14.3 \text{ psia} \end{array}\right\} \text{measured data}$$

Then

$$P_{T_w} = 17.88 \text{ psia}$$

$$\rho_{st}, \ W = f(P_{T_w}, \ P_{st_w})$$

$$\rho_{st'}, \ W' = g(P_{T_0}, \ P_{st_w})$$

and can be evaluated from isentropic relations. Inserting the values of ρ_{st}, $\rho_{st'}$, W and W' in Equations 18, 19 and 20 yields

$$\left.\delta^*\right)_4 = 0.068$$

$$\left.\theta^*\right)_4 = 0.054$$

and

$$\left.H\right)_4 = 1.258$$

Figures 36, 37 and 38 show the radial distribution of the boundary layer parameters that existed at station 4 for the plain blade. Two things are evident: (1) the radial distributions of δ^*, θ^*, and H are much more uniform at station 4 than they were at station 3, indicating the flow irregularities were smoothed by the mixing process that occurred between stations 3 and 4, (2) the estimated after-mixing values of the boundary layer parameters given correspond quite closely with the measured and nearly radially constant values of δ^*, θ^*, and H given in Figures 36, 37 and 38, respectively. The implication of these results is that perhaps mixing was essentially completed at station 4.

Summary of Plain Blade Performance
_____

In summary, the downstream guide walls had a pronounced effect on the performance of the plain blade and were justifiably removed so that that performance could be properly assessed.

When the guide walls were removed, it was determined from both flow visualization studies and aerodynamic measurements that the flow separated from the blade surface. The region of separated flow on the blade suction surface exhibited strong circumferential variations which were attributed to effects caused by the flow path being only a segment of and not a complete annulus. Radial variations were also observed.

Based on a radial total pressure survey performed at one circumferential position upstream of the two center blades of the cascade, there was evidence that the inlet guide walls may have been generating some incidence on the blade leading edges.

The plain blade was designed for a suction surface diffusion factor of 0.4; however, without the downstream guide walls in place, diffusion factors of only 0.330, 0.332, and 0.312 were realized experimentally at the hub, mean, and tip sections. Also, the hub, mean, and tip sections were 9.0, 8.5, and 11.1% deficient in achieving the required change in tangential velocity across the blade row. Without the assistance of the downstream guide walls the plain blade was not able to satisfy either the theoretical surface velocity distributions or the radial distribution of the downstream gas angle. Even though flow separation was observed by the lampblack-mineral oil flow visualization technique there was no evidence of flow separation from the surface velocity distributions.

Overall mass averaged loss coefficients were computed at the blade trailing edge (station 3) and 2 in. (measured axially) downstream of the trailing edge (station 4). It was observed that the loss increased significantly as the flow proceeded from station 3 to station 4. The performance at station 4 was masked somewhat by the fact that the flow appeared to be separating from the rig casing hub wall at that computing station. The computed values of overall mass averaged loss coefficients at stations 3 and 4 were:

	Station			
	3		4	
	$\bar{e}$	$\bar{\omega}$	$\bar{e}$	$\bar{\omega}$
Plain blade	0.0959	0.1061	0.1133	0.1308

VORTEX GENERATOR BLADES

The aerodynamic analysis of the flow about the plain blade configuration is given in reference 1. This analysis showed that flow separation should be experienced on the suction surface; the experimental results given in the preceding section verified that this is the case. The purpose of the vortex generator configurations selected for the investigation described herein was to promote mixing of the high energy free-stream flow with the low energy boundary layer flow, thereby preventing separation of the flow from the suction surface.

Two types of vortex generators were investigated—a two-dimensional co-rotating vane and a three-dimensional triangular plow. These devices are shown in Figure 39. The dimensions of the vortex generators shown in Figure 39 are:

	D(in.)	h(in.)	α(deg)	Length(in.)	Thickness(in.)
Co-rotating vane	0.100	0.015	20.0	0.060	0.005
Triangular plow	0.200	0.020	0.0	0.060	—

The vortex generators were attached to the suction surface of the plain blade after testing of the plain blade had been completed.

CO-ROTATING VANE VORTEX GENERATOR BLADE PERFORMANCE

The design point flow conditions for the vortex generator blades were established by setting the hub section leading edge critical velocity ratio to be identical with that for the plain blade, 0.704. The same set of inlet guide walls was used for both the plain blade and the vortex generator blades.

Velocity and Pressure Distributions

Circumferential Static Pressure

The variation of static pressure (nondimensionalized on the plenum total pressure) in the circumferential direction at the hub and tip sections immediately upstream and downstream of the cascade is shown in Figure 40. Comparing Figure 40 with Figure 23 for the plain blade shows that the circumferential variation of the flow properties is slightly improved (that is, the static pressure was nearly circumferentially uniform). In Figure 40, the free-vortex nature of the flow at the trailing edge is essentially absent as the hub and tip static pressures are approximately equal.

Blade Surface Velocity and Pressure Distributions

The distribution of the critical velocity ratio over the blade surfaces for the co-rotating vane vortex generator blade hub, mean, and tip sections is shown in Figures 41, 42, and 43, respectively. These velocity distributions are based on a constant total pressure across the cascade. The corresponding static pressure distributions are shown in Figures 44, 45, and 46. Comparison of Figures 44, 45, and 46 with Figures 17, 18, and 19 for the plain blade shows that data from several of the vortex generator static pressure taps are missing. This was the result of the taps becoming inoperative during testing and/or rework and could not be practicably repaired. The velocity plot results still show a relatively large discrepancy between predicted and measured values on the suction surface in the neighborhood of 30 to 40 percent of the axial chord. This condition is attributed to deficiencies in the velocity prediction technique in regions of large surface curvature. Comparison of Figures 41, 42, and 43 with the surface velocity distributions without the downstream guide walls of Figures 11, 12, and 13 for the plain blade indicates that the vortex generator was more effective than the plain blade in achieving the suction and pressure surface theoretical velocity distribution in the trailing edge region. There was no significant increase over the plain blade of the maximum velocity obtained on the suction surface. Because of the reduced differential between the maximum and trailing edge velocities, the co-rotating vane vortex generator actually had less diffusion on the suction surface than the plain blade. The radial distribution of the suction surface diffusion factor was 0.278, 0.303, and 0.208 for the hub, mean, and tip sections, respectively. These data are given in Table III.

Blade loads were computed from the static pressure distribution. However, because of the limited amount of surface static pressure data available, the force was computed on a per unit blade length basis only at the mean section. The result of this calculation for the plain and co-rotating vane vortex generator blades is as follows:

	Mean section tangential blade force per unit blade length, F_y/L (lb$_f$/in.)	Flow rate per passage, $\dot{m}_p$(lb$_m$/sec)	Mean section unit tangential blade force per pound of passage flow, $\dfrac{F_y/L}{\dot{m}_p}$ $\left(\dfrac{\text{lb}_f/\text{in.}}{\text{lb}_m/\text{sec}}\right)$
Plain blade	6.98	1.240	5.629
Co-rotating vane vortex generator	7.62	1.192	6.393
Design	7.036	1.050	6.705

The measured vortex generator velocity more closely approached the theoretical distribution than did that for the plain blade. Also, more lift per pound of primary flow was generated on the vortex generator blade, at least at the blade mean section.

Flow Visualization Results

Application of the lampblack-mineral oil flow visualization technique revealed that the presence of the co-rotating vane vortex generator did not contribute significantly to the elimination of flow separation. Figures 47, 48, and 49 show the results for approximately 90, 100, and 110% design flow rate conditions. Figures 47 and 49 indicate slightly larger regions of separated flow than the corresponding plain blade conditions. It appears, however, that at the design flow conditions, the presence of the vortex generators effected a slight reduction in the amount of blade suction surface covered by separated flow. The strong circumferential variation of the separated flow regions observed on the plain blade is still evident on this vortex generator configuration. The radial location of the separated flow regions, however, is shifted somewhat toward the tip sections. This radial shifting is probably due to the orientation of the vortex generators on the suction surface. Figure 13 of reference 1 shows that near the suction surface, the vortex generator should impart a radial component to the gas in the direction of the tip section.

Downstream Gas Angle and Tangential Velocity

Average Downstream Gas Angle Radial Distribution

The radial variation of the gas angle for the two center blades of the cascade (blade numbers 3 and 4) at station 4 is shown in Figure 50. Comparison of Figure 50 with the corresponding data of Figure 14 for the plain blade (without the downstream guide walls) shows that the co-rotating vane vortex generator effected a considerable improvement over the plain blade in achieving the predicted gas angle radial distribution. The slope of the experimental data points for both the co-rotating vane vortex generator and the plain blade is more negative than the theoretical curve. That is, there was greater turning of the gas near the hub section than at the tip. In the case of the vortex generator blade, the theoretical value was obtained near the blade mean section, with overturning at the hub and underturning at the tip. This observation implies that there is less total pressure loss at the hub than at the tip; this agrees with the flow visualization results which showed the flow to have a strong preference to separate at the tip but not at the hub.

Change in Tangential Velocity Across Blade Row

The change in equivalent tangential velocity across the blade row was computed by assuming (1) the flow entered the cascade at the design inlet angles given in Table I and left at the measured exit average gas angles shown in Figure 50 and (2) the hub, mean, and tip velocity levels were those at the leading and trailing edges of Figures 41, 42, and 43, respectively, modified to include loss effects at the blade trailing edge. The loss computations are presented in Table II.

The results of the co-rotating vane vortex generator blade change in tangential velocity calculations are:

		Design value
●	Hub—1237.08	1247.87
●	Mean—971.37	1027.65
●	Tip—832.09	873.71

These results show that this blade configuration was 0.86, 5.48, and 4.77% deficient at the hub, mean, and tip sections, respectively, in achieving the required change in tangential velocity across the blade row.

Contour Plots

Results at Blade Trailing Edge (Station 3)

Contour plots of the local values of kinetic energy and total pressure loss coefficients just downstream of the trailing edge are shown in Figures 51 and 52, respectively. These plots show radial and circumferential variations similar to those observed for the plain blade in Figures 25 and 26. The wakes of this vortex generator blade appear to be narrowed slightly with many of the irregularities observed on the plain blade smoothed out. However, the core of the wake is filled with a contour of loss level that is considerably larger than that for the plain blade. As will be shown later the overall mass averaged values of kinetic energy and total pressure loss at the trailing edge of the co-rotating vane vortex generator blade were less than those computed for the plain blade. Apparently, the effect of the large region of high loss of the vortex generator blade was overcompensated for by the decreased wake size, resulting in reduced overall loss coefficients.

Results Downstream of Blade Trailing Edge (Station 4)

Kinetic Energy Loss Coefficient

Contours of the local values of the kinetic energy loss coefficient computed at station 4 are shown in Figure 53. Comparison of these data with

34

the plain blade data in Figure 27 shows that the loss increased significantly as the flow proceeded downstream of this blade configuration. Analysis of the wakes at station 4 shows that the co-rotating vane vortex generator blade produced a wake that was not only broader but also had regions of higher loss than the plain blade wake. The hub section of this blade configuration is characterized by a large region of high loss as was the plain blade. Further, it is shown below that the overall mass averaged loss coefficients for the co-rotating vane vortex generator are considerably larger than those for the plain blade.

Downstream Gas Angle

A contour field plot of the gas angle, measured from axial, 2 in. downstream of the co-rotating vane vortex generator blade trailing edge is shown in Figure 54. The data exhibit the same general characteristics as the plain blade data in Figure 28. The magnitude of the gas angle fluctuated about 4 degrees across the wake in the circumferential direction. Figure 50 showed that the flow between blade numbers 3 and 4 of the cascade was overturned near the hub but underturned near the tip section. The details of this observation are shown in Figure 54. The magnitude of the gas angle in the neighborhood of the mean section was approximately the theoretical value (shown as the ordinate on the left hand side of Figure 54). The measured gas angles generally were larger than the theoretical values of the hub and smaller than the theoretical values at the tip section.

Mass Averaged Loss and Boundary Layer Parameters

Results at the Blade Trailing Edge (Station 3)

Circumferential mass averaging of the station 3 loss data was performed at each of the 10 radial depths for this blade configuration and is shown in Figures 55 and 56 for the kinetic energy and total pressure loss coefficients, respectively. The data exhibit trends similar to the plain blade data in that the loss decreased in the direction of the hub section. The level of the loss coefficients, however, is less than that for the plain blade. The magnitude of the overall mass averaged loss coefficients was computed and demonstrated that at the trailing edge of the blade the loss coefficients for the co-rotating vane vortex generator blade were less than those for the plain blade. Those values were:

	Overall mass averaged loss coefficients at station 3	
	$\bar{e}$	$\bar{\omega}$
Plain blade	0.0959	0.1061
Co-rotating vane vortex generator	0.0732	0.0783

These values are also included in Table II and represent a 23.7% reduction in $\bar{e}$ and 26.2% reduction in $\bar{\omega}$ at the blade trailing edge for the vane type vortex generator with respect to the plain blade.

The boundary layer displacement calculations, shown in Figure 57, illustrate clearly how the magnitude of δ^* increases (reflecting blockage) in a separated flow. On the radially outward portion of the blade, where the flow is known to have separated from the blade surface, δ^* has a large value; but as the hub is approached evidence of separation diminished and δ^* progressively decreased in magnitude.

The radial distribution of the compressible boundary layer shape factor was computed from the δ^* and θ^* data of Figures 57 and 58, respectively, and is illustrated in Figure 59. There was much scatter in the data indicating the following 2 conditions:

● There was a high degree of irregularities in the flow as it moved off the trailing edge of the blade
● It was noted in the plain blade discussion in Section VI that a value of $H \approx 2.0$ was a reasonable estimate for a separation criteria under the present aerodynamic conditions

Following that reasoning, it may be concluded that, since nearly the outward 2/3 of the blade had values of $H > 2.0$, Figure 59 substantiates all of the earlier observations made concerning flow separating from the radially outward portion but remaining attached to the radially inward portion of the co-rotating vane vortex generator blade.

Results Downstream of the Blade Trailing Edge (Station 4)

The boundary layer and circumferentially mass averaged loss characteristics were computed for the 10 radial depths at station 4 and are depicted in Figures 60 through 64. Consider Figure 60 for the vortex generator blade and Figure 34 for the plain blade. At the mean section the loss is approximately the same with the plain blade being slightly superior. However, the tip section indicates the vortex generator blade has better loss characteristics. The hub section predominates and determines the overall loss characteristics of these blades at this axial station. The vortex generator blade has considerably larger loss coefficients in the hub region than does the plain blade. This effect is attributed to the flow separating off the hub casing wall at this axial location. Figures 50 and 54 show the vortex generator blade accomplished greater gas turning (from axial) than did the plain blade. The flow was turned more towards the tangential direction and, therefore, was more susceptible to separation from the hub casing wall. Unfortunately, this casing wall separation effect masks the performance of the blades at this

36

axial location. The overall mass averaged loss coefficients were computed for this axial location and are shown here and in Table II.

Overall mass averaged loss coefficient at station 4

	$\bar{e}$	$\bar{\omega}$
Plain blade	0.1133	0.1308
Co-rotating vane vortex generator	0.1329	0.1521

The boundary layer characteristics are illustrated in Figures 62, 63, and 64 and show that the vortex generator configuration exhibited characteristics similar to the plain blade. The flow appeared to be nearly completely smoothed out by the time it reached station 4.

Summary of Co-rotating Vane Vortex Generator Blade Performance

The application of the co-rotating vane vortex generator effected only a very slight reduction in the amount of blade suction surface that experienced flow separation. This boundary layer control device did effect a substantial improvement over the plain blade in achieving the theoretical surface velocity distribution by effecting larger accelerations in the trailing edge region. Also the radial distribution of downstream gas angle was considerably improved over that of the plain blade.

Even though the co-rotating vane vortex generator had an improved velocity distribution in the trailing edge region, it had less suction surface diffusion than the plain blade, and the radial distribution of D_s was 0.278, 0.303, and 0.208 for the hub, mean, and tip sections. The design D_s was a radially constant value of 0.4.

The co-rotating vane vortex generator hub, mean, and tip sections were, respectively, 0.86, 5.48, and 4.77% deficient in achieving the required change in tangential velocity across the blade row.

Loss coefficient computations demonstrated that the loss level at the trailing edge of this vortex generator configuration was somewhat less than that for the plain blade. At the downstream computing station (station 4), the loss level was equal to or greater than that for the plain blade at all radial stations except near the hub region. Here, the flow separated from the hub casing wall. The loss computed at the hub region had a large value which penalized the co-rotating vane vortex generator overall mass averaged loss

coefficient. Even if the radial distribution of loss coefficient near the hub section had been identical for the plain and co-rotating vane vortex generator blade configurations, it is felt that the vortex generator would have demonstrated a larger overall mass averaged loss coefficient at station 4. The computed values of overall mass averaged loss coefficients were:

	Station			
	3		4	
	$\bar{e}$	$\bar{\omega}$	$\bar{e}$	$\bar{\omega}$
Co-rotating vane vortex generator	0.0732	0.0783	0.1329	0.1521
Plain blade	0.0959	0.1061	0.1133	0.1308

TRIANGULAR PLOW VORTEX GENERATOR BLADE PERFORMANCE

Upon completion of testing of the co-rotating vane vortex generator blade configuration those vortex generators were removed from the blade suction surface and the triangular plow type was installed. A photograph of that assembly is shown in Figure 65.

Velocity and Pressure Distributions

Circumferential Static Pressure

The circumferential variation of the hub and tip static pressure, measured immediately upstream and downstream of the blade row (stations 0 and 3) is illustrated in Figure 66. There is very little variation of this property in the circumferential direction indicating a reasonably uniform distribution of flow between the blades of the cascade. Figure 66 shows that the fluid exhibited free vortex flow characteristics at the trailing edge which was essentially absent on the co-rotating vane vortex generator.

Blade Surface Velocity and Pressure Distributions

Hub, mean, and tip section surface velocity distributions were shown on Figures 41, 42, and 43 and compared with those of the co-rotating vane. Except for the inlet radial velocity distribution, which was the same for all blades tested, the magnitude of the surface velocity distributions was consistently larger for the plow vortex generator than it was for either the co-rotating vane or the plain blade. These hub, mean, and tip velocity distributions yielded suction surface diffusion factors for the plow vortex generator of 0.238, 0.265 and 0.288, respectively. These Ds data are shown in Table III where they can be compared with the plain and co-rotating vane vortex generator blades. The plow vortex generator hub, mean, and tip section surface static pressure distributions, which correspond to the

38

surface velocity distributions of Figures 41, 42, and 43 are illustrated in Figures 67, 68, and 69, respectively. The mean section tangential blade force was computed on a per unit blade length basis by graphic integration of the static pressure data of Figure 68. The results are presented here for comparison with similar information for the plain and co-rotating vane vortex generator blades.

	Mean section blade force per unit blade length, F_y/L $(lb_f/in.)$	Flow rate per passage, $\dot{m}_p$ (lb_m/sec)	Mean section unit tangential blade force per pound of passage flow, $\dfrac{F_y/L}{\dot{m}_p}\left(\dfrac{lb_f/in.}{lb_m/sec}\right)$
Plain blade	6.98	1.240	5.629
Co-rotating vane vortex generator	7.62	1.192	6.393
Triangular plow vortex generator	8.34	1.330	6.271
Design	7.036	1.050	6.705

These results show that though the plow vortex generator blade had the largest mean section lift on an absolute basis, when the increased plenum requirements of pressure and flow rate were taken into account, the plow vortex generator's performance was slightly inferior to that of the co-rotating vane vortex generator blade.

Flow Visualization Results

The results of the flow visualization study for approximately 90, 100, and 110% design flow rate for the plow vortex generator are depicted in Figures 70, 71, and 72, respectively. The resulting patterns of separated flow on the blade suction surfaces indicate that the plow vortex generator used in these tests was quite ineffective in re-energizing the boundary layer flow and preventing flow separation. In nearly all cases, the condition of flow separation seems to have been aggravated by the presence of the plow vortex generator. Also, the strong circumferential and radial variation in the separated flow regions observed on the plain and co-rotating vane vortex generator blades is still evident in Figures 70, 71, and 72.

Downstream Gas Angle and Tangential Velocity

Average Downstream Gas Angle Radial Distribution

Figure 73 demonstrates clearly that, at least for blades 3 and 4 of the cascade, the application of the triangular plow vortex generator was not adequate to achieve the correct level and radial distribution of the downstream gas angle. When compared with Figure 14 for the plain blade, in most cases, the plow vortex generator blade effected less turning (particularly in the neighborhood of the mean section) than did the plain blade. The implication here is that the presence of the plow vortex generator did not promote a mixing of the free stream and boundary layer flows but significantly increased the drag of the airfoil. The increased drag resulted in an increase in total pressure loss downstream of the blade which showed up as reduced gas turning. That the loss coefficients for this configuration were significantly larger than the plain blade will be shown later.

Change in Tangential Velocity Across Blade Row

The change in tangential velocity across the blade row was computed by these assumptions:

● The flow entered and left the cascade at the design inlet angles of Table I and the measured exit gas angles of Figure 73, respectively
● The hub, mean, and tip velocity levels were those at the leading and trailing edges of Figures 39, 40, and 41, respectively, modified for loss effects at the blade trailing edge

The loss computations are presented in Table II. The results of the triangular plow vortex generator change in tangential velocity calculations are:

	Triangular plow vortex generator	Design value
Hub	1041.01	1247.87
Mean	947.10	1027.65
Tip	780.19	873.71

These results show that this blade was substantially deficient in achieving the desired change in tangential velocity across the blade row. This is a direct result of the high loss at the blade trailing edge. The hub, mean, and tip sections were, respectively, 16.57, 7.84, and 10.70% low with respect to the design values in effecting the correct ΔW_u across the blade row.

Contour Plots

Results at the Blade Trailing Edge (Station 3)

Figures 74 and 75 show contours of total pressure and kinetic energy loss coefficients obtained from the boundary layer surveys which were performed at 10 radial depths immediately downstream of the blade trailing edge. These data, when compared with Figures 25 and 26 for the plain blade, generally indicate a higher loss level for the plow vortex generator than for the plain blade. This is particularly true near the hub section. Having a region of high loss near the hub section is difficult to explain in light of the flow visualization results of Figures 20 and 70 for the plain and plow vortex generator blades, respectively. These figures demonstrate clearly that the hub sections of blade numbers 3 and 4 for both blade configurations did not experience flow separation. The hub section loss contours of Figures 73 and 74 may have been caused by secondary flow effects that were somehow amplified by the presence of the triangular plow vortex generator.

Results Downstream of Blade Trailing Edge (Station 4)

Kinetic Energy Loss Coefficient

Contours of the kinetic energy loss coefficient, computed 2 in. downstream of the plow vortex generator blade trailing edge, are illustrated in Figure 76. These contours show that the wakes of the plow vortex generator blade were approximately of the same width as those of the plain blade. Further, the high loss wake regions were slightly larger for the plow vortex generator and its hub section was filled with separated flow from the rig casing hub wall.

The reduced amount of gas turning is reflected in the small amount that the wakes of Figure 76 are radially skewed in the circumferential direction.

The wake loss contours seem to oscillate in the circumferential direction. It is suspected that, because the triangular plow vortex generators shed counter-rotating vortices, the wake circumferential oscillations are a manifestation of the presence of this type of vortex generator on the blade surface. No correlation of plow geometry and/or position and wake circumferential oscillation frequency have been found to date.

Downstream Gas Angle

Contours of the triangular plow vortex generator downstream gas angle field are shown in Figure 77. The data do not contribute substantially beyond what has already been presented except to show that the plow vortex generator blade consistently underturned the gas.

41

Mass Averaged Loss and Boundary Layer Parameters

Results at the Blade Trailing Edge (Station 3)

The average level of the kinetic energy and total pressure loss coefficients was, generally, about the same as for the plain blade except near the hub section where the loss level for the vortex generator blade increased very markedly. This increase is demonstrated in Figures 78, 79, and 29, 30 for the plow vortex generator and plain blades, respectively. The computed high loss values near the hub merely substantiate the loss contour plots of Figures 74 and 75.

Overall mass averaged values of the loss coefficients were computed at this axial station and are presented here along with similar data for the plain and co-rotating vane vortex generator blades. These data and additional pertinent experimental information are also included in Table II.

<u>Overall mass averaged loss coefficients at station 3</u>

	$\bar{e}$	$\bar{\omega}$
Plain blade	0.0959	0.1061
Co-rotating vane vortex generator	0.0732	0.0783
Triangular plow vortex generator	0.1034	0.1149

These values represent an increase in loss at the trailing edge of 7.82% for $\bar{e}$ and 8.29% for $\bar{\omega}$ due to the presence of the triangular plow vortex generator on the blade suction surface.

The radial distribution of the boundary layer characteristics, shown in Figures 80, 81, and 82, support all of the previously mentioned findings for this blade configuration by showing the large magnitude and amount of scatter in the boundary layer shape factor data (Figure 82). This condition indicates that this blade is operating poorly with much of the flow in a separated state as it passes off the trailing edge of the blade.

Results Downstream of the Blade Trailing Edge (Station 4)

The boundary layer and circumferentially mass averaged loss characteristics computed at this axial location are demonstrated in Figures 83 through 87. In general, they indicate a very high loss region near the hub section.

The magnitude of the overall mass averaged loss coefficients was computed and they are compared here with the values for the plain and co-rotating vane vortex generator blades.

Overall mass averaged loss coefficients at station 4

	$\bar{e}$	$\bar{\omega}$
Plain blade	0.1133	0.1308
Co-rotating vane vortex generator	0.1329	0.1521
Triangular plow vortex generator	0.1346	0.1504

As mentioned earlier, the value of the overall mass averaged data at station 4 is questionable since the true performance was masked by the fact that the flow was separating from the rig hub casing. These data can also be found in Table II.

The boundary layer data of Figures 85, 86, and 87 show that, with the exception of flow near the hub region, the flow had nearly smoothed out by the time it reached station 4.

Summary of Triangular Plow Vortex Generator Blade

Application of the triangular plow vortex generators did not, in general, contribute to improved blade performance. A level of velocity larger than either the plain or co-rotating vane vortex generator blades was observed on the blade surfaces. This surface velocity distribution resulted in a radial distribution of diffusion factor of 0.238, 0.265, and 0.288 for the hub, mean, and tip sections, respectively. Measurements of the downstream gas angle showed that this blade configuration was quite ineffective in achieving the required amount of gas turning. Further, because of high losses in the trailing edge region, the plow vortex generator did not achieve the design change in tangential velocity across the blade row. The hub, mean, and tip sections were, respectively, 16.57, 7.84, and 10.70% low with respect to the design values in effecting the correct ΔW_u across the blade row.

The level of loss was larger for the plow vortex generator than it was for the plain blade in planes located both at and far downstream of the blade

trailing edge. The overall mass averaged loss coefficients at stations 3 and 4 for the vortex generator and plain blade configurations were:

	Station			
	3		4	
	$\bar{e}$	$\bar{\omega}$	$\bar{e}$	$\bar{\omega}$
Triangular plow vortex generator	0.1034	0.1149	0.1346	0.1504
Co-rotating vane vortex generator	0.0732	0.0783	0.1329	0.1521
Plain blade	0.0959	0.1061	0.1133	0.1308

REFERENCES

1. Bettner, J. L.: Experimental Investigation in an Annular Cascade Sector of Highly Loaded Turbine Stator Blading. vol I. Analysis and Design. NASA CR-1219, 1968.

2. Stewart, W. L.: Analysis of Two-Dimensional Compressible-Flow Loss Characteristics of Turbomachine Blade Rows in Terms of Basic Boundary Layer Characteristics. NACA TN 3515. July 1955.

3. Aerodynamic Design of Axial Flow Compressors. NASA SP-36. 1965.

4. Culick, F. E. C., and Hill, J. A. F.: A Turbulent Analog of the Stewartson-Illingworth Transformation. Journal of Aeronautical Sciences. vol 25, No. 4. April 1958. pp 259-262.

Table I.

Design data for plain and vortex generator blades.

	Units	Hub	Mean	Tip
C_x	in.	1.3650	1.5925	1.8200
s	in.	1.01267	1.22967	1.44678
σ		1.3458	1.293	1.258
β_0	degrees	36.08	41.66	46.37
ψ_1	degrees	47.85	43.05	38.80
DS turning	degrees	13.0	13.0	13.0
$\left(W/W_{cr}\right)_0$		0.703	0.623	0.572
$\left(W/W_{cr}\right)_4$		0.799	0.707	0.647

Table II.

Experimental results for the plain, co-rotating vane vortex generator and triangular plow vortex generator blades.

	Plain blade		Co-rotating vane vortex generator	Triangular plow vortex generator
	With exit guide walls	Without exit guide walls		
Kinetic energy loss coefficient Exit plane (station 3)		0.0959	0.0732	0.1034
Downstream plane (station 4)		0.1133	0.1329	0.1346
Total pressure loss coefficient Exit plane (station 3)		0.1061	0.0783	0.1149
Downstream plane (station 4)		0.1308	0.1521	0.1504
Actual flow rate, lb/sec	2.33	1.24	1.192	1.330
Corrected flow rate, lb/sec	1.011	0.996	0.960	1.036
Plenum total pressure, P_{T_0}, in. Hg abs	69.709	37.481	37.741	39.597
Barometric pressure, P_{Baro}, in. Hg abs	29.309	29.306	29.341	28.997
$P_{T_0}/P_{st_{4_h}}$	1.849	1.288	1.318	1.382
P_{T_0}/P_{Baro}	2.378	1.279	1.286	1.366
Plenum total temperature, $T_{T_0}-°R$	530.0	525.0	536.0	552.0
Θ_{cr}	1.0217	1.012	1.033	1.064
δ_0	2.329	1.253	1.261	1.323
Inlet W/W_{cr}				
Hub	0.706	0.703	0.704	0.702
Mean	0.642	0.633	0.638	0.647
Tip	0.574	0.559	0.570	0.592
Change in equivalent tangential velocity across blade row, ΔW_u, ft/sec Hub		1136.01	1237.08	1041.01
Mean		940.59	971.37	947.10
Tip		776.91	832.09	780.19

Table III.

Experimental and design values of suction surface diffusion
factors for the plain, co-rotating vane vortex generator and
triangular plow vortex generator blades.

(Based on an isentropic surface velocity distribution)

	Plain blade		Co-rotating vane vortex generator	Triangular plow vortex generator	Design value
	With downstream guide walls	Without downstream guide walls			
Hub	0.243	0.330	0.278	0.238	0.400
Mean	0.362	0.332	0.303	0.265	0.400
Tip	0.354	0.312	0.208	0.288	0.400

The y-axis is labeled "Corrected inlet total pressure, P_T/δ_0" with values 13.0, 14.0, 15.0.
The x-axis is labeled "Radius—in." with values 10.0, 11.0, 12.0, 13.0, 14.0, 15.0.

5315II-1
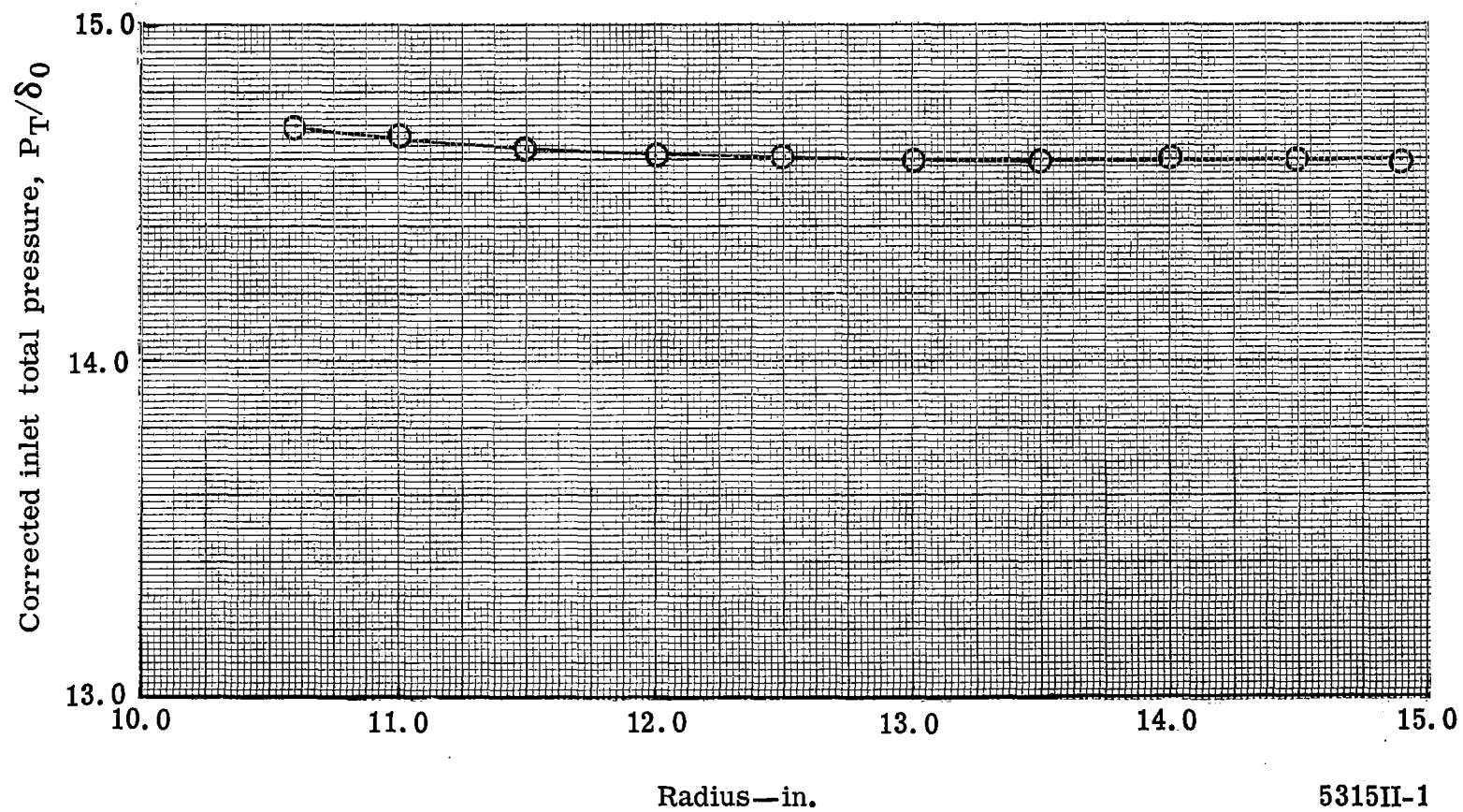
Figure 1. Inlet total pressure radial survey performed on the center blade passage mean section extended midchannel line—approximately 0.75 in. upstream of blade leading edge.
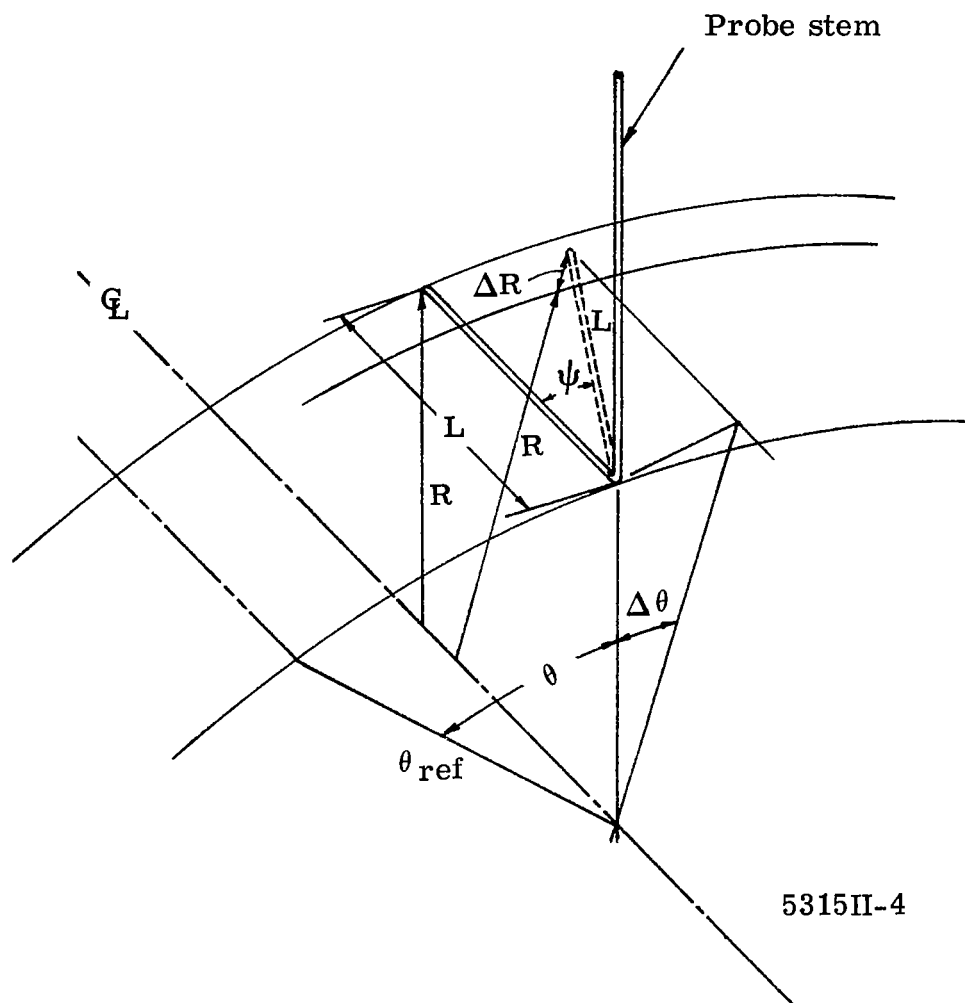
Figure 4. Schematic of prism probe for calculation of probe
tip spatial location.
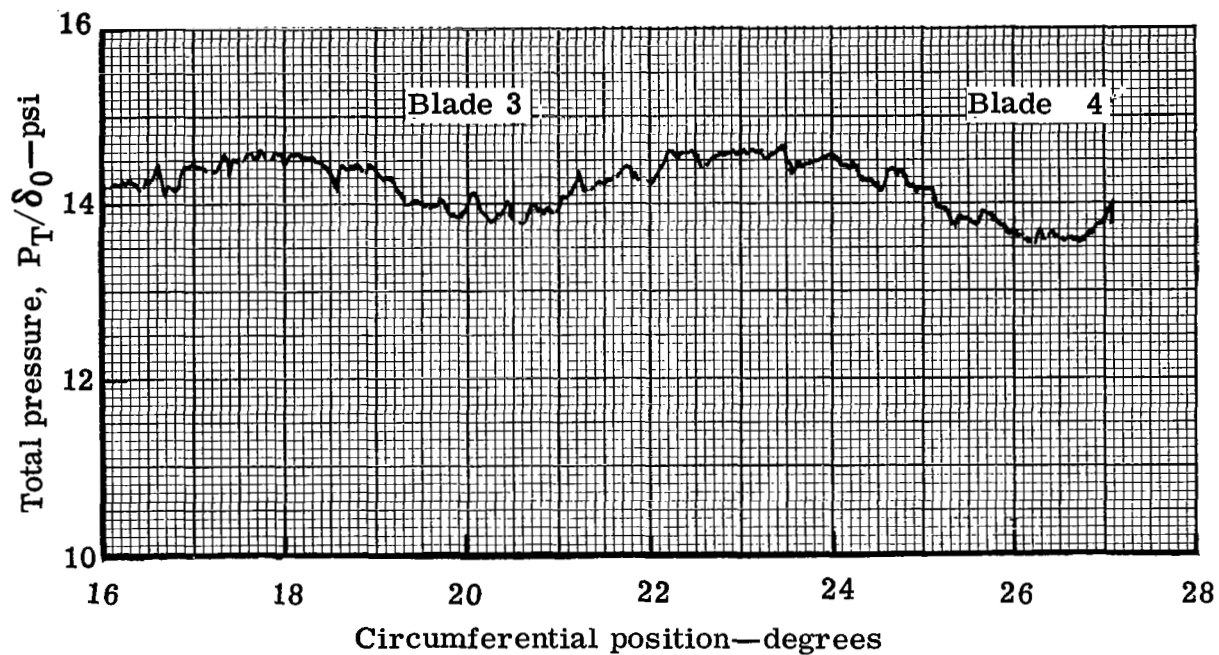
Figure 5. Plain blade downstream wake survey total pressure distribution for radial position R = 13.00 in.
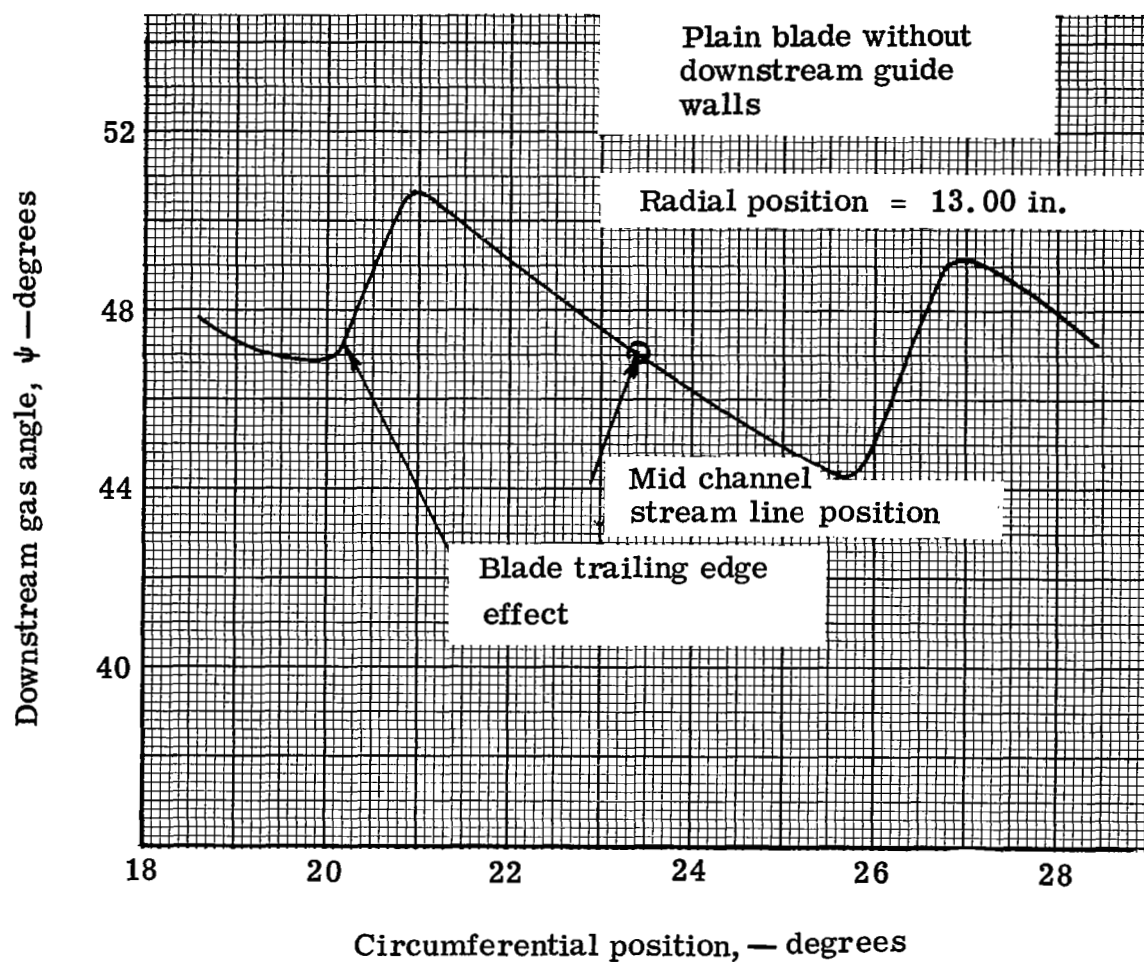
Figure 6. Plain blade circumferential variation of downstream gas angle for radial position R = 13.00 in.

Plain blade exit wake survey
Kinetic energy loss coefficient distribution at station 3 for radial position = 12.97
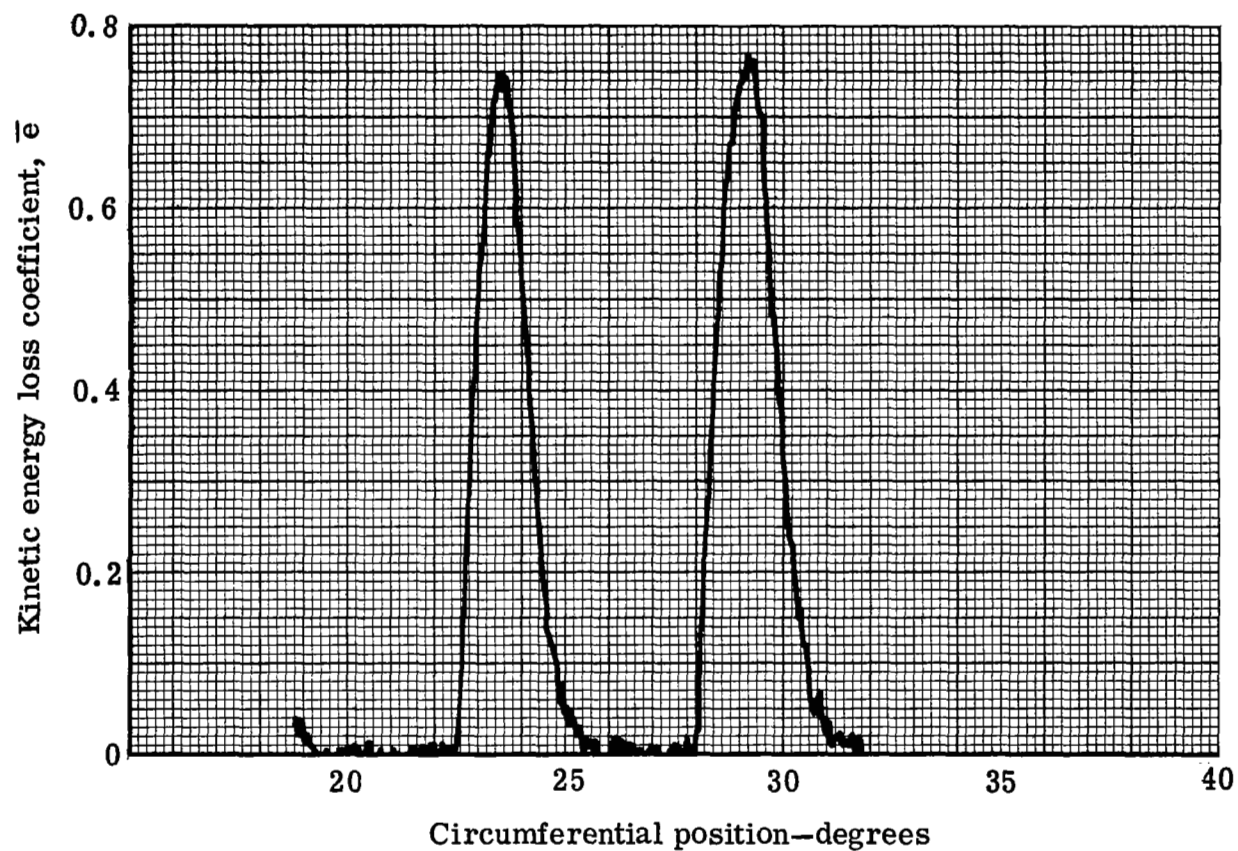
Figure 7. Plain blade circumferential variation of exit wake survey kinetic energy loss coefficient for radial position R = 12.97 in.
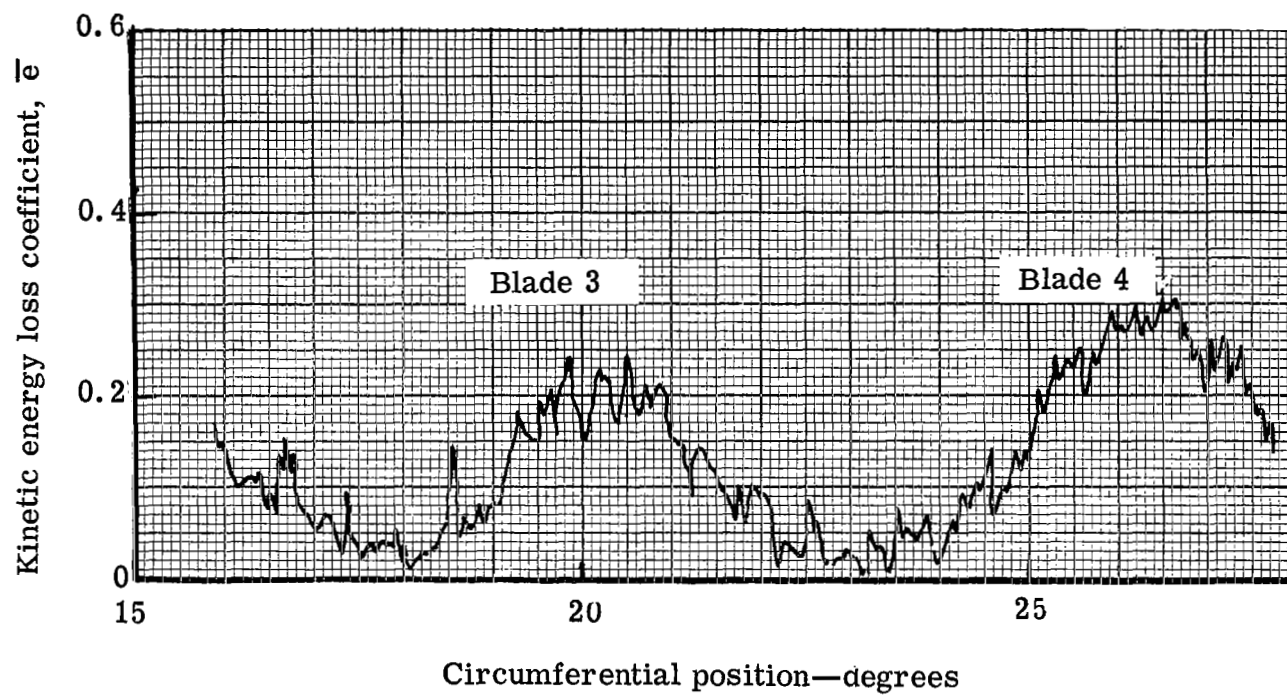
5315Ⅱ-7

Figure 8. Plain blade circumferential variation of downstream wake survey kinetic energy loss coefficient for radial position R = 13.00 in.
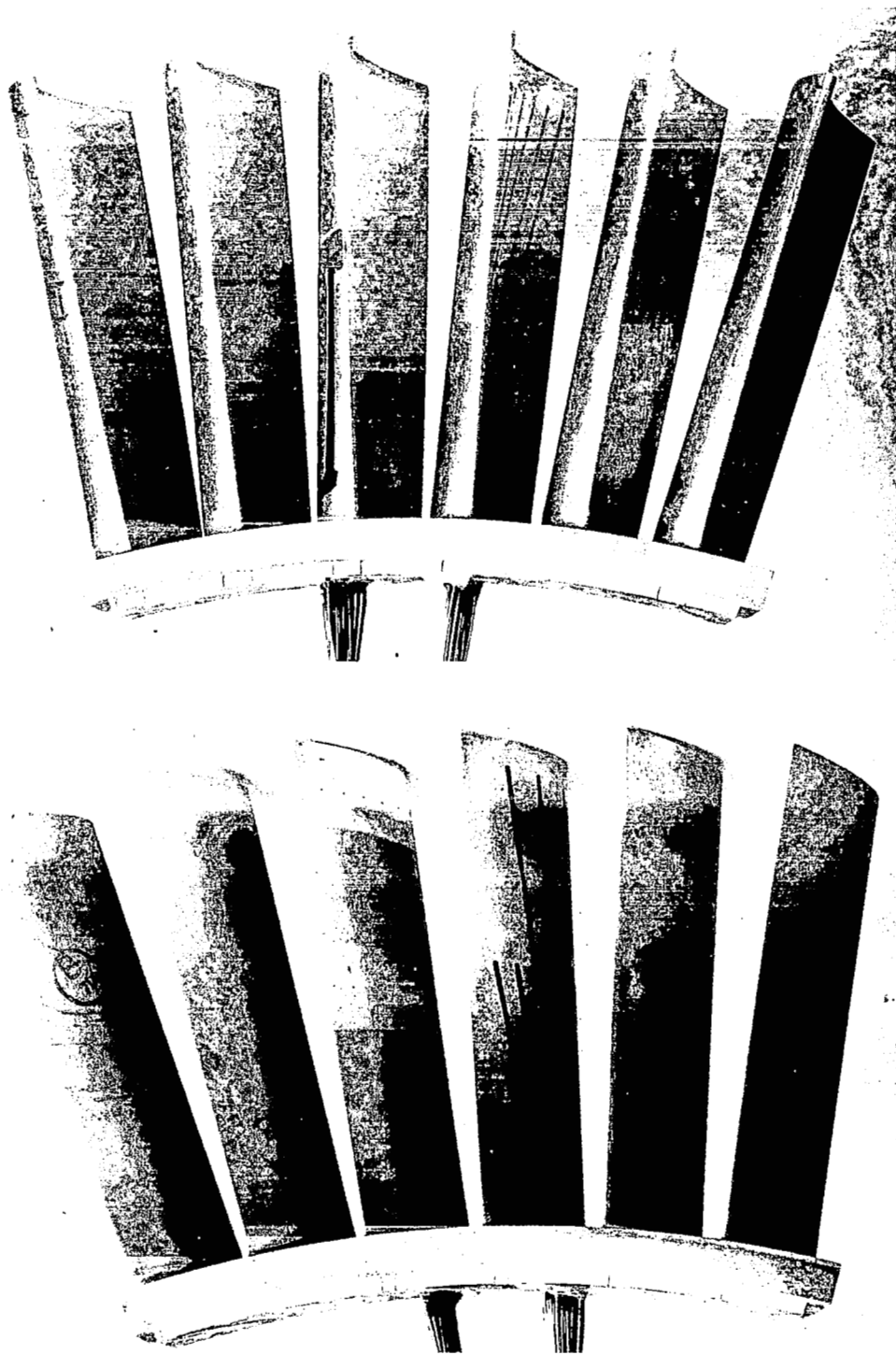
Figure 9.   Plain blade assembly.
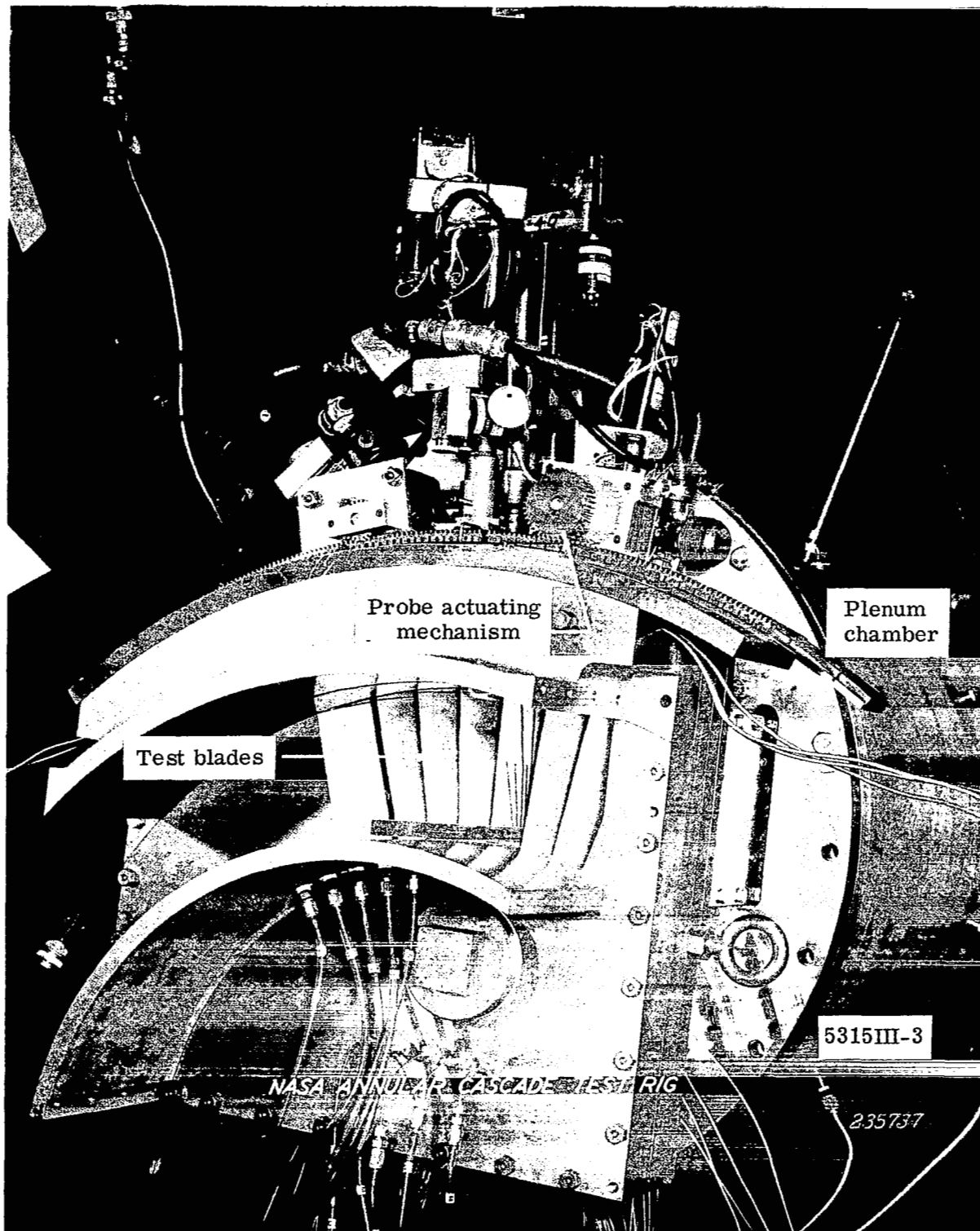
Figure 10. Annular cascade test rig.
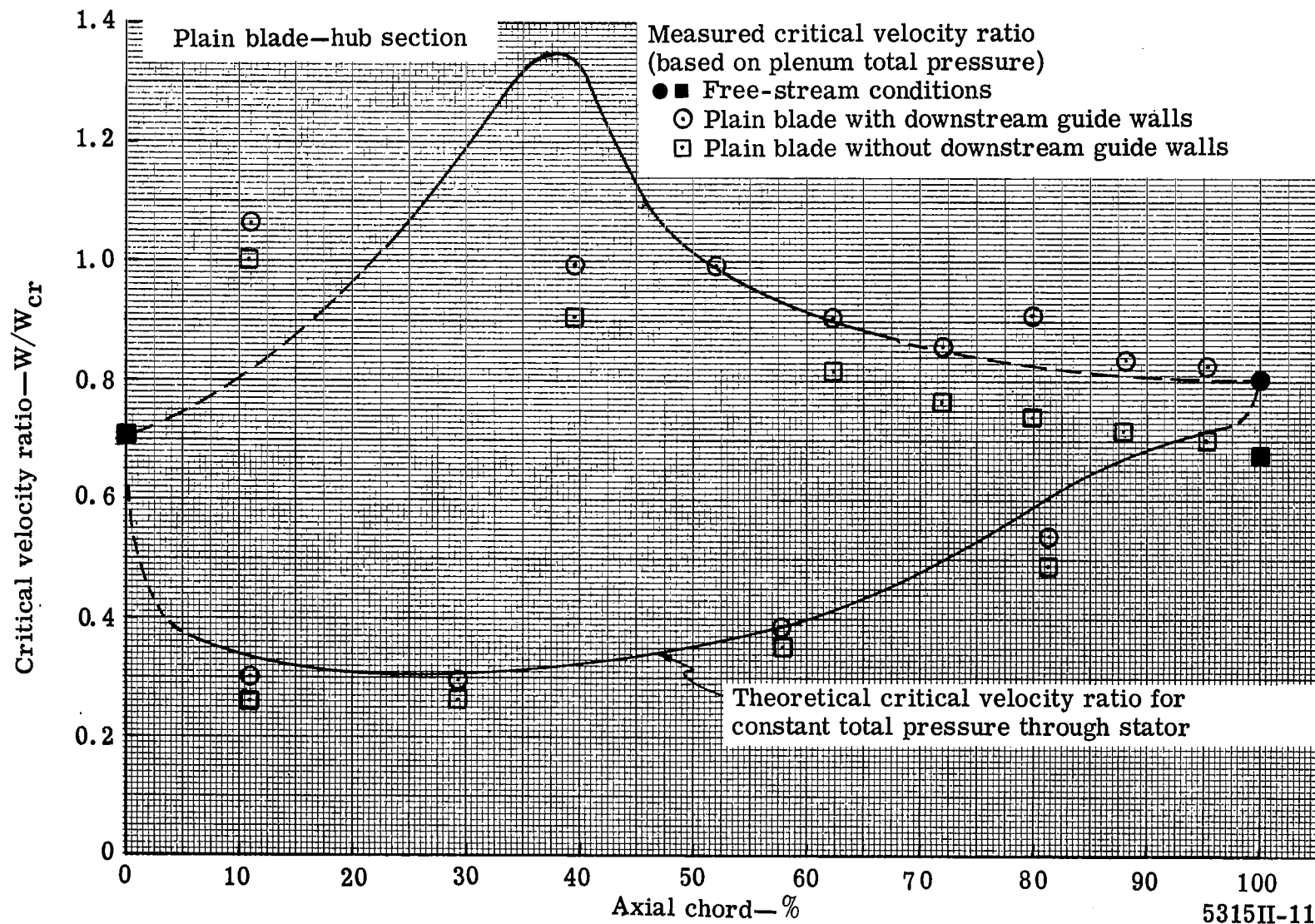
Figure 11. Measured and predicted surface critical velocity ratio distribution for plain blade hub section.
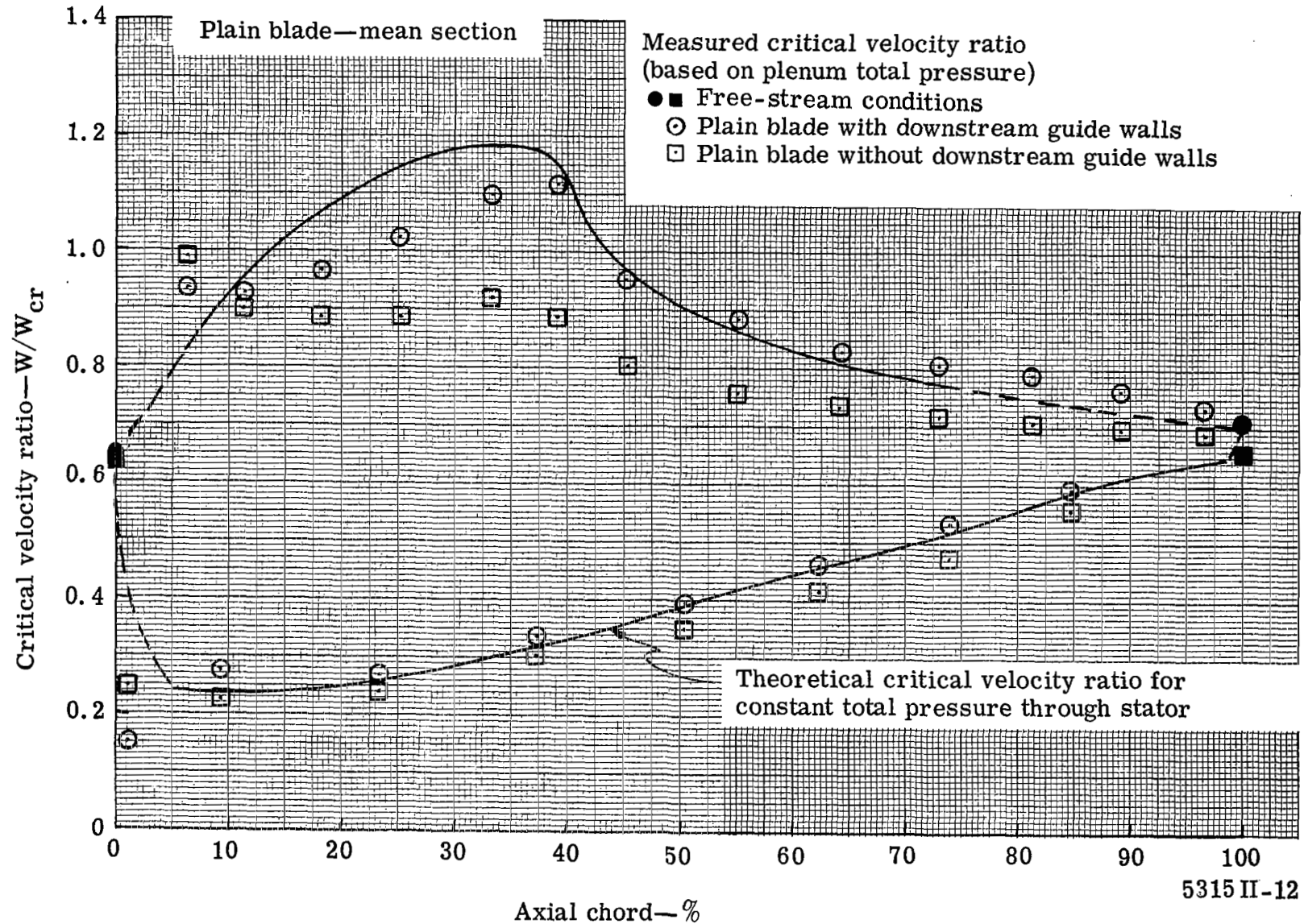
Figure 12. Measured and predicted surface critical velocity ratio distribution for plain blade mean section.
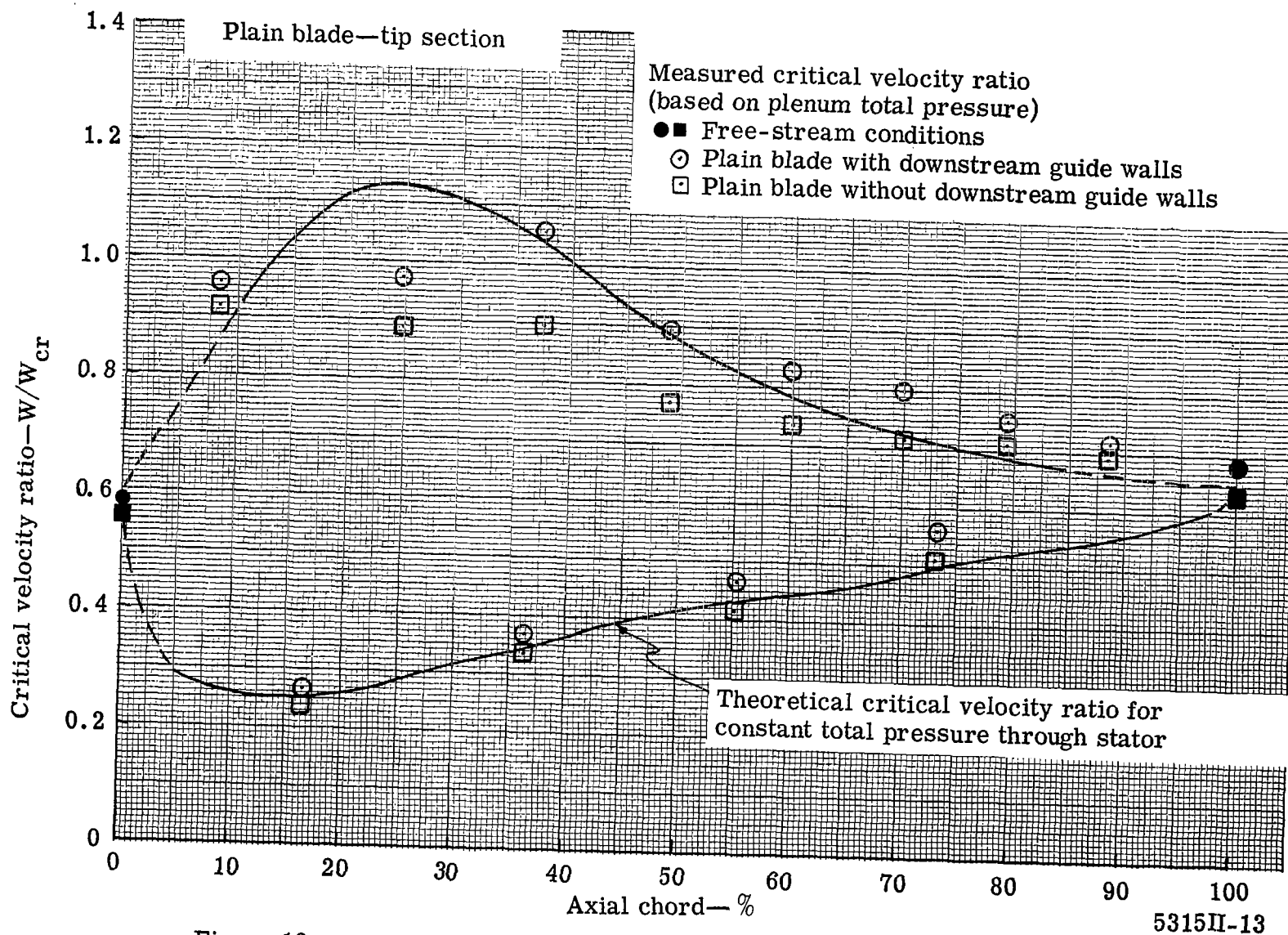
5315 II-12

Figure 13. Measured and predicted surface critical velocity ratio distribution for plain blade tip section.
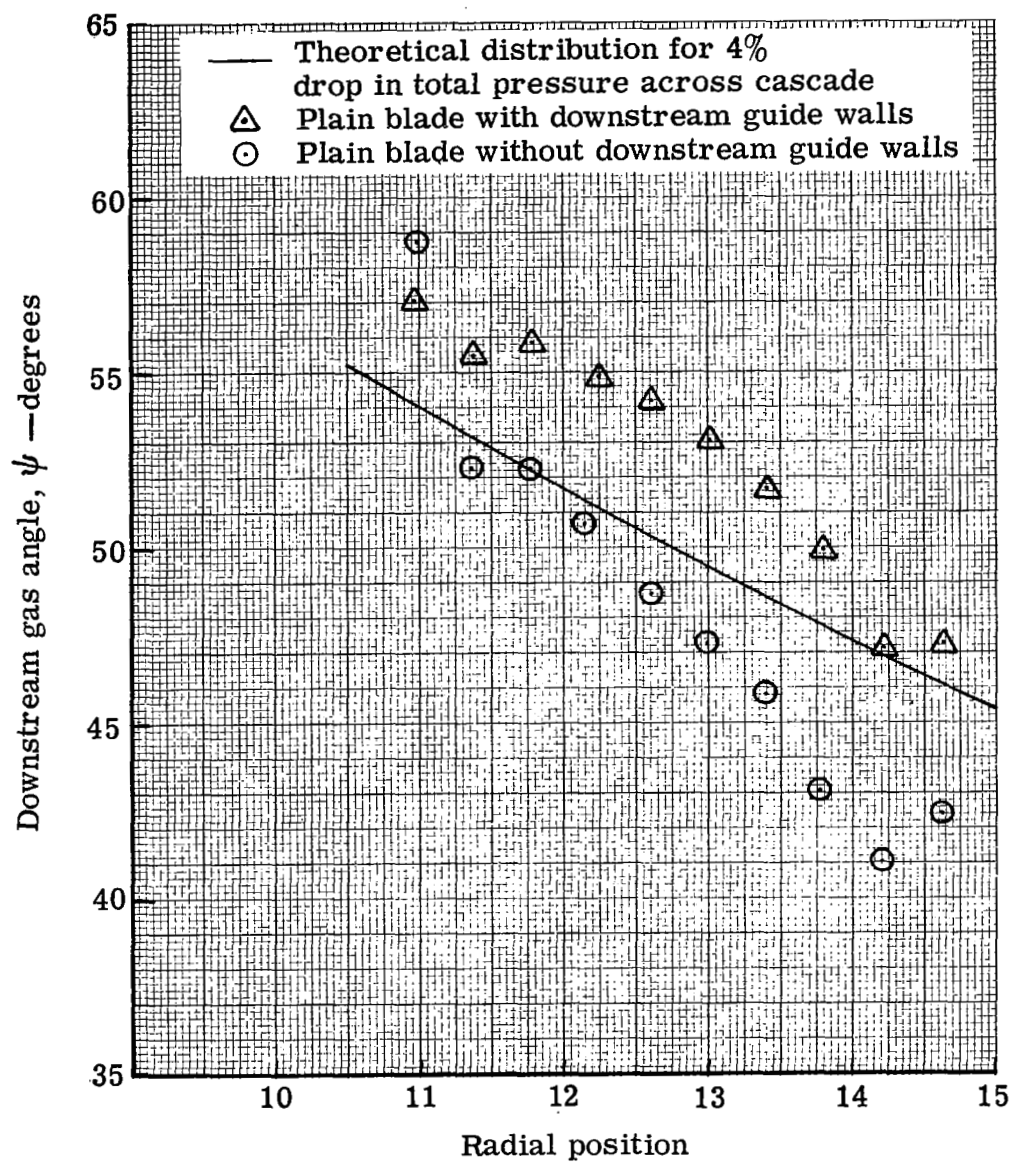
5315II-13

Figure 14. Measured and predicted radial variation of the plain blade average downstream gas angle.
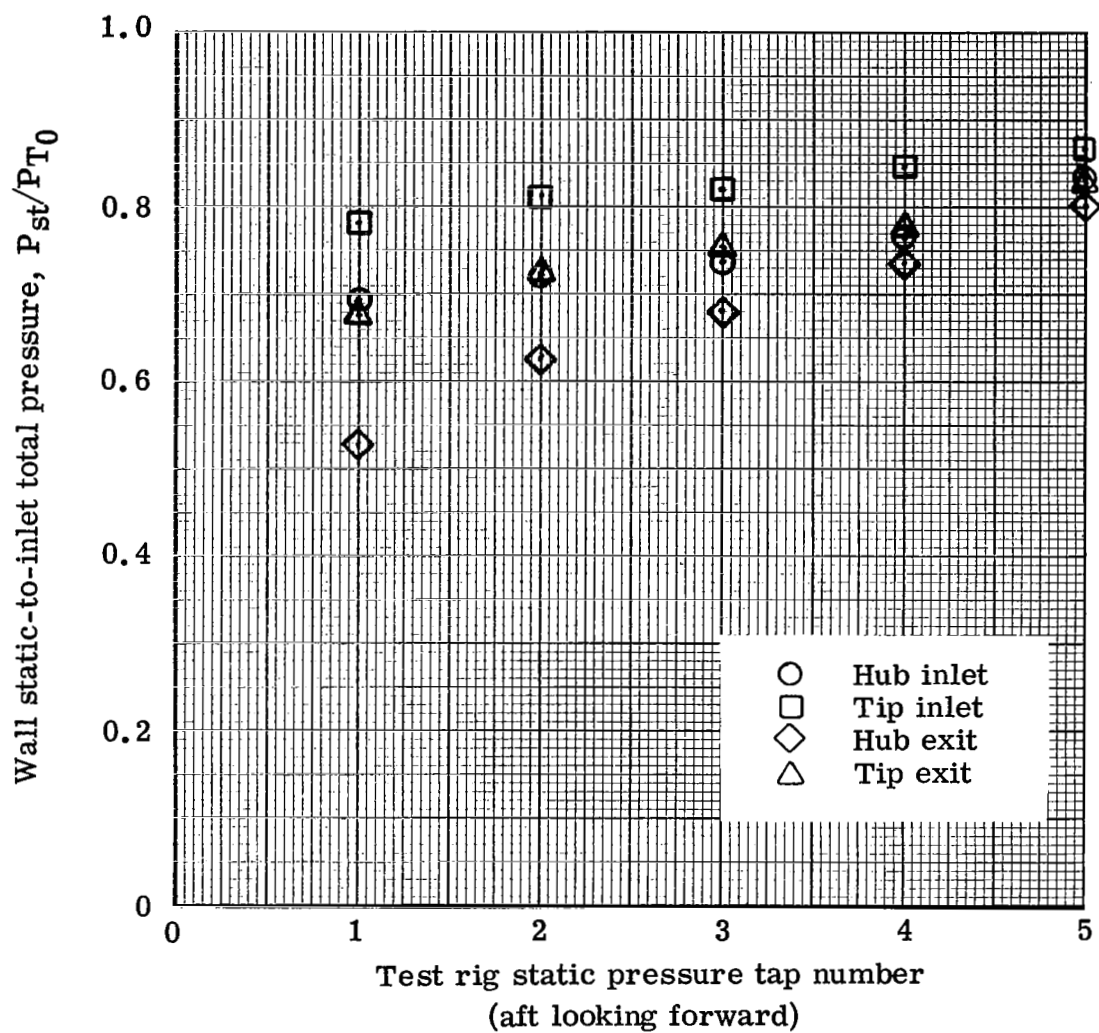
Figure 15. Circumferential variation of static pressure on inlet and exit hub and tip walls for plain blade with downstream guide walls in place.

5315II-15

P_{st}/P_{T_0} { with exit guide walls } 0.821 0.756 0.714
{ without exit guide walls } 0.822 0.788 0.778

Tip

P_{T_0}

Blade row

2 in.

6 in.

P_{amb}

Hub

P_{st}/P_{T_0} { with guide walls } 0.738 0.680 0.540
{ without guide walls } 0.742 0.755 0.777

| Inlet plane | Exit plane | Downstream plane | Exit of rig |

1.0

0.8

0.6

0.4

Free-stream critical velocity ratio, W/W_{cr}

with exit guide walls
without exit guide walls

Hub

Tip

Axial distance—in.
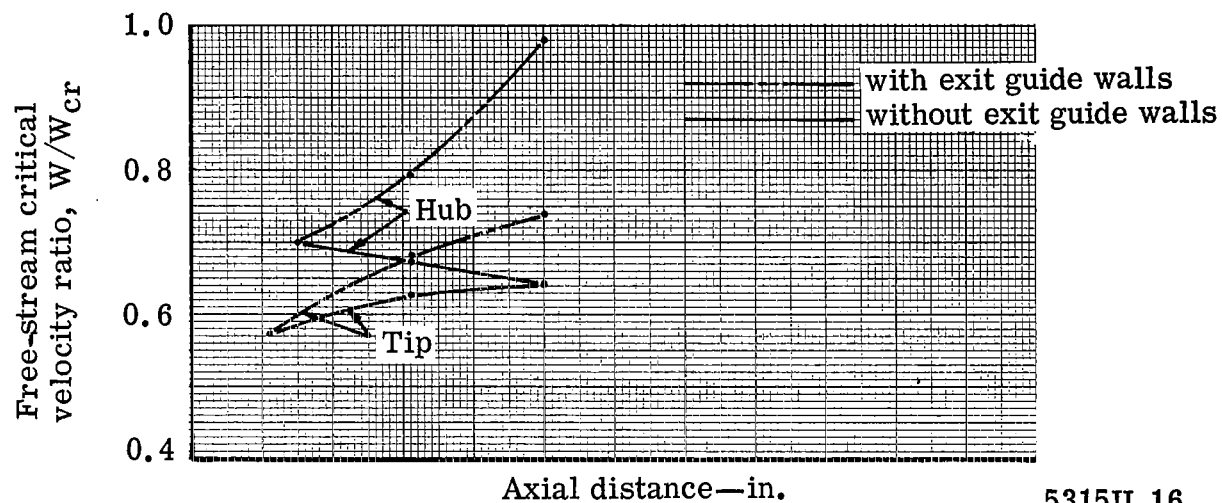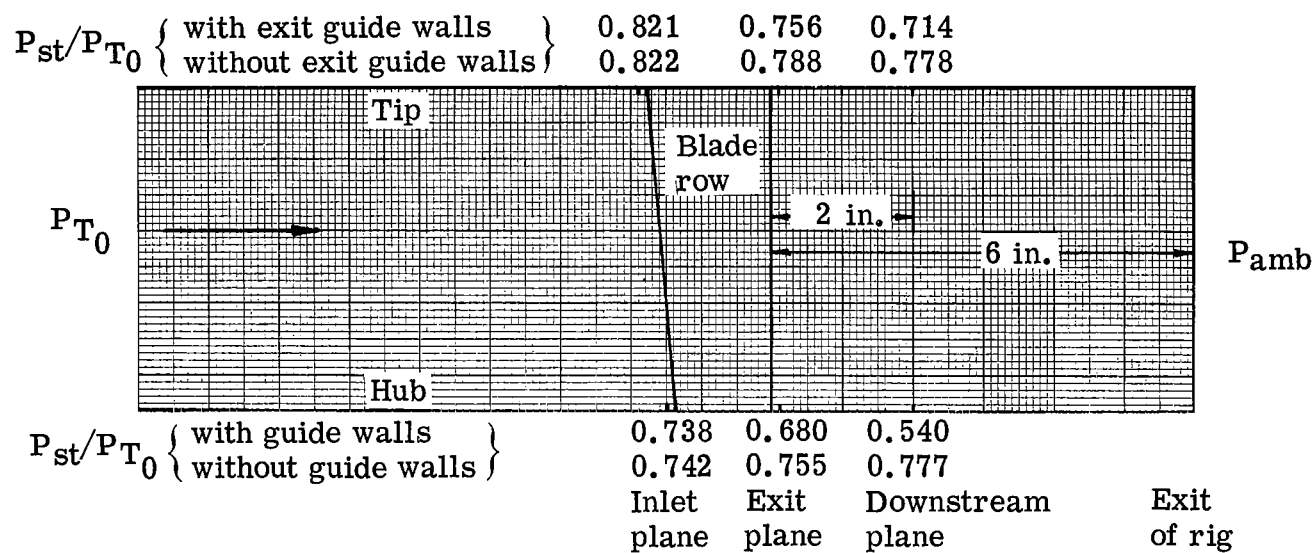
5315II-16

Figure 16. Effect of exit guide walls on the free-stream velocity through the test rig.
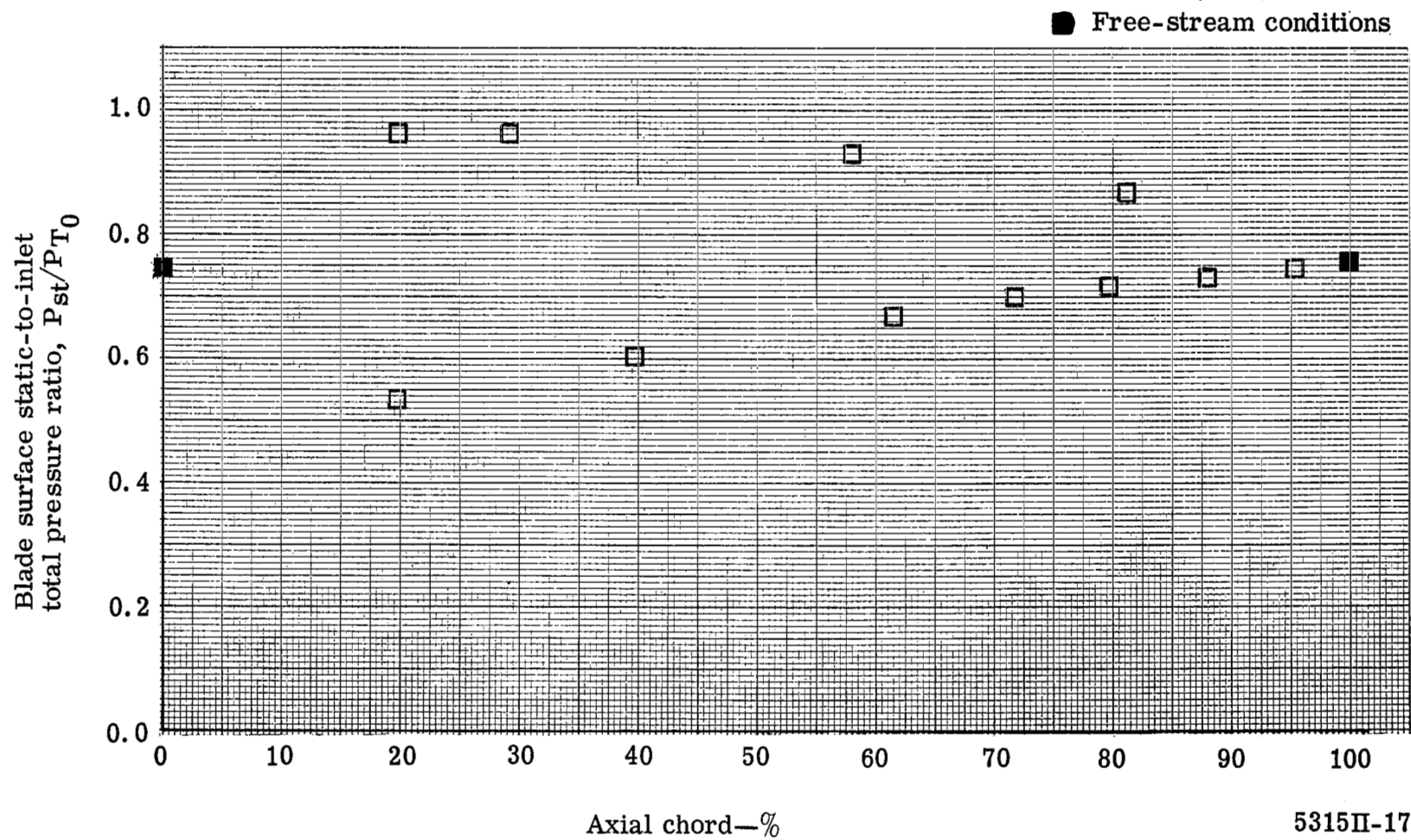
Figure 17. Measured surface static pressure distribution for the plain blade without downstream guide walls—hub section.

5315Ⅱ-17
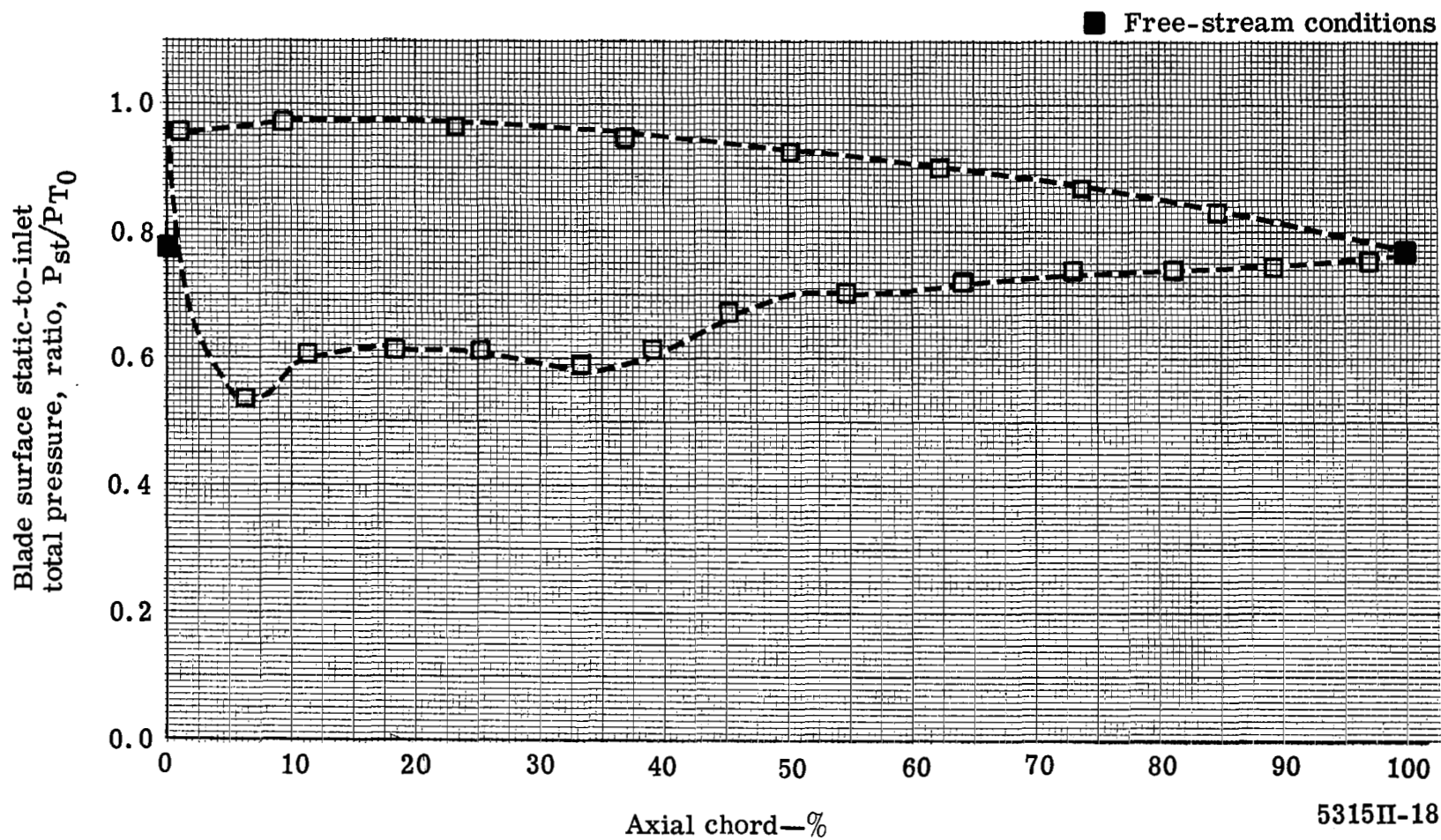
Figure 18. Measured surface static pressure distribution for the plain blade without
downstream guide walls—mean section.

5315II-18

■ Free-stream conditions
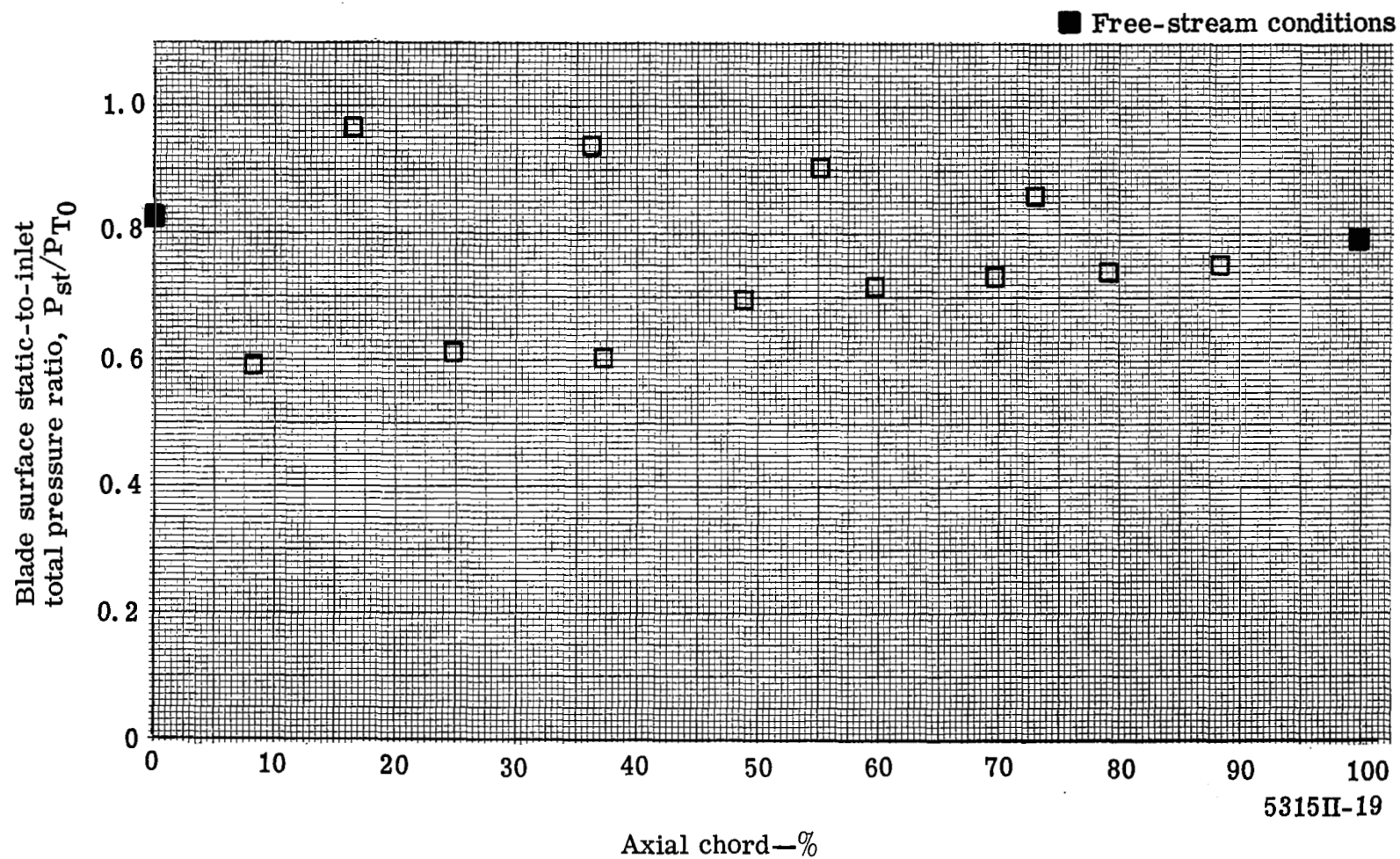
Figure 19. Measured surface static pressure distribution for the plain blade without downstream guide walls—tip section.
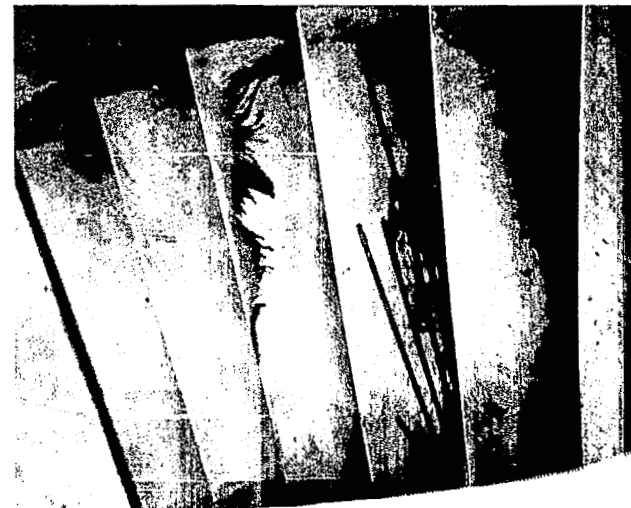
5315II-19

69
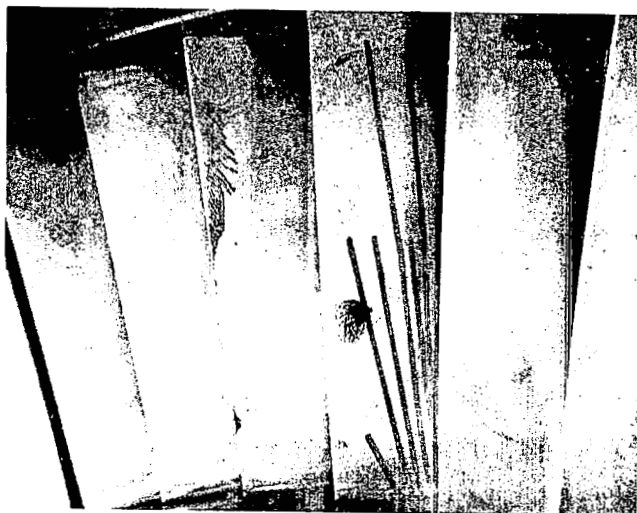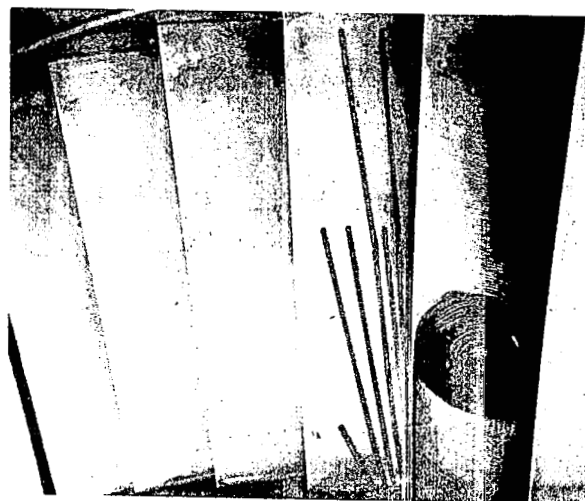
Vane No. 3

Vane No. 4

Vane No. 5

Figure 20. Plain blade flow visualization results for inlet hub static-to-total pressure ratio of 0. 65 (below design value).
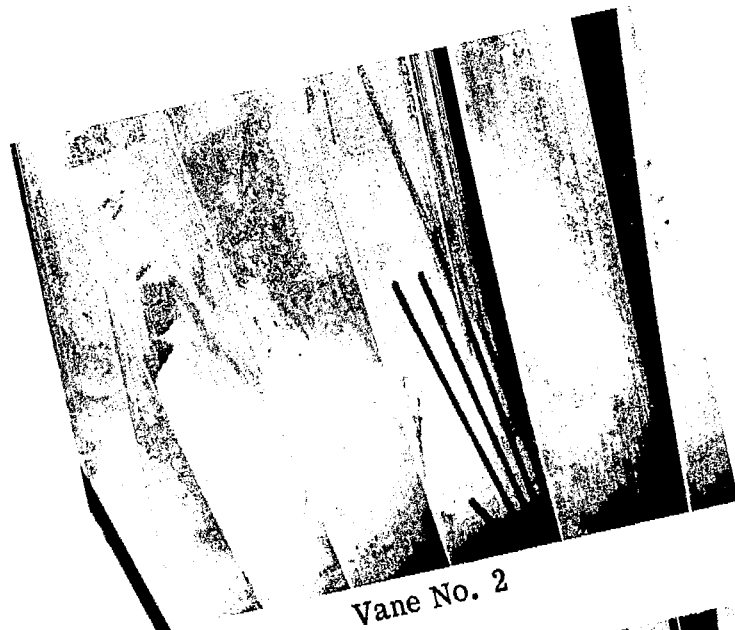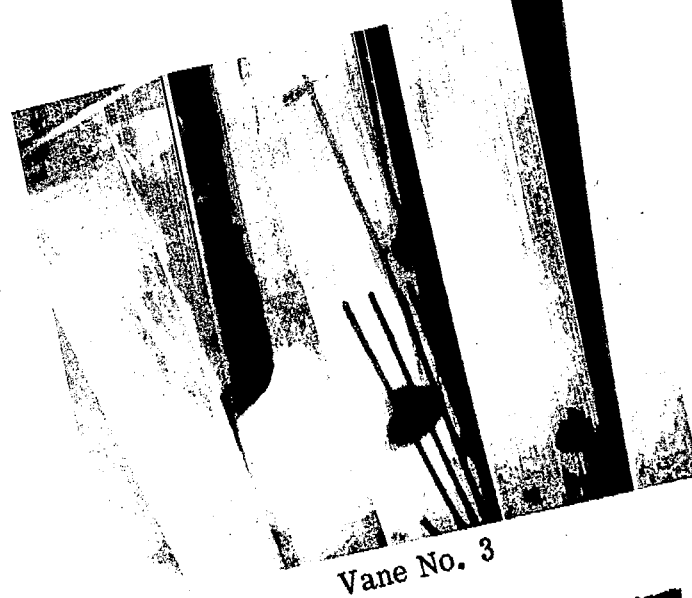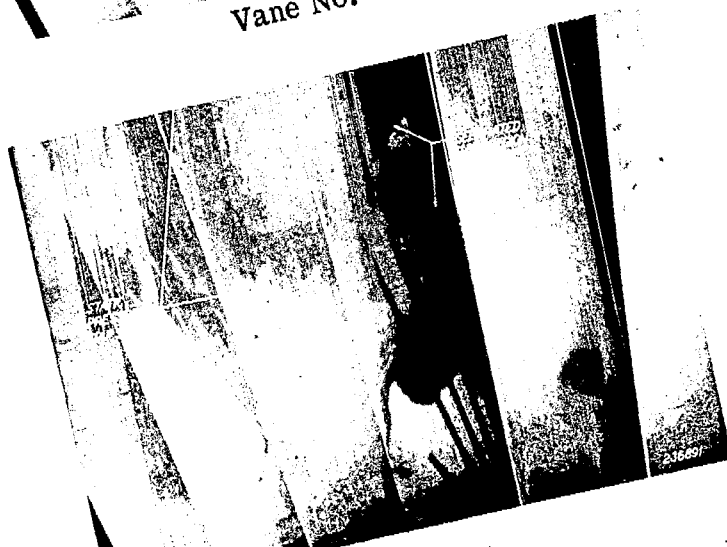
Vane No. 2

Vane No. 3

Vane No. 5

lization results for inlet hub static-to-total
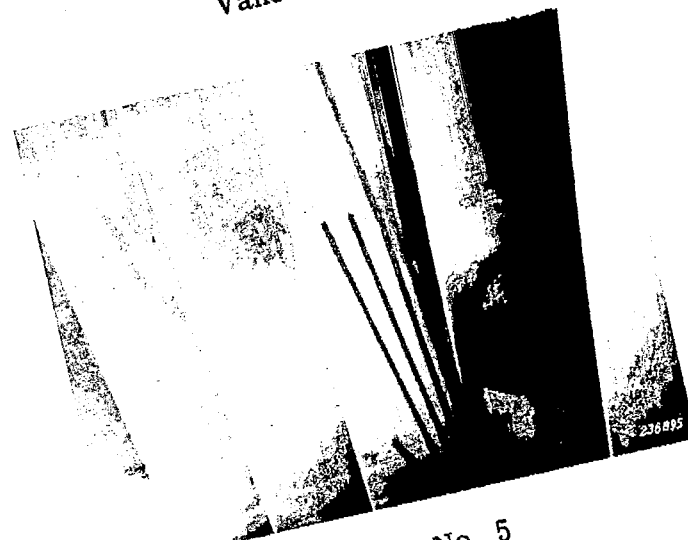
Vane No. 2
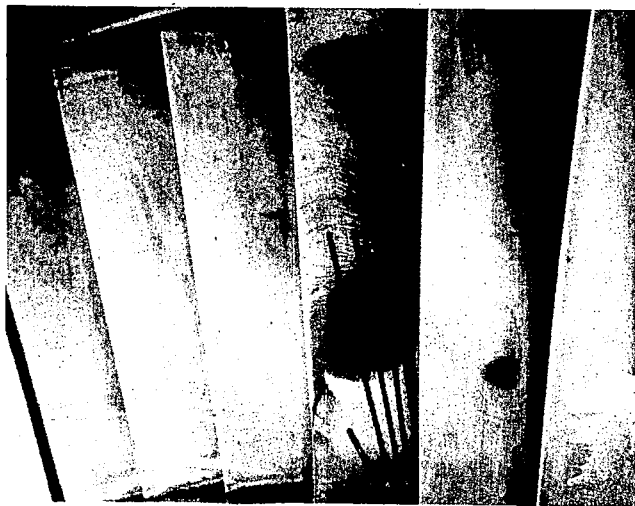
Vane No. 3

Vane No. 4

Vane No. 5

Figure 22.   Plain blade flow visualization results for inlet hub static-to-total
pressure ratio of 0. 82 (above design value).
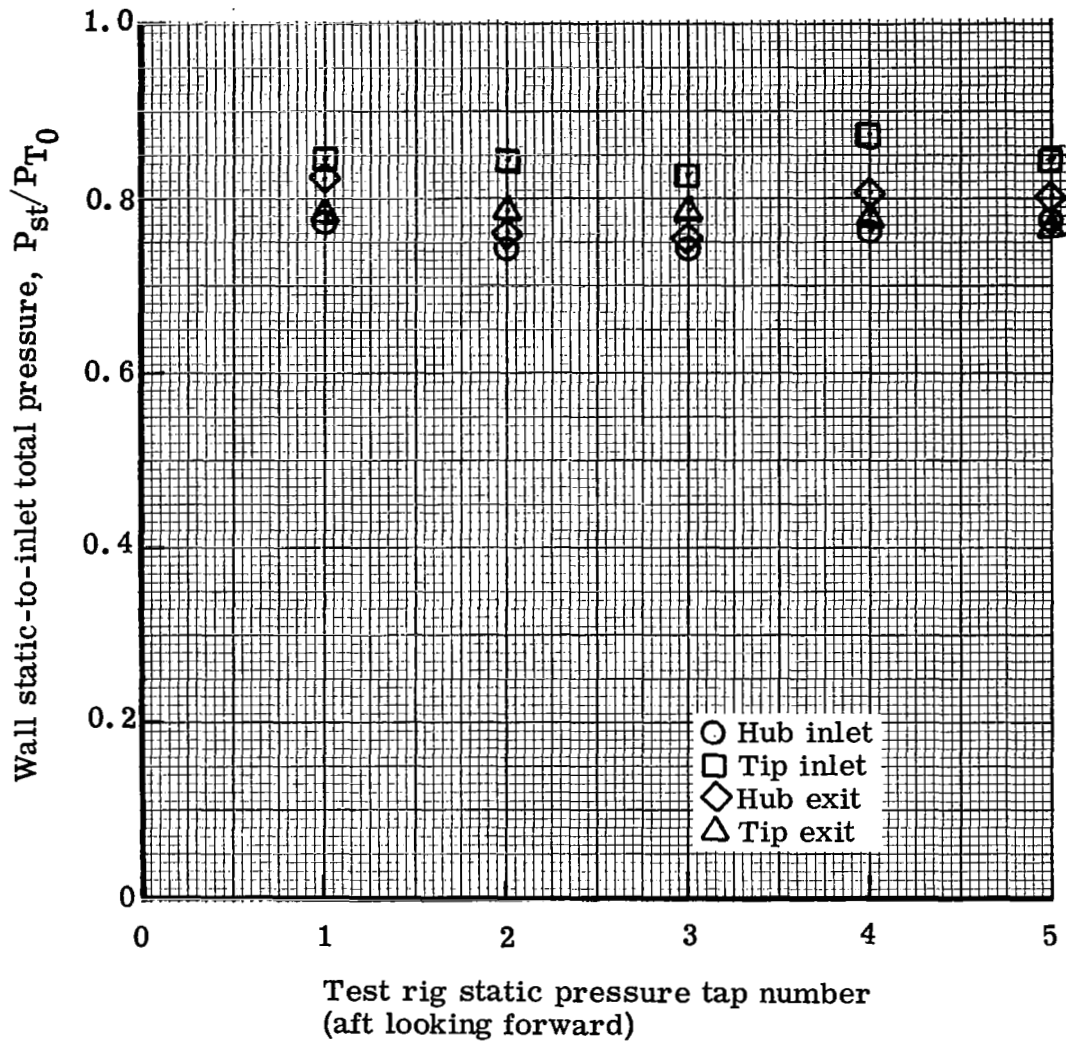
Figure 23. Circumferential variation of static pressure on inlet and exit hub and tip walls for plain blade without downstream guide walls in place.
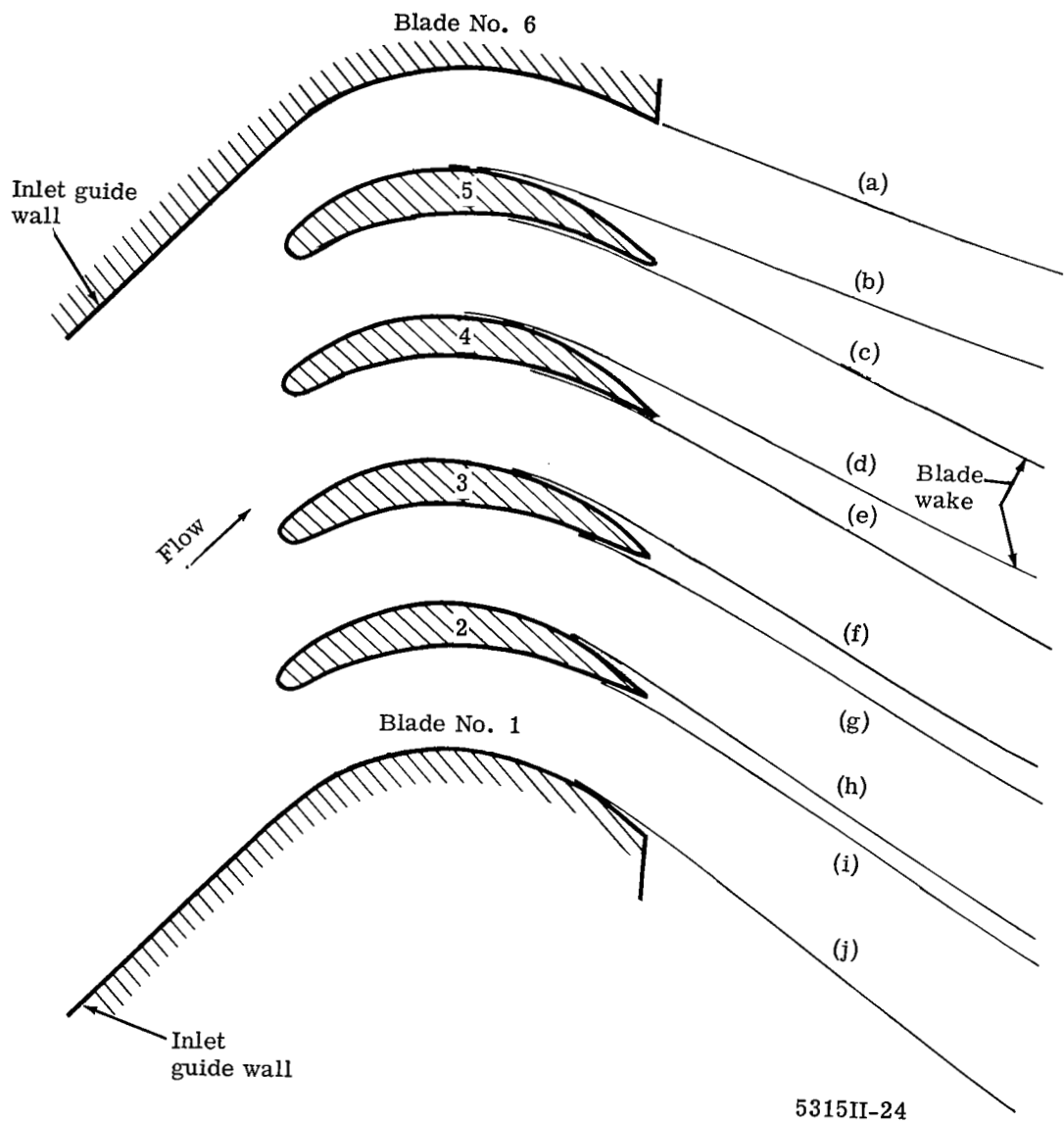
Figure 24. Schematic representation of blade wake
circumferential variation.
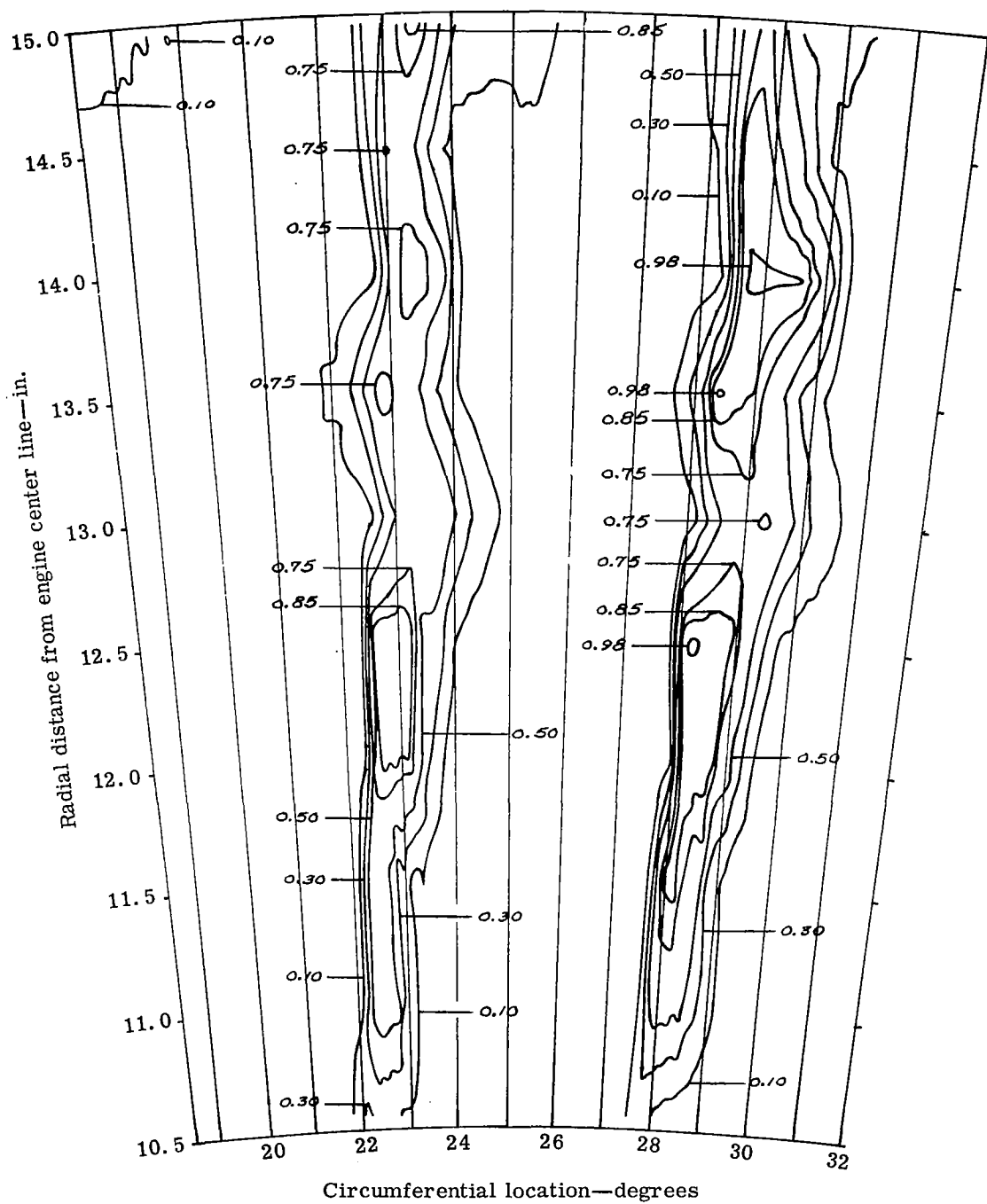
5315JI-25

Figure 25. Contours of kinetic energy loss coefficient across one blade passage—plain blade exit wake survey.

75
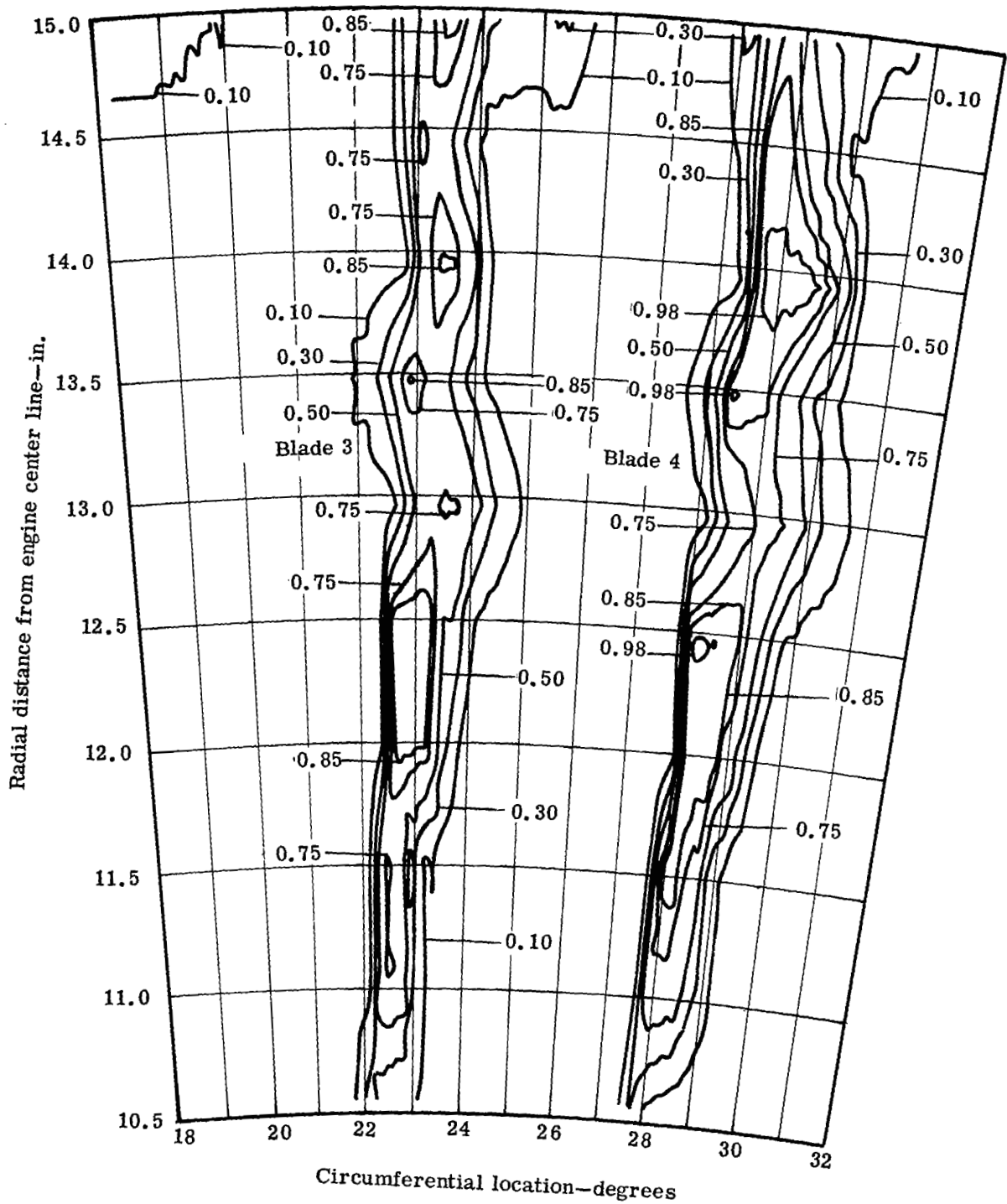
Figure 26. Contours of total pressure loss coefficient across one blade passage—plain blade exit wake survey.

5315 II-26

Figure 27. Contours of kinetic energy loss coefficient—plain blade downstream wake survey.
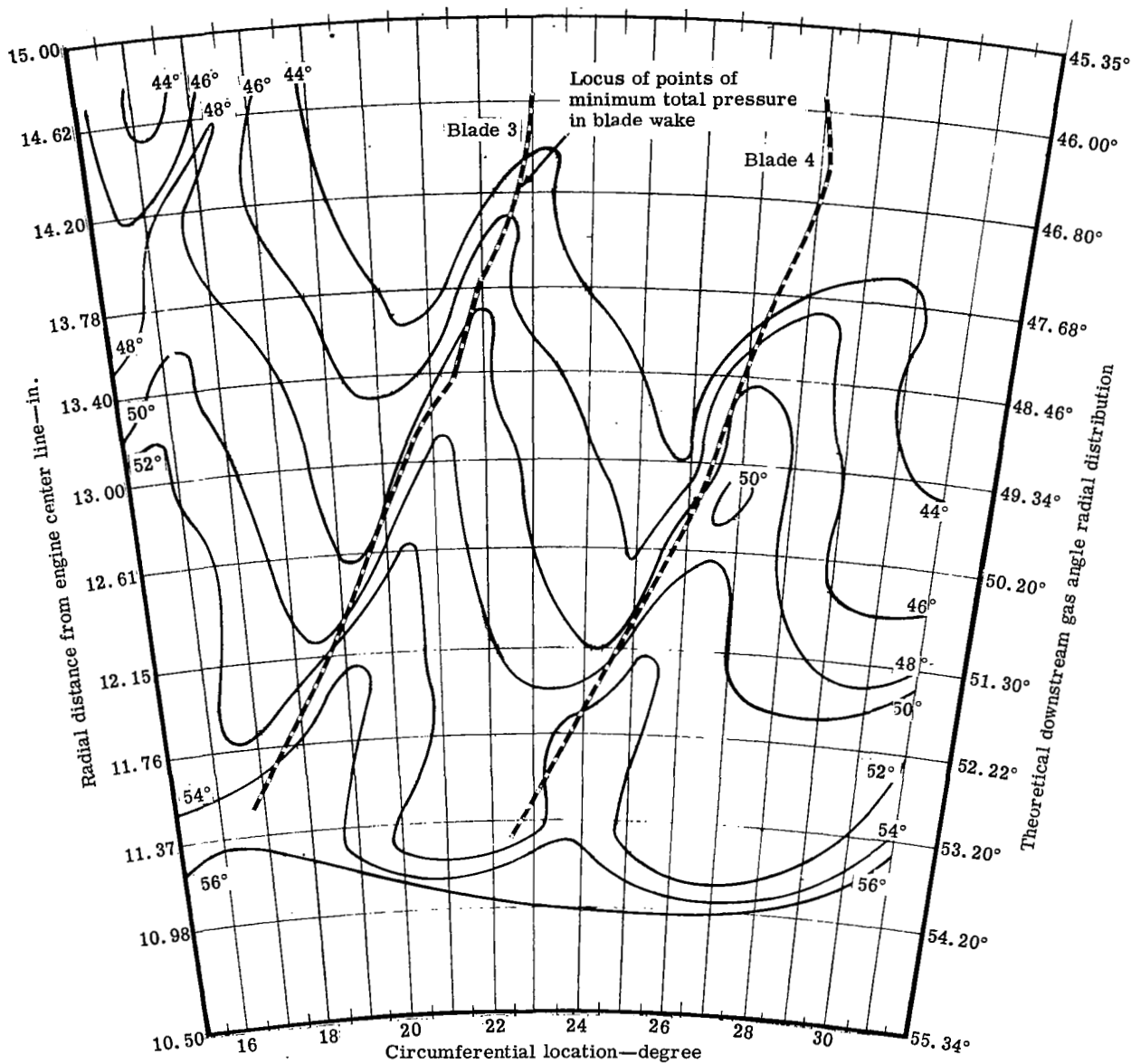
5315II-27

Figure 28. Contours of downstream gas angle—measured from axial—plain blade downstream wake survey.
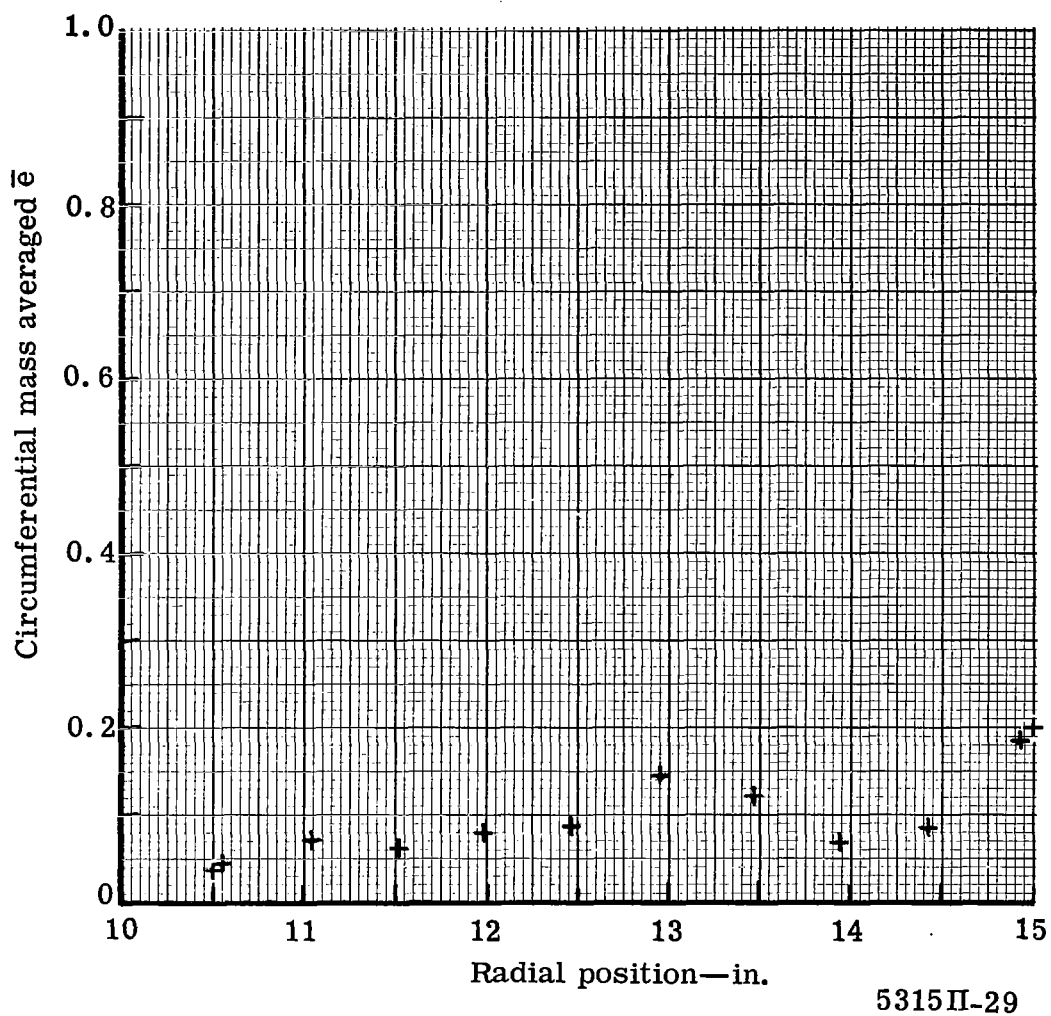
Figure 29. Plain blade exit wake survey—kinetic energy loss coefficient distribution at station 3.
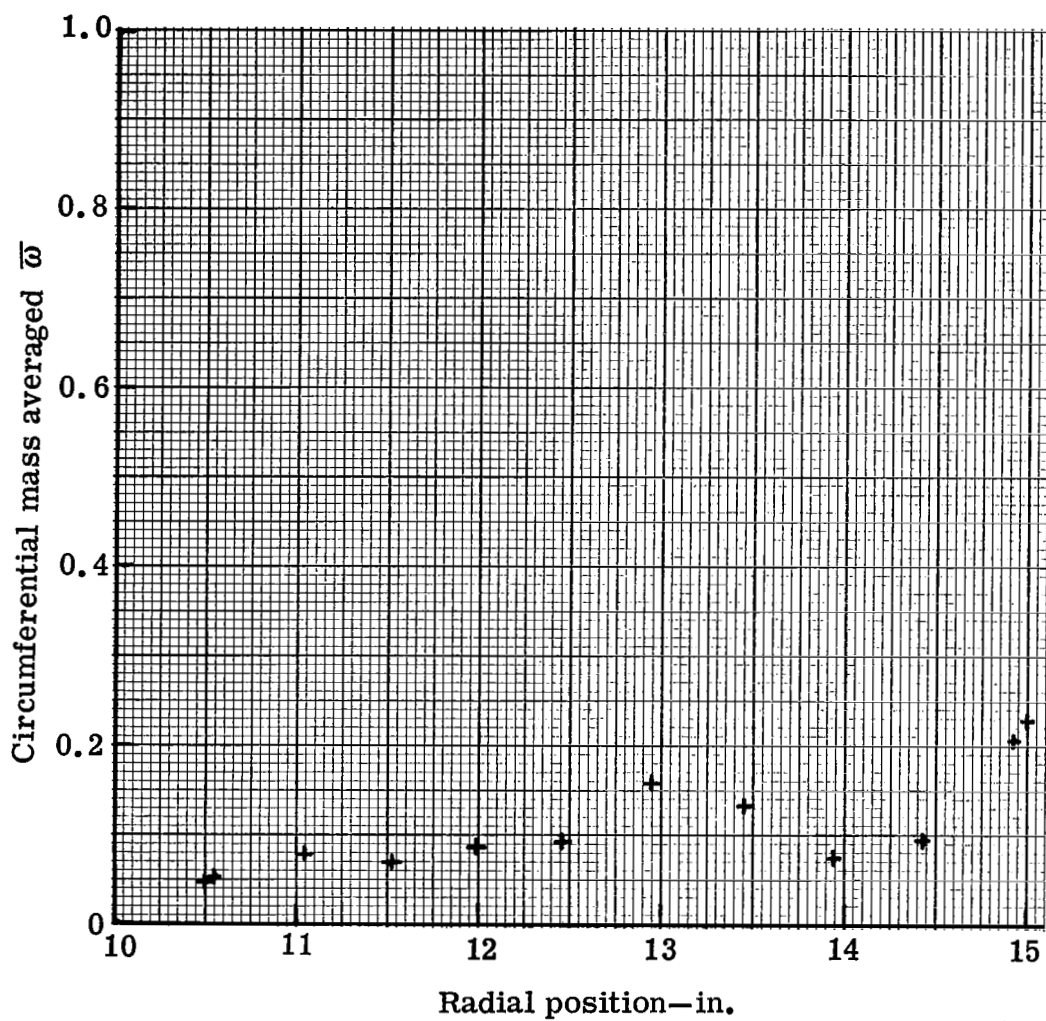
Figure 30. Plain blade exit wake survey—total pressure loss coefficient distribution at station 3.

5315-30
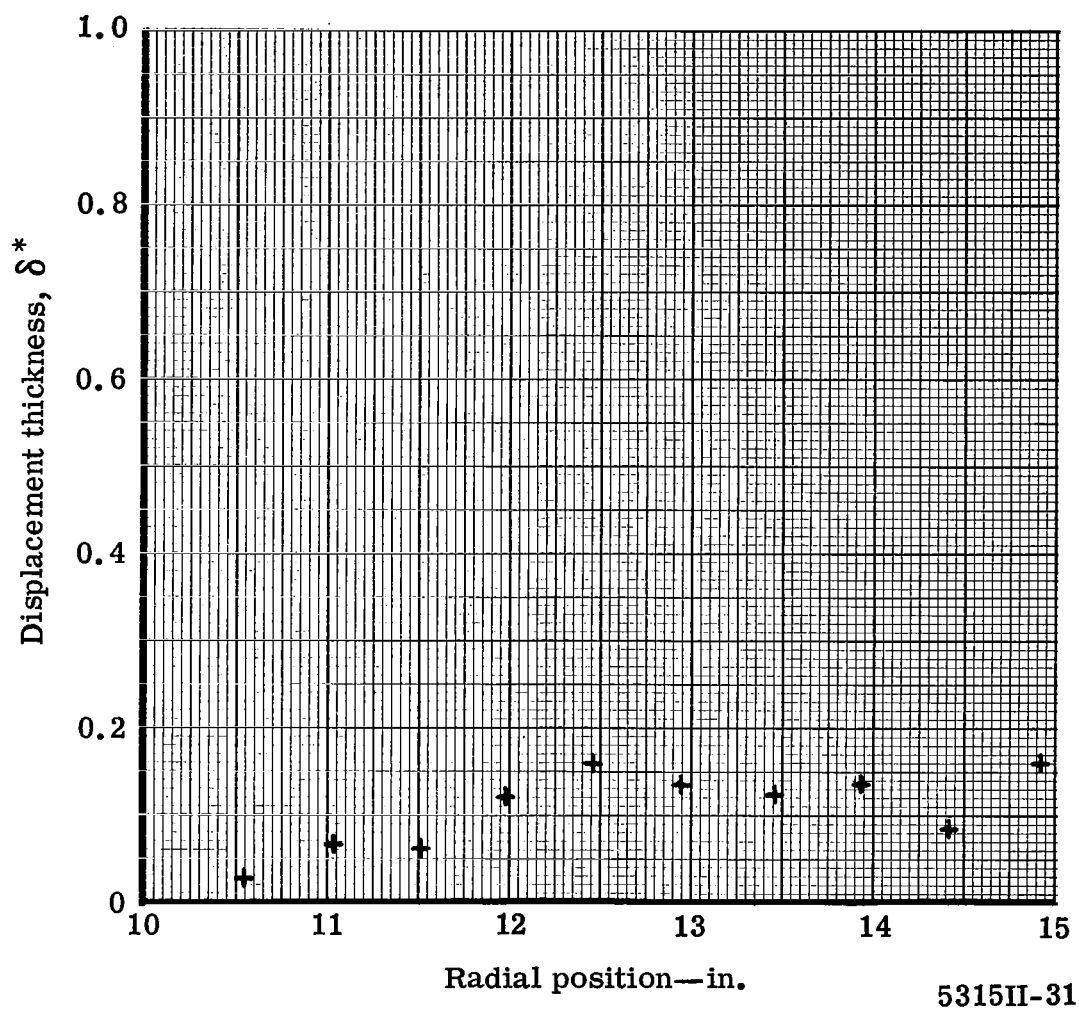
Figure 31.   Plain blade exit wake survey—displacement thickness
distribution at station 3.
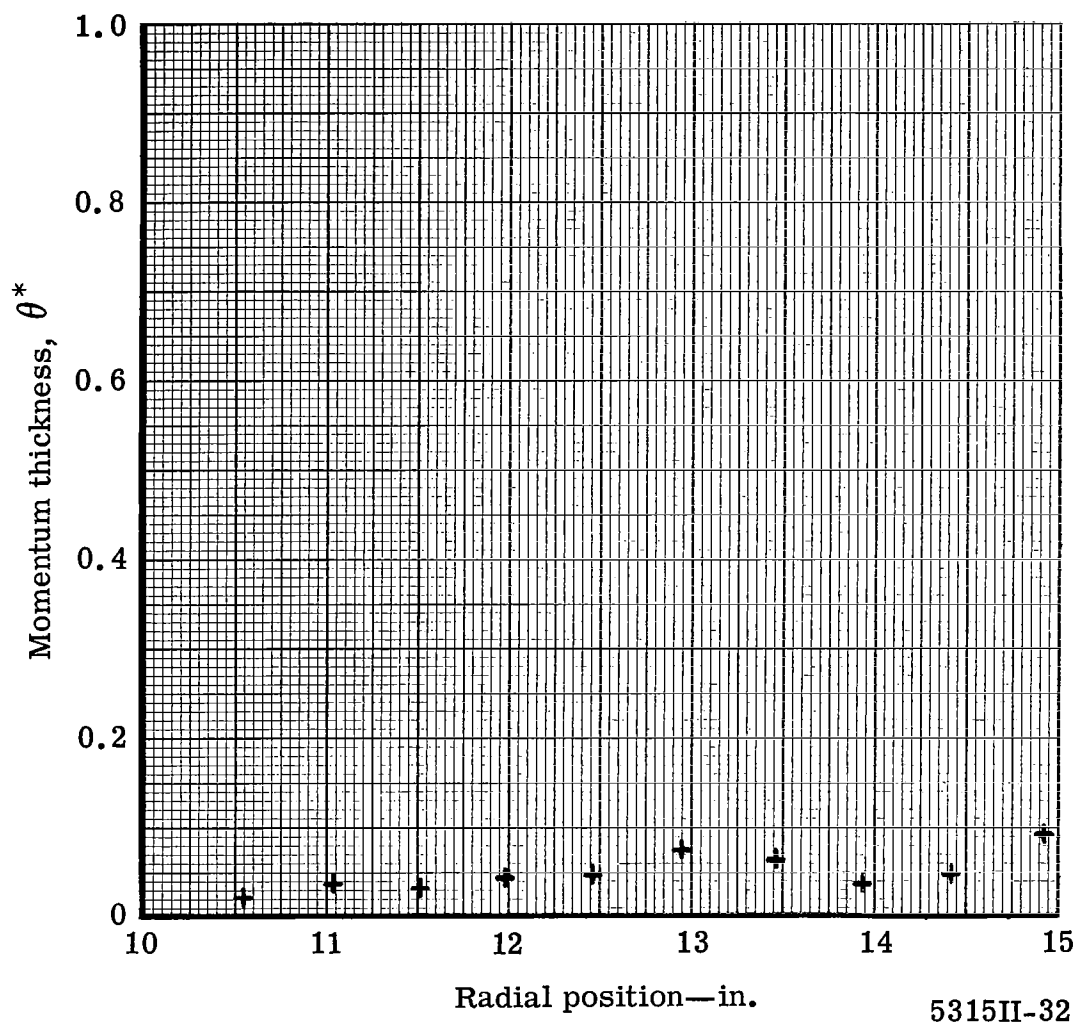
5315II-31

Figure 32. Plain blade exit wake survey—momentum thickness distribution at station 3.
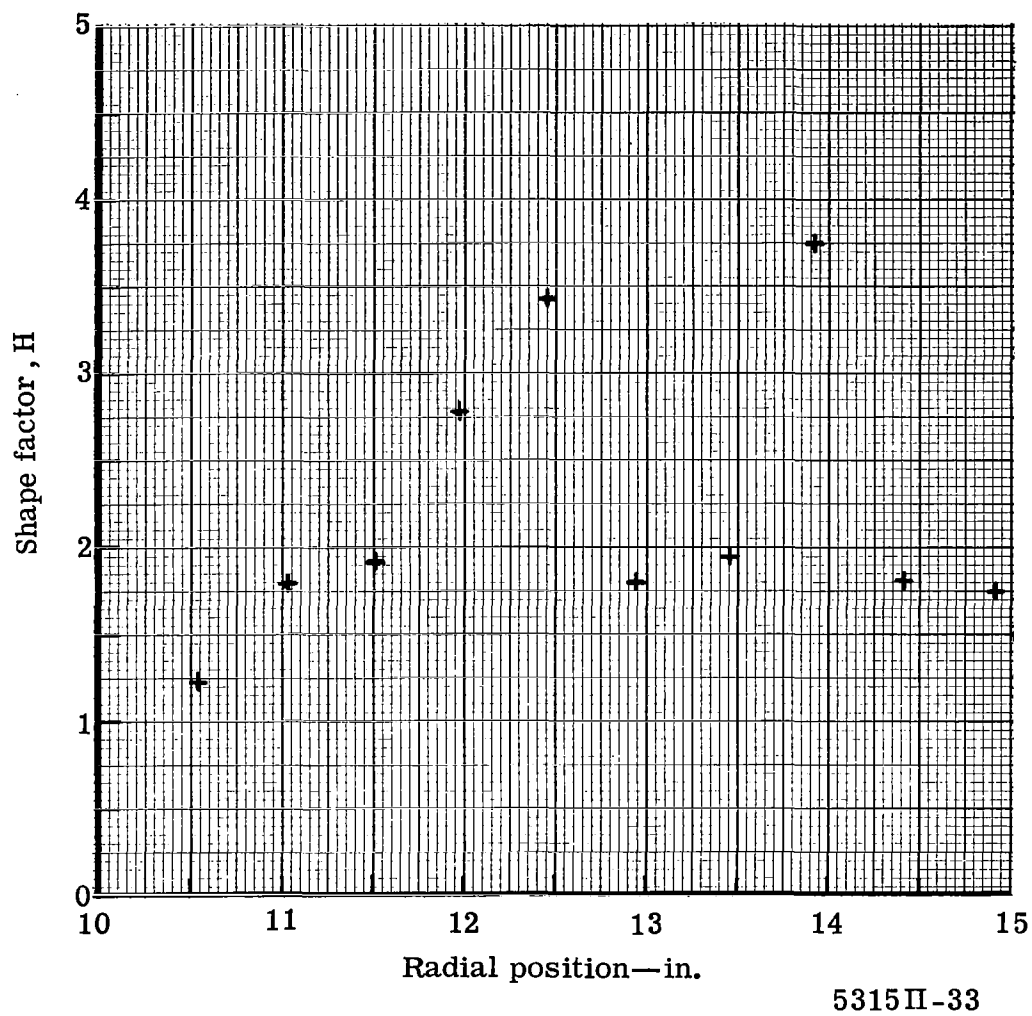
5315II-32

Figure 33. Plain blade exit wake survey—shape factor distribution at station 3.
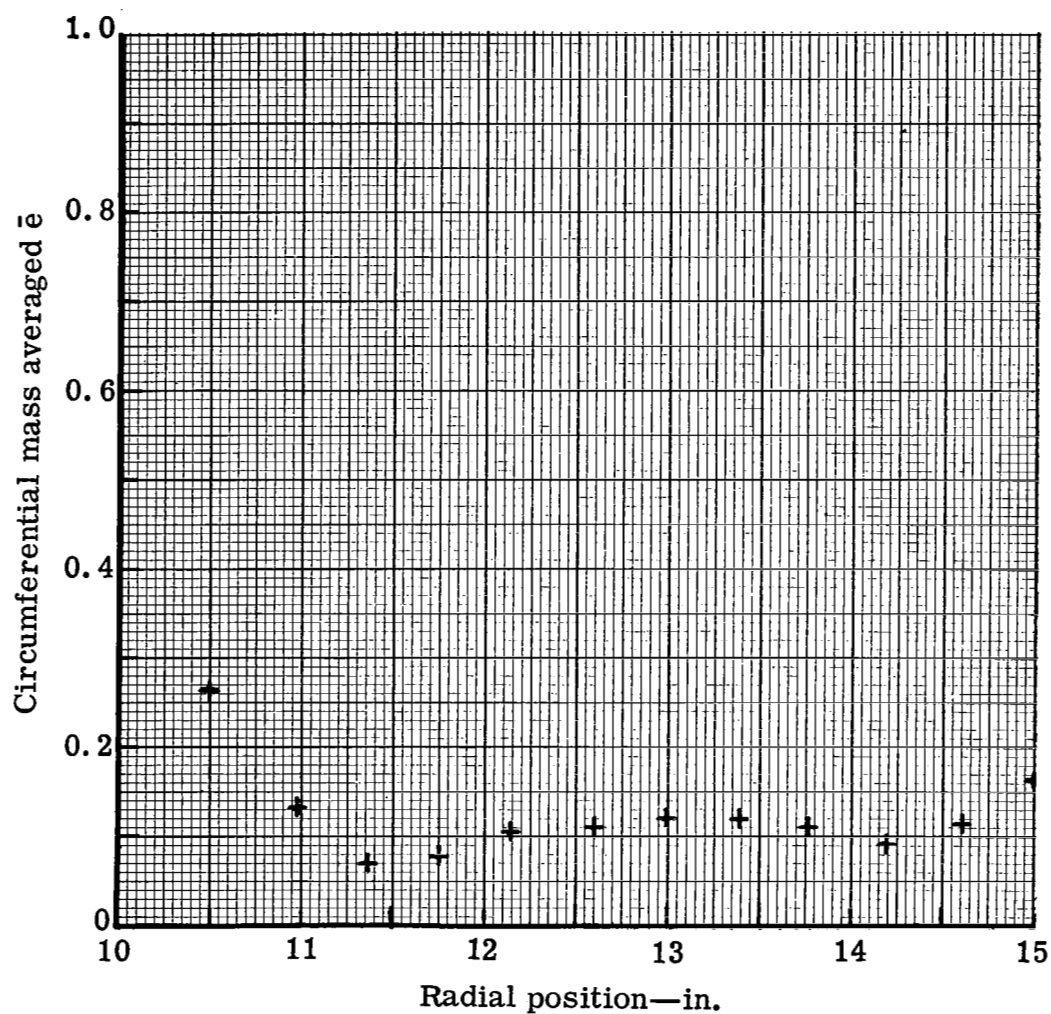
5315 II-33

Figure 34. Plain blade downstream wake survey—kinetic energy loss coefficient distribution at station 4.

5315 II-34
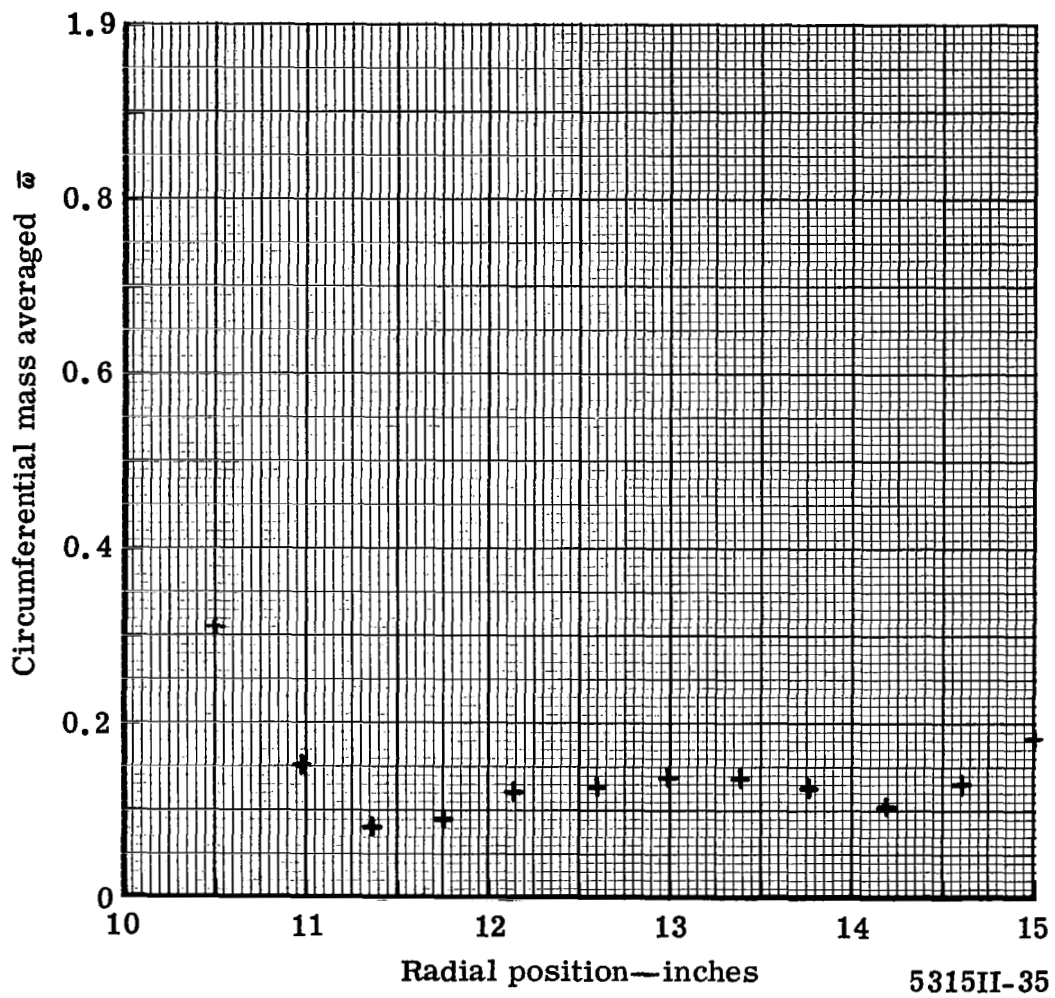
Figure 35. Plain blade downstream wake survey—total pressure loss coefficient distribution at station 4.
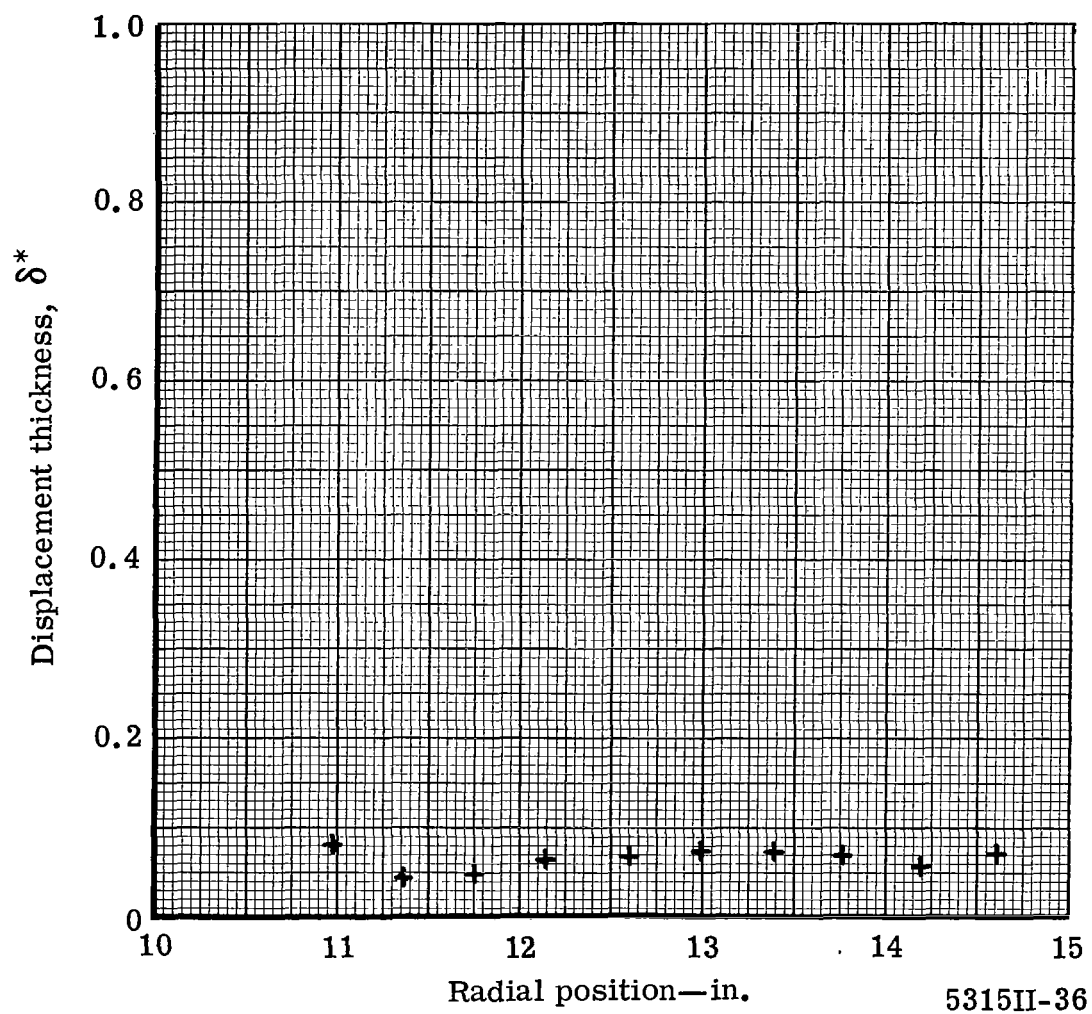
Figure 36. Plain blade downstream wake survey—displacement
thickness distribution at station 4.
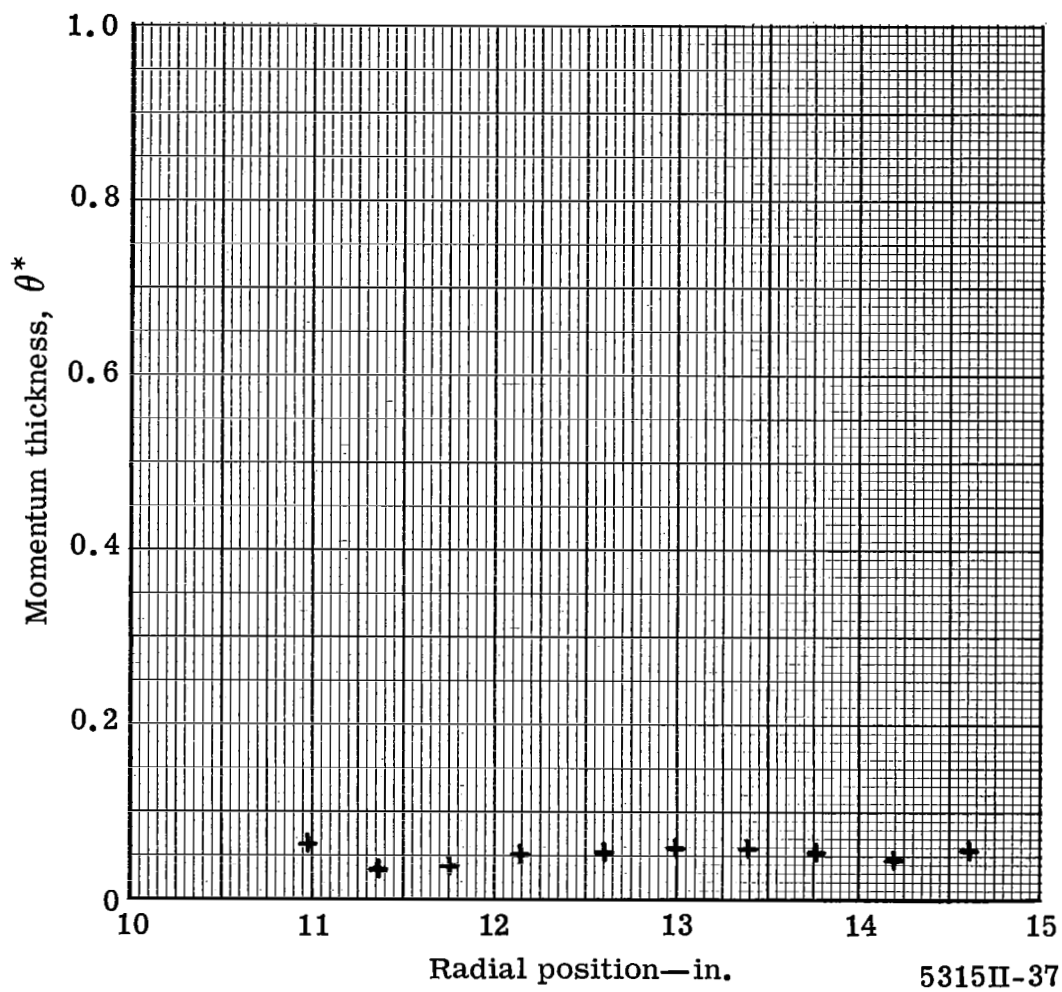
Figure 37. Plain blade downstream wake survey—momentum thickness
distribution at station 4.
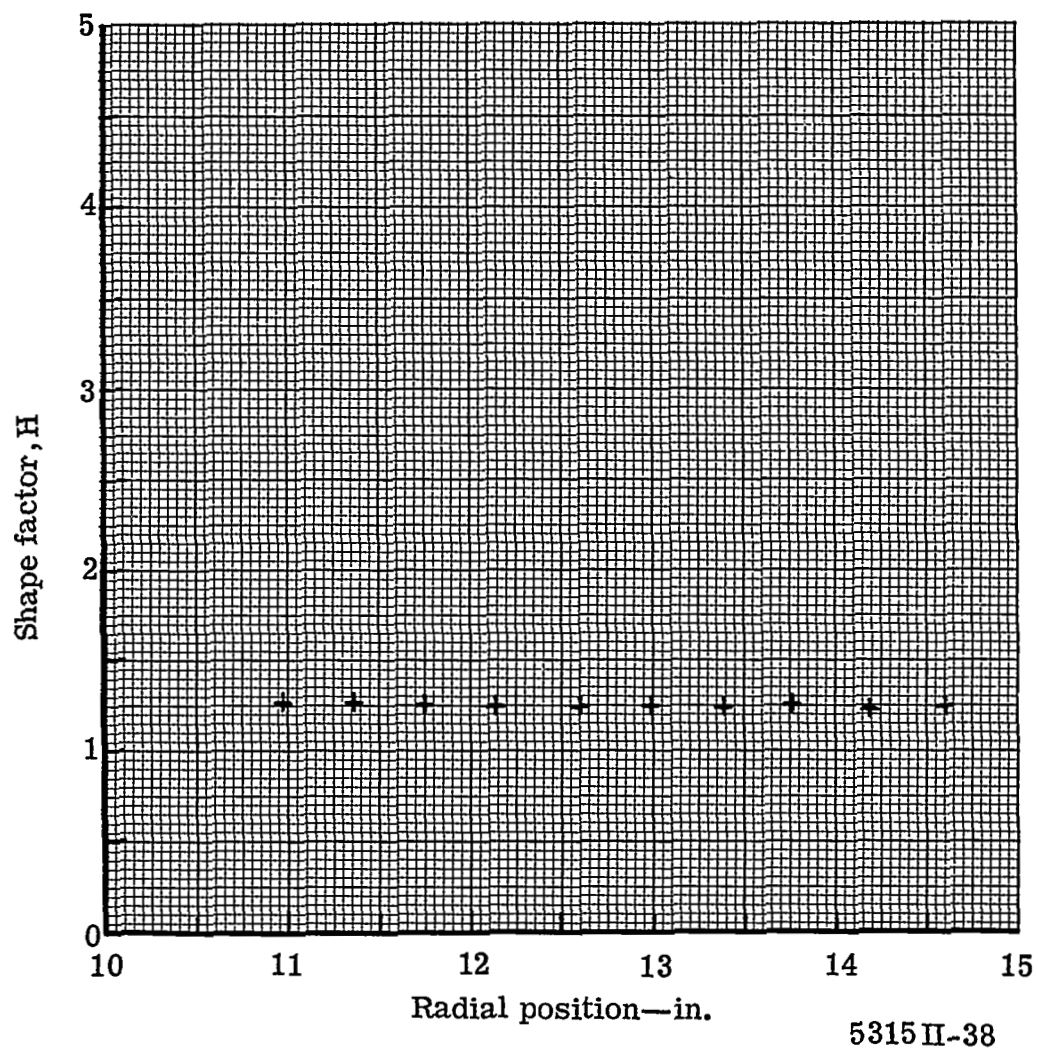
5315 II-38

Figure 38. Plain blade downstream wake survey—shape factor distribution at station 4.

A. Co-rotating vane vortex generator

B. Triangular plow vortex generator
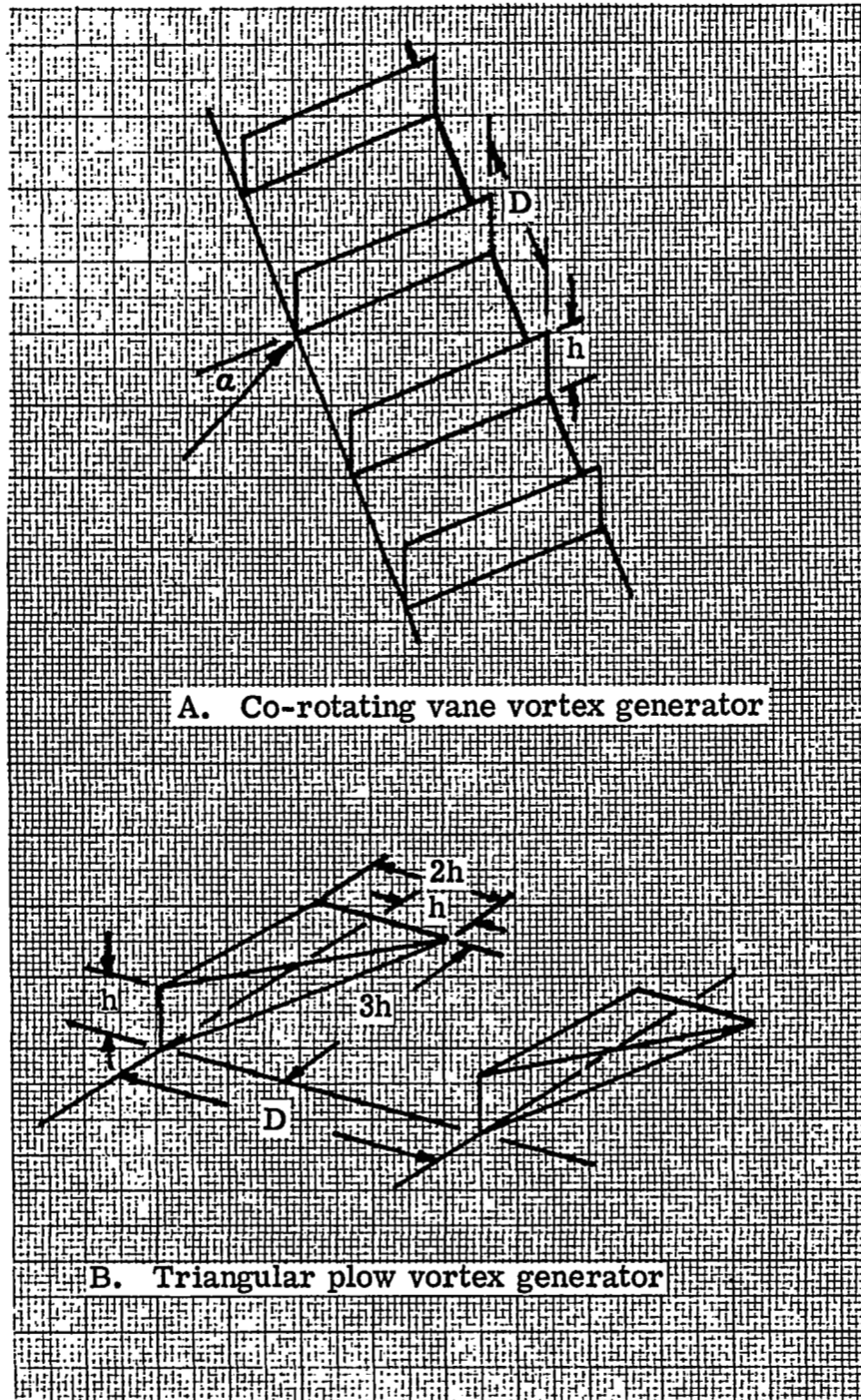
Figure 39. Types of vortex generators mounted on plain
blade configuration.
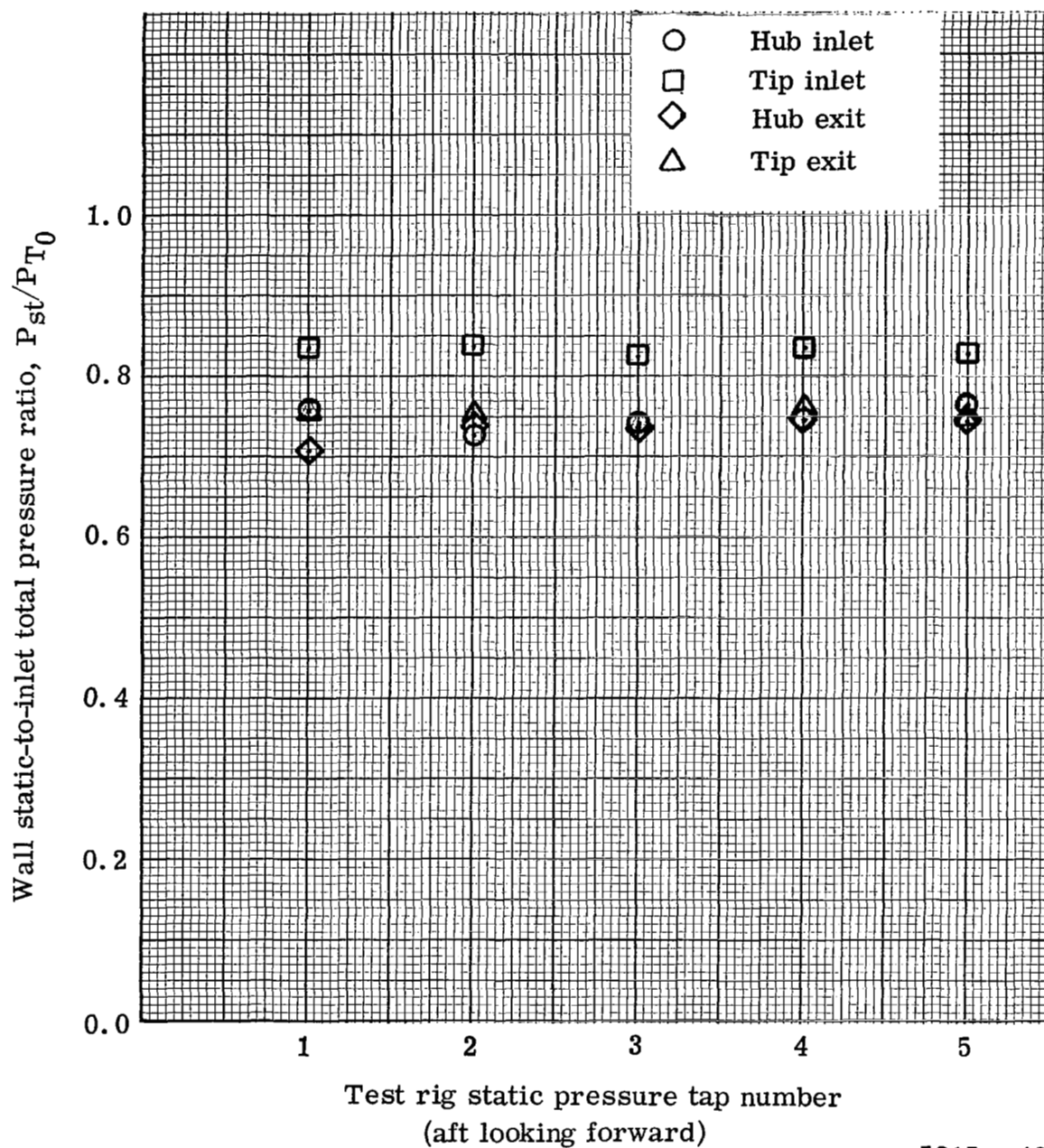
Figure 40. Circumferential variation of static pressure on inlet and exit hub and tip walls for co-rotating vane vortex generator blade.

5315II-40

90
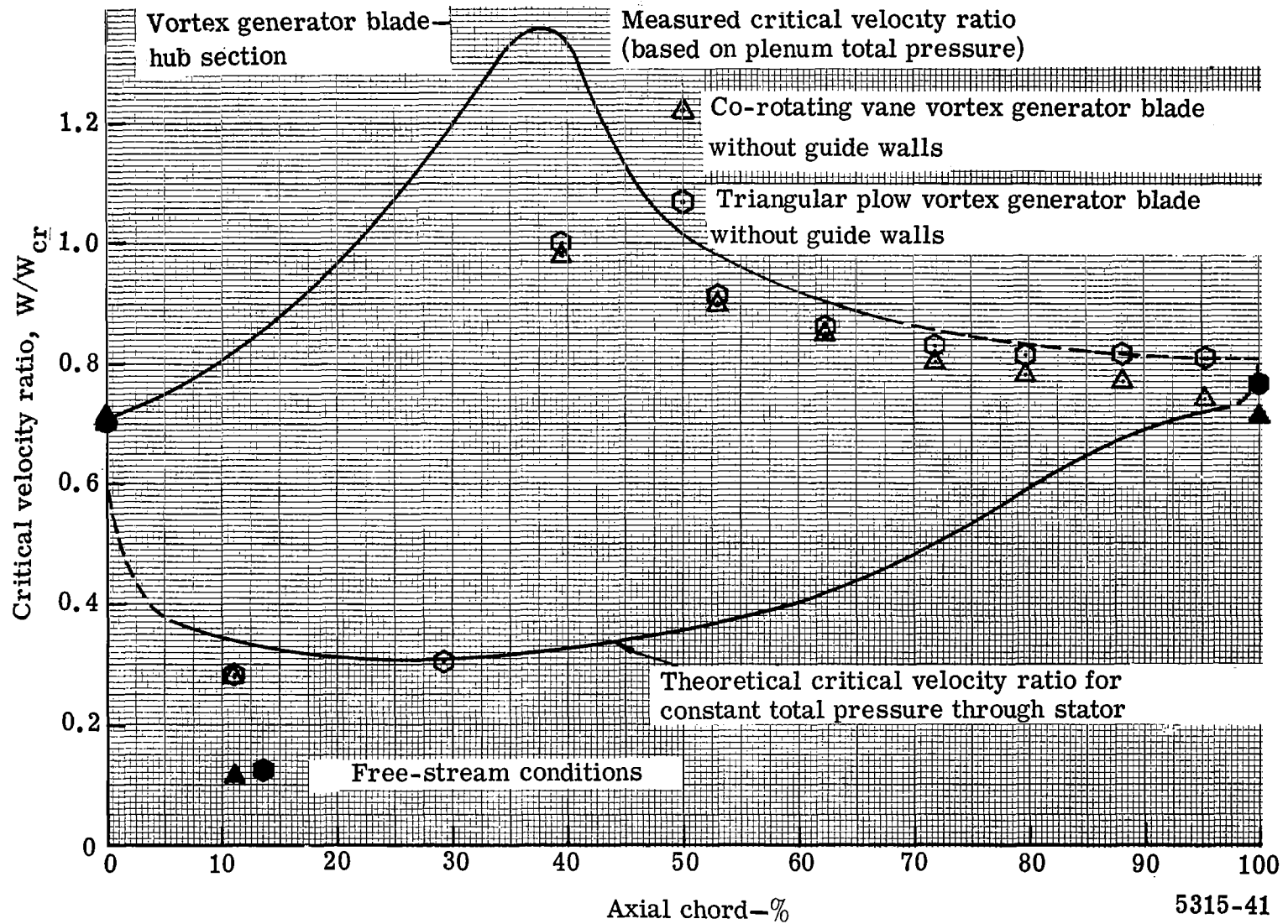
Figure 41.   Measured and predicted surface critical velocity ratio distribution
for vortex generator blade hub section.
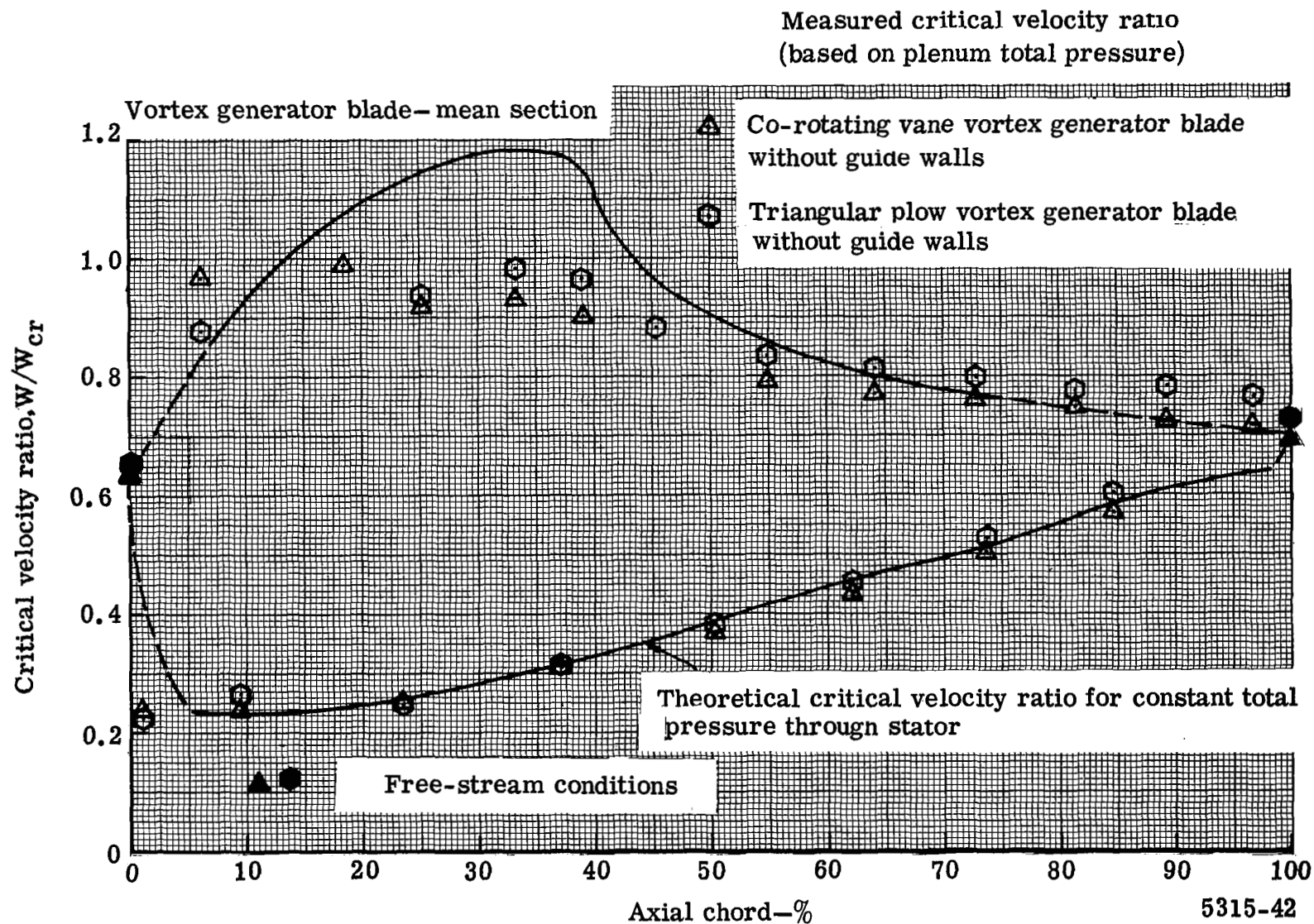
5315-41

Figure 42. Measured and predicted surface critical velocity ratio distribution for vortex generator blade mean section.
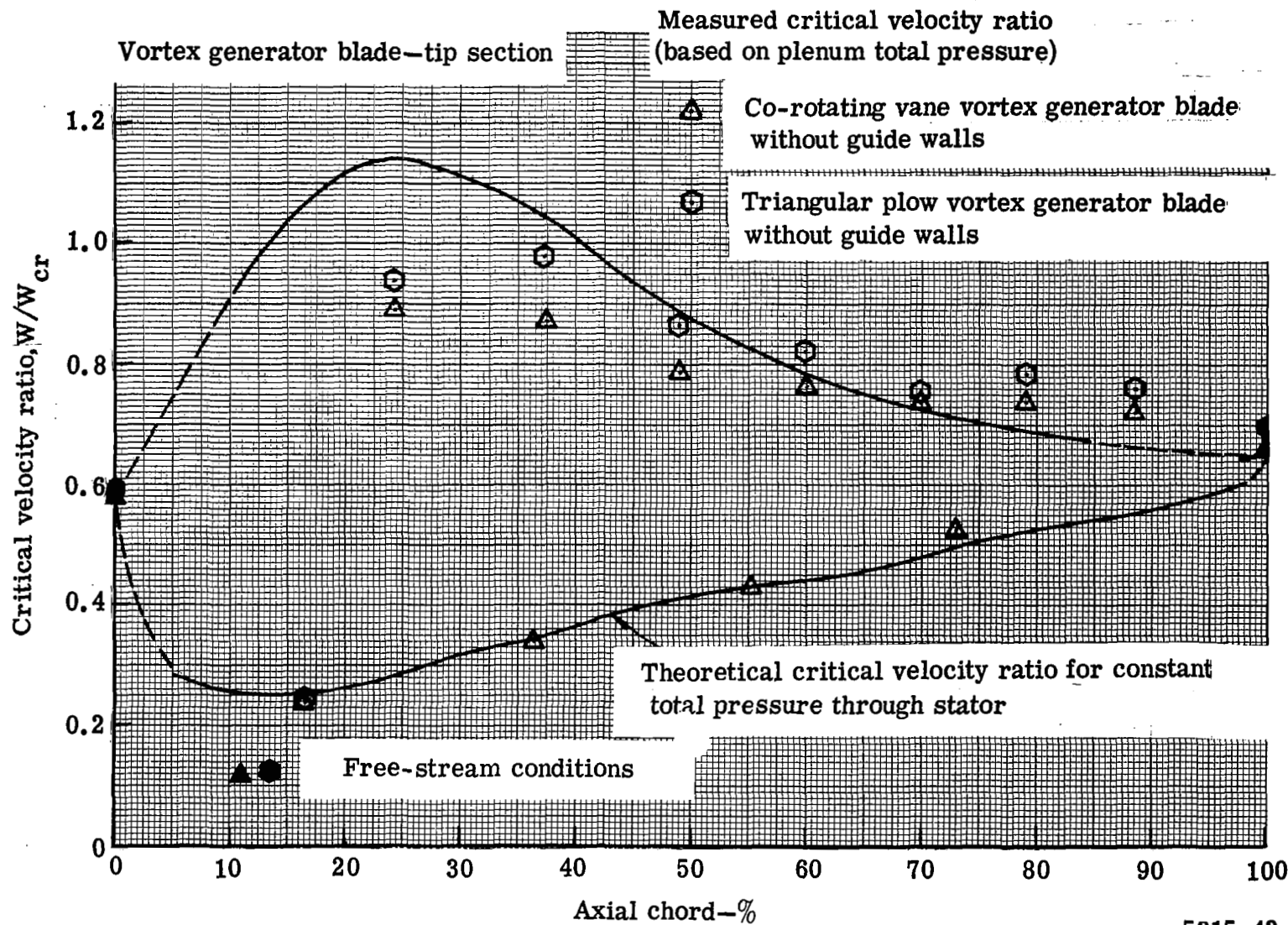
Figure 43. Measured and predicted surface critical velocity ratio distribution for vortex generator blade tip section.

5315-43
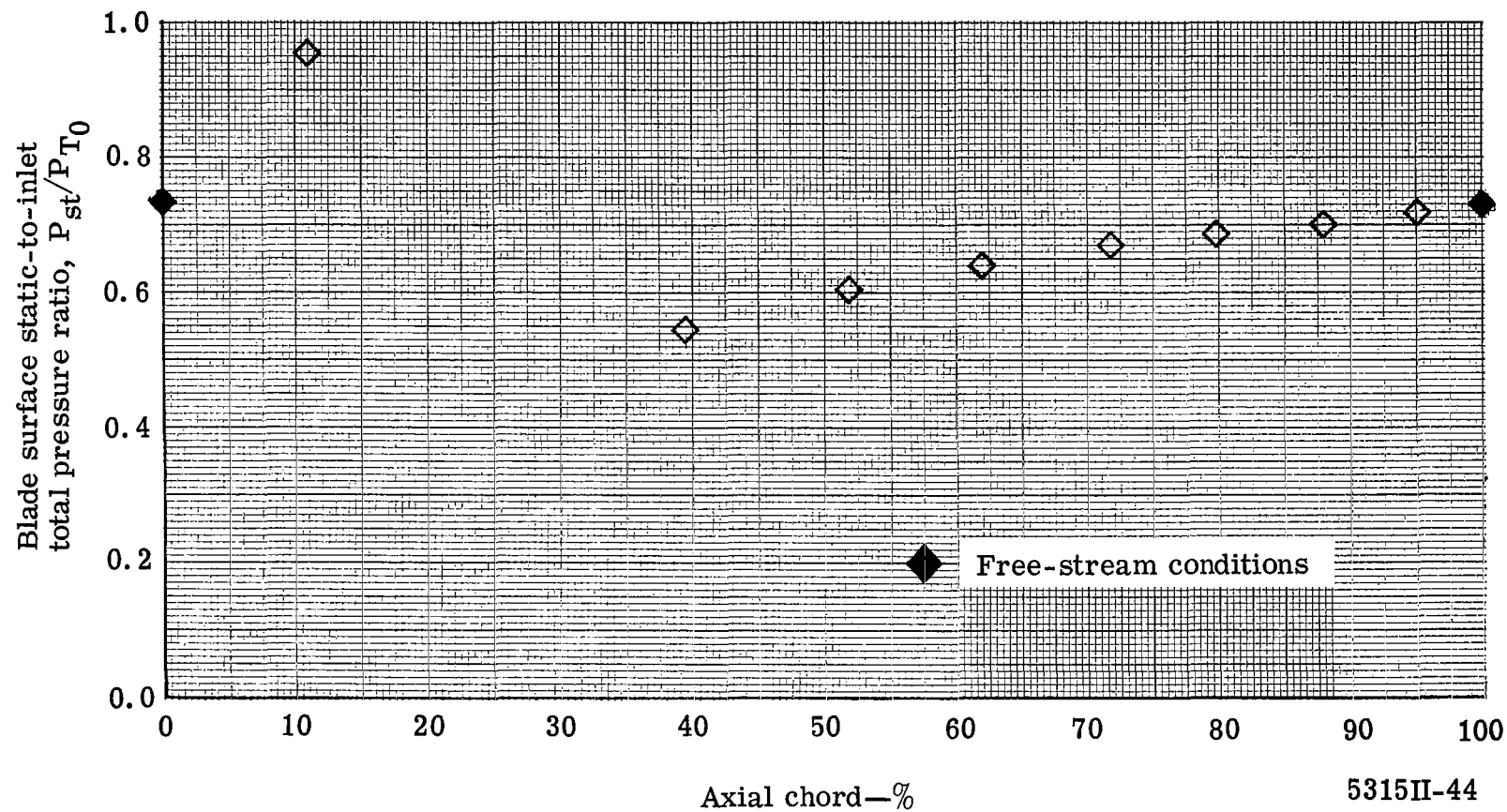
Figure 44.   Measured surface static pressure distribution for the co-rotating vane
vortex generator blade—hub section.

5315II-44
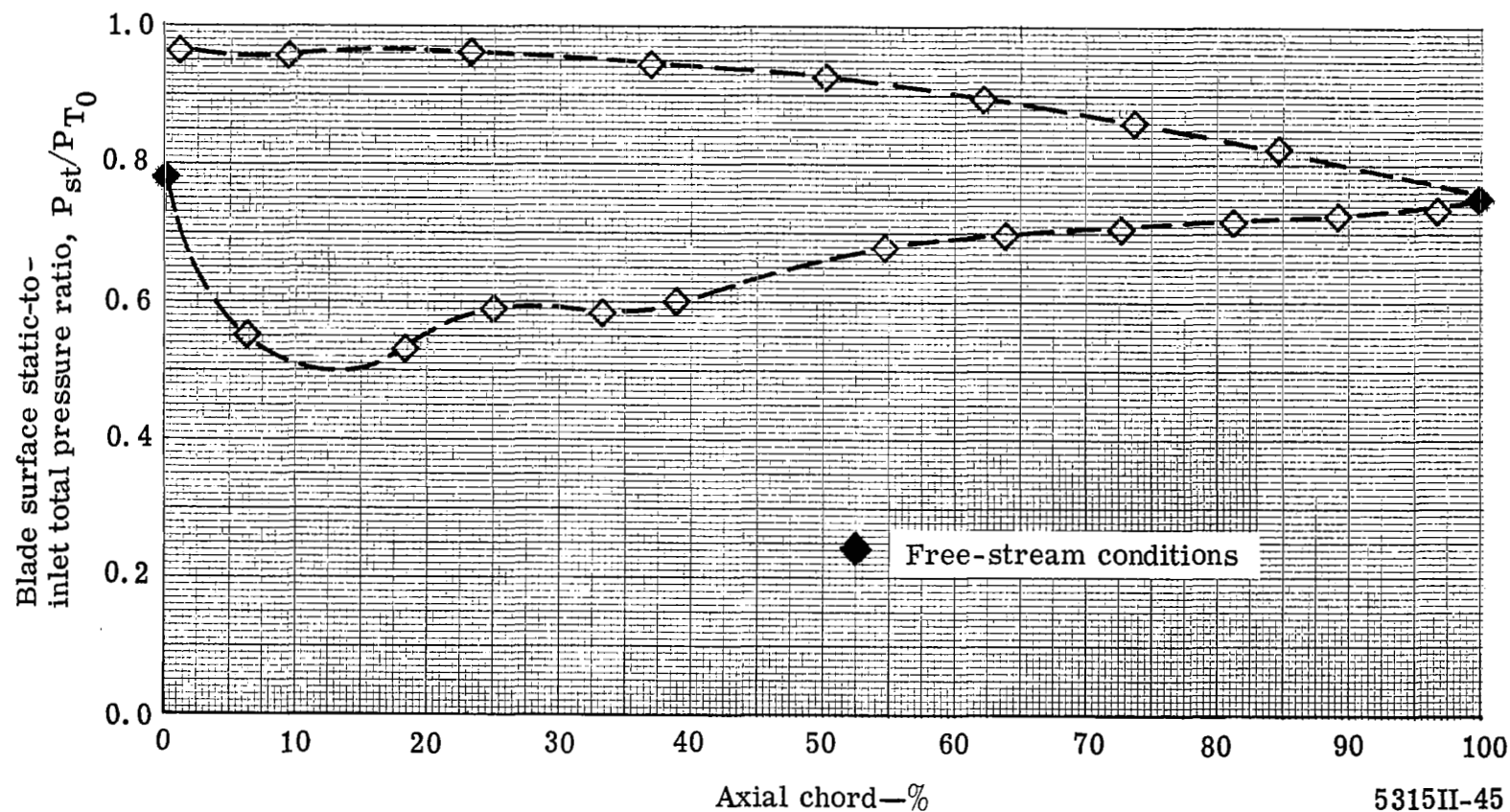
Figure 45. Measured surface static pressure distribution for the co-rotating vane vortex generator blade—mean section.
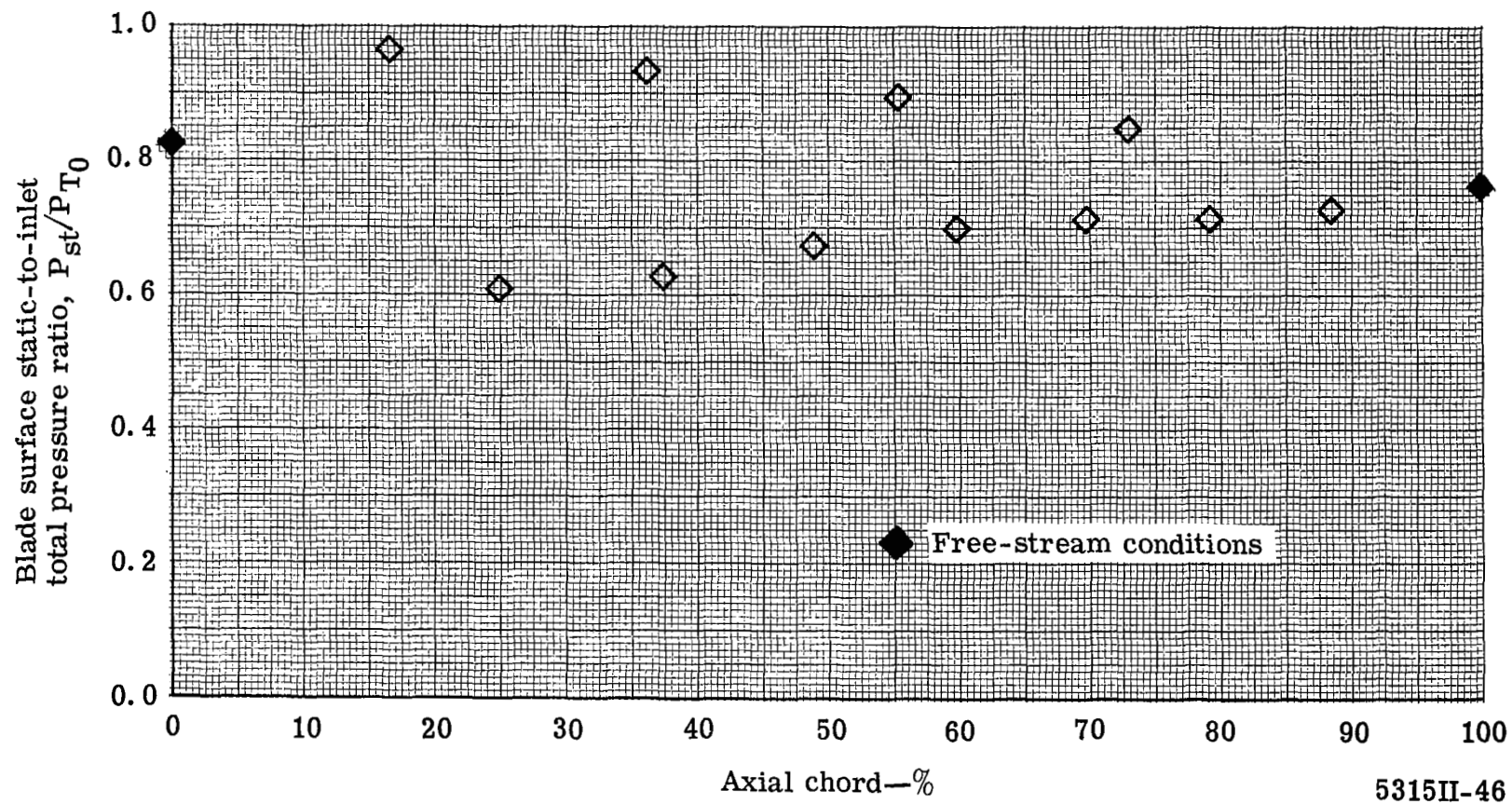
Figure 46. Measured surface static pressure distribution for the co-rotating vane vortex generator blade—tip section.

5315II-46

Vane No. 2

Vane No. 3

Vane No. 4

Vane No. 5

Figure 47. Co-rotating vane vortex generator blade flow visualization results for inlet hub static-to-total pressure ratio of 0.65 (below design value).

Vane No. 2

Vane No. 3

Vane No. 4

Vane No. 5

Figure 48.   Co-rotating vane vortex generator blade flow visualization results for
inlet hub static-to-total pressure ratio of 0.74 (design value).

Vane No. 2
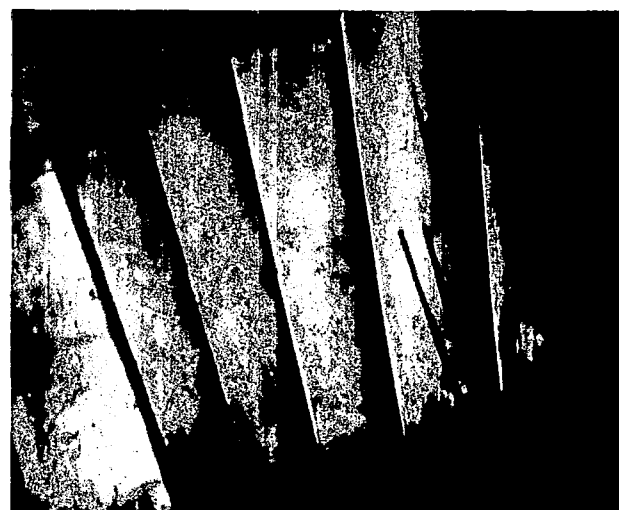
Vane No. 3

Vane No. 4

Vane No. 5

Figure 49. Co-rotating vane vortex generator blade flow visualization results for inlet hub static-to-total pressure ratio of 0.82 (above design value).
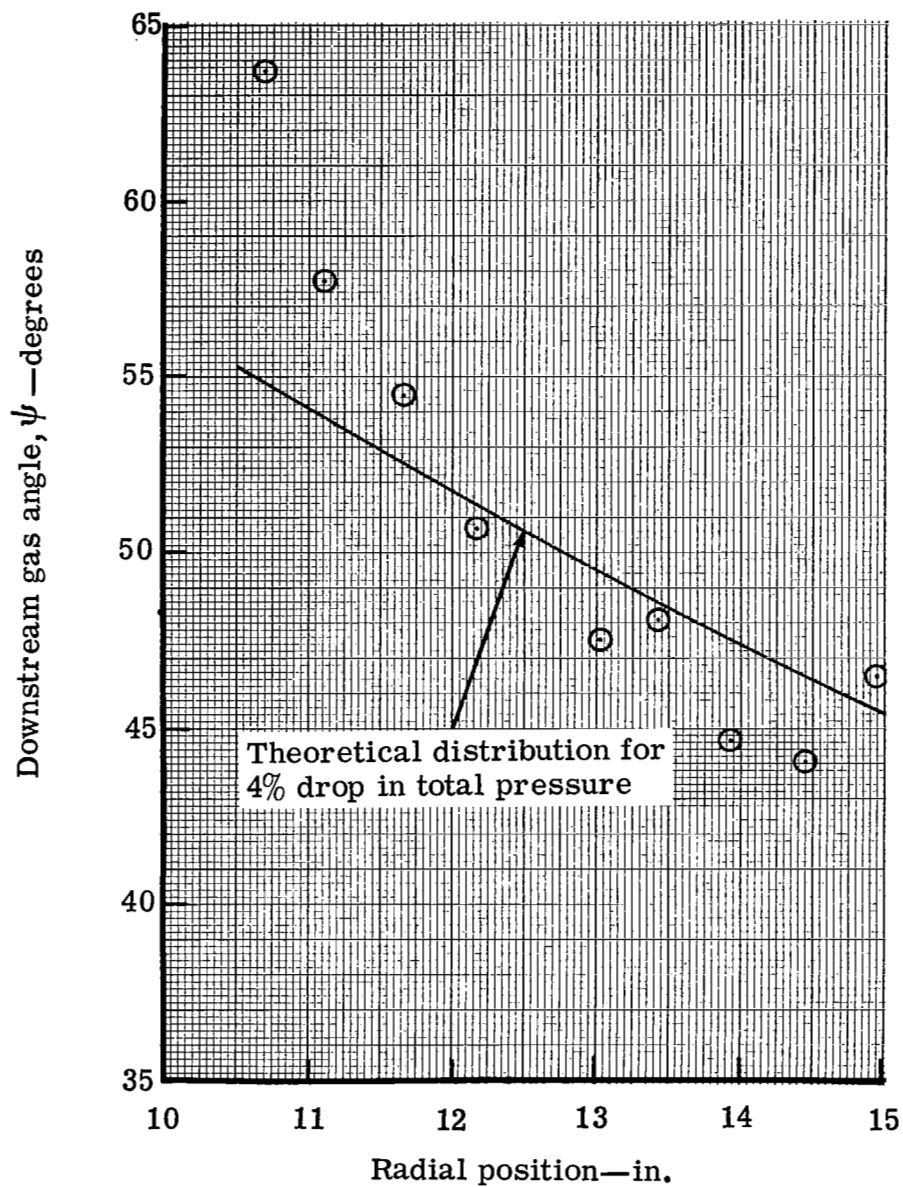
Figure 50. Measured and predicted radial variation of average downstream gas angle for co-rotating vane vortex generator blade.
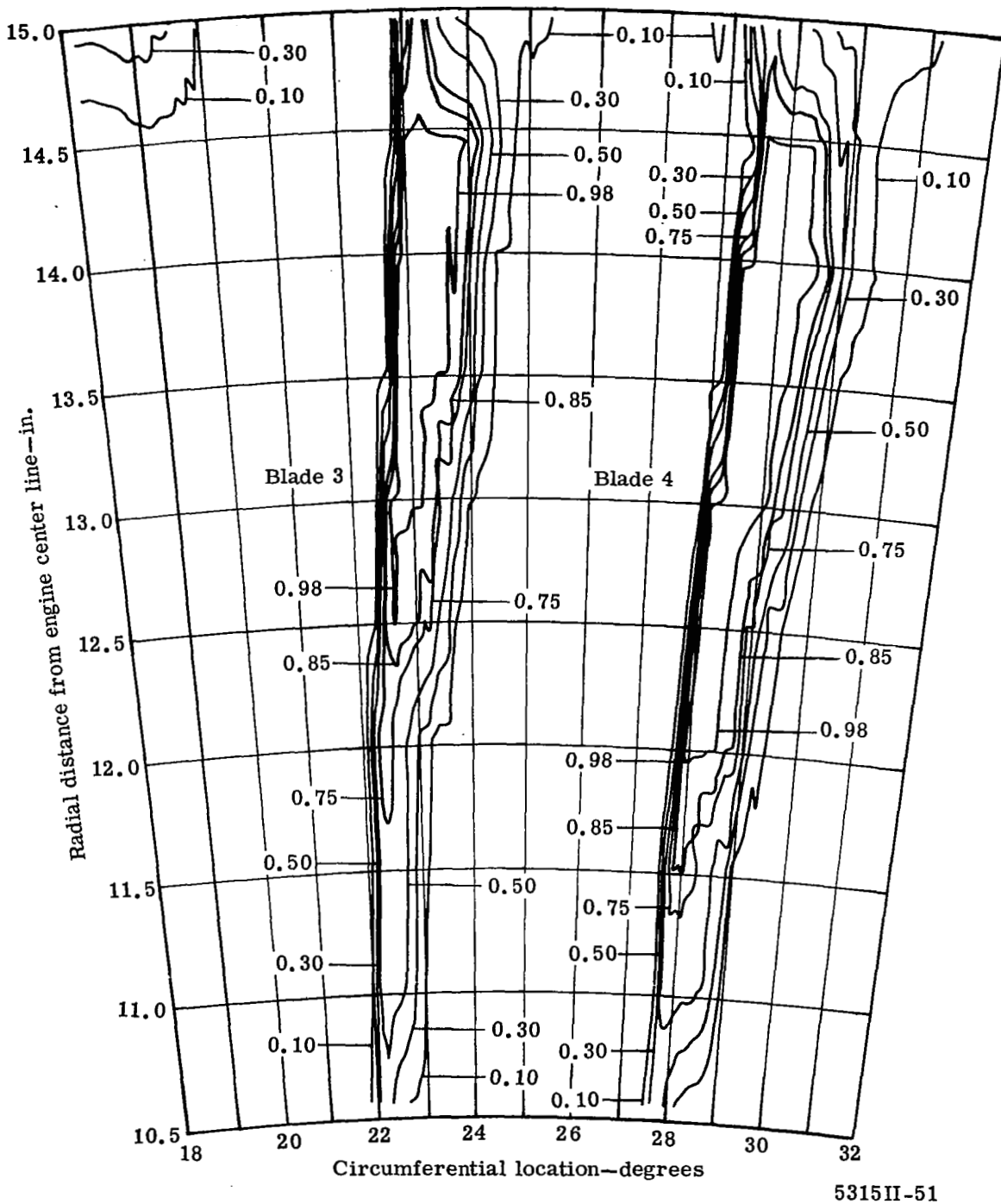
Figure 51. Contours of kinetic energy loss coefficient across one blade
passage—co-rotating vane vortex generator blade exit
wake survey.

5315 II-51

101
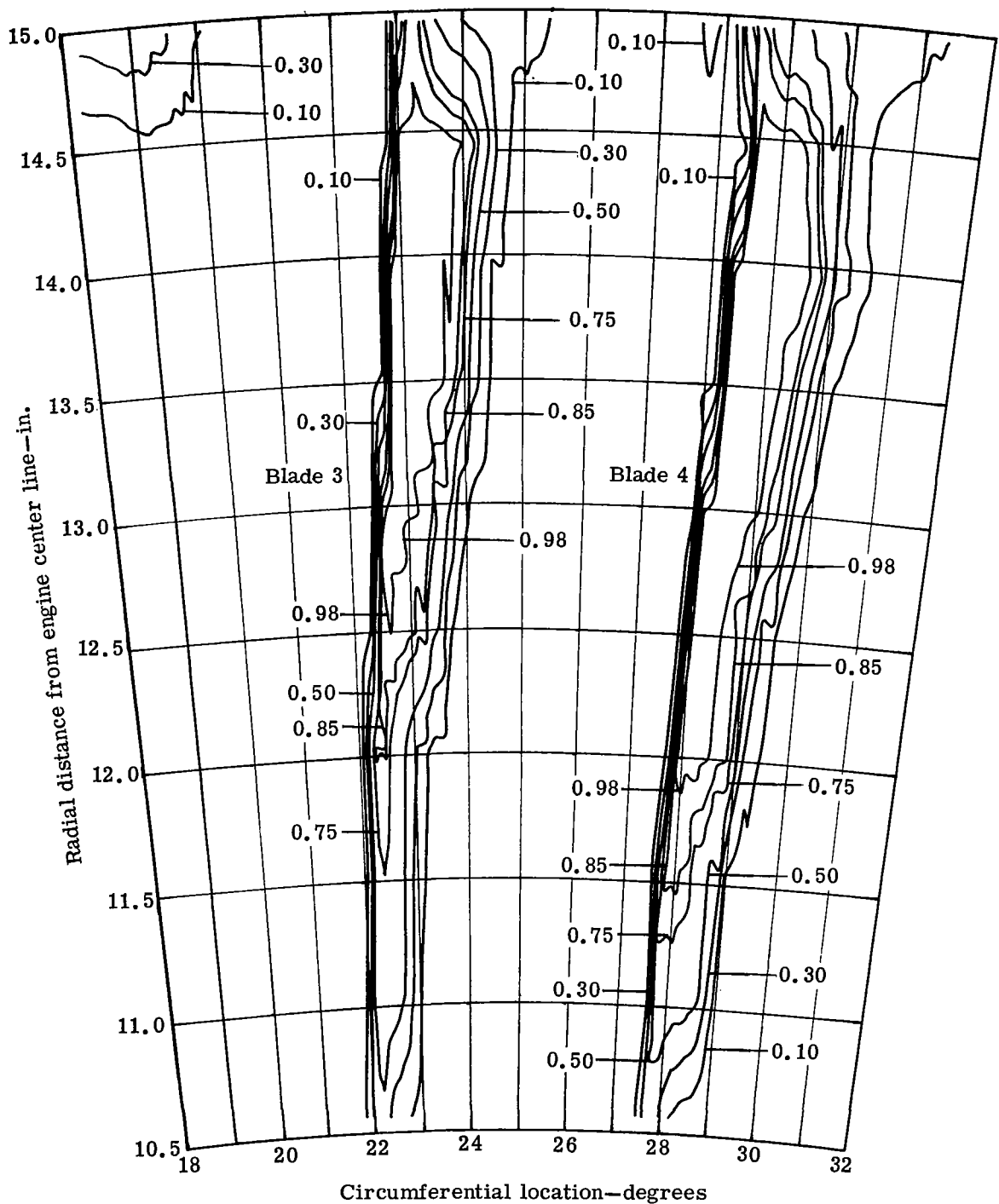
Figure 52. Contours of total pressure loss coefficient across one blade passage—co-rotating vane vortex generator blade exit wake survey.
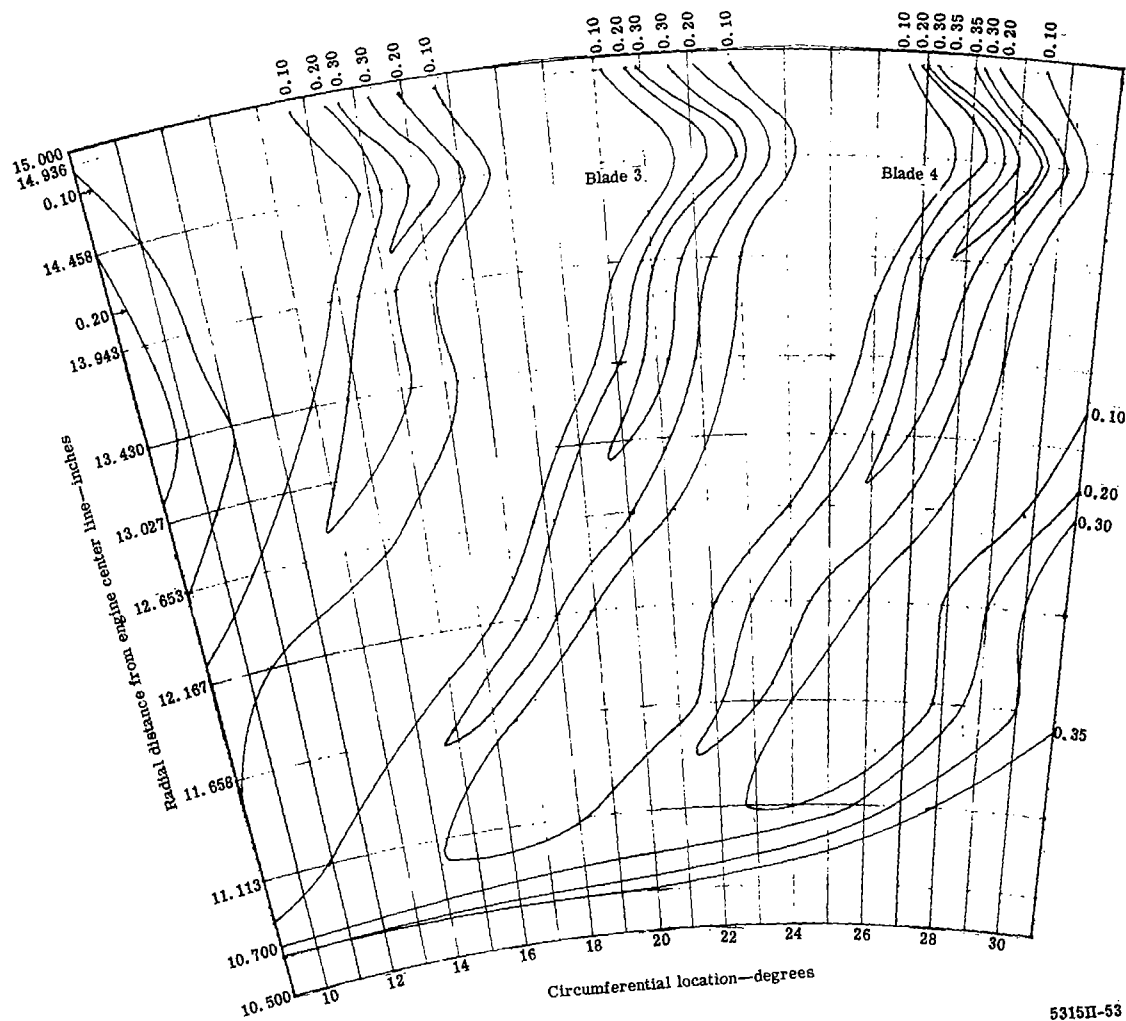
Figure 53. Contours of kinetic energy loss coefficient—co-rotating vane vortex generator downstream wake survey.
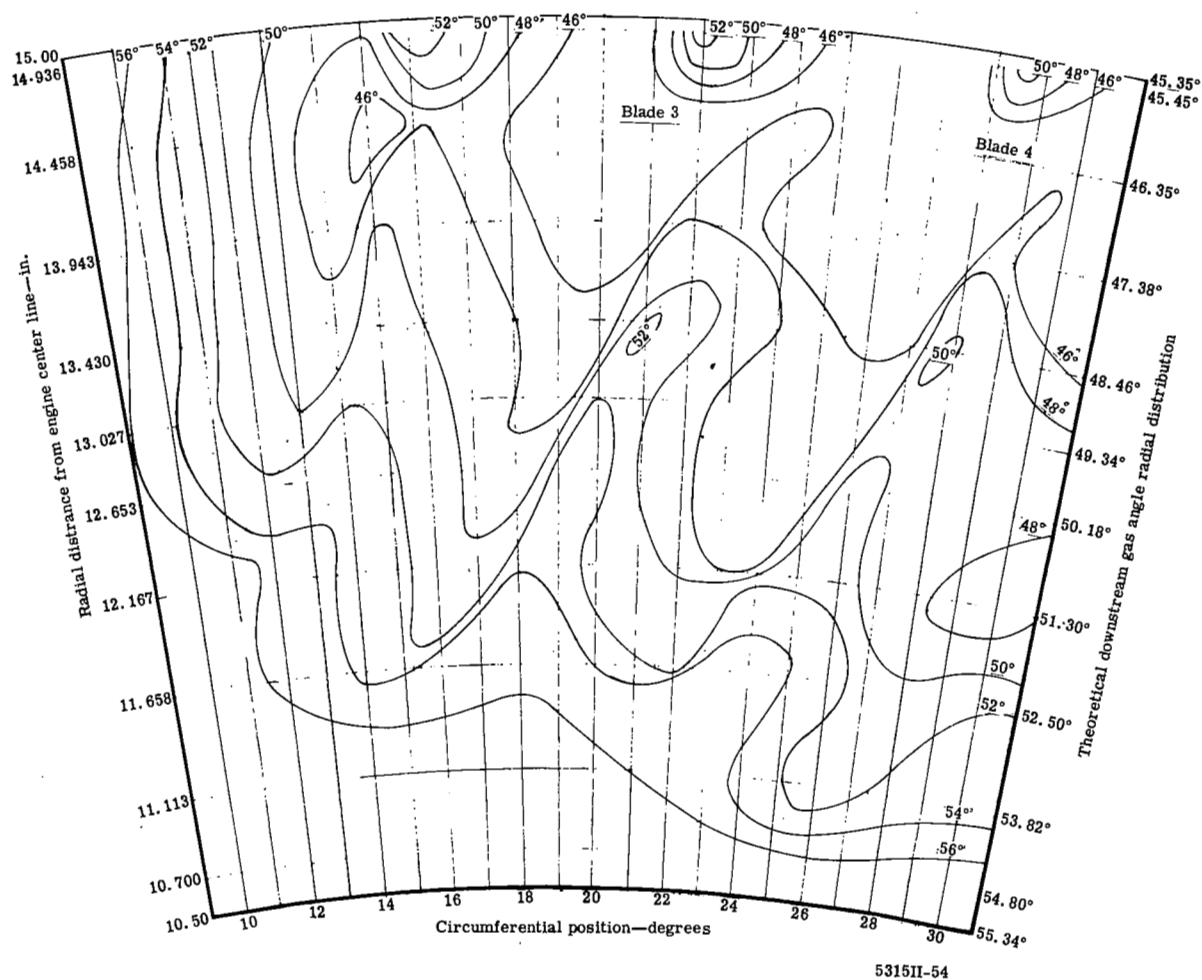
5315II-53

Figure 54. Contours of downstream gas angle—measured from axial-co-rotating vane vortex generator downstream wake survey.
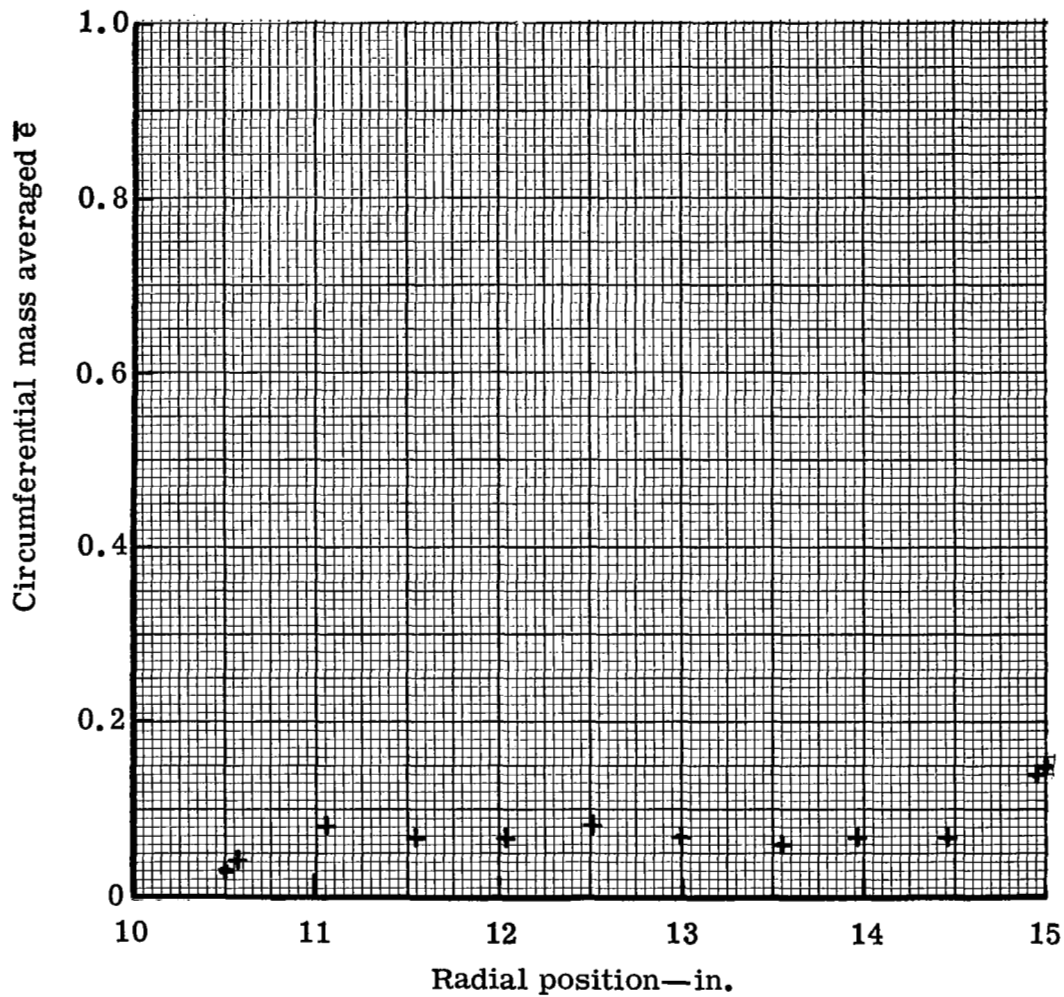
Figure 55. Co-rotating vane vortex generator exit wake survey—kinetic energy loss coefficient distribution at station 3.
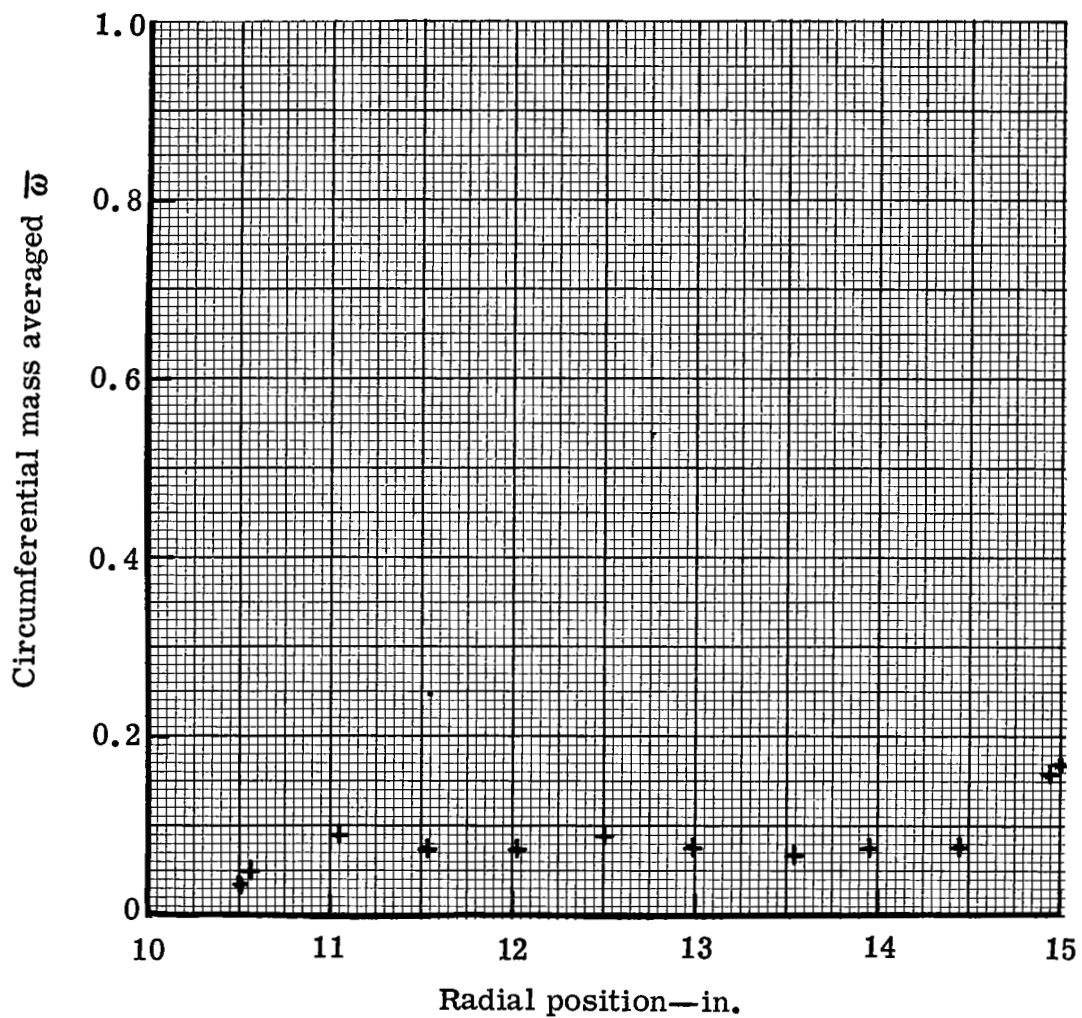
5315II-55

Figure 56.   Co-rotating vane vortex generator exit wake survey—total pressure loss coefficient distribution at station 3.
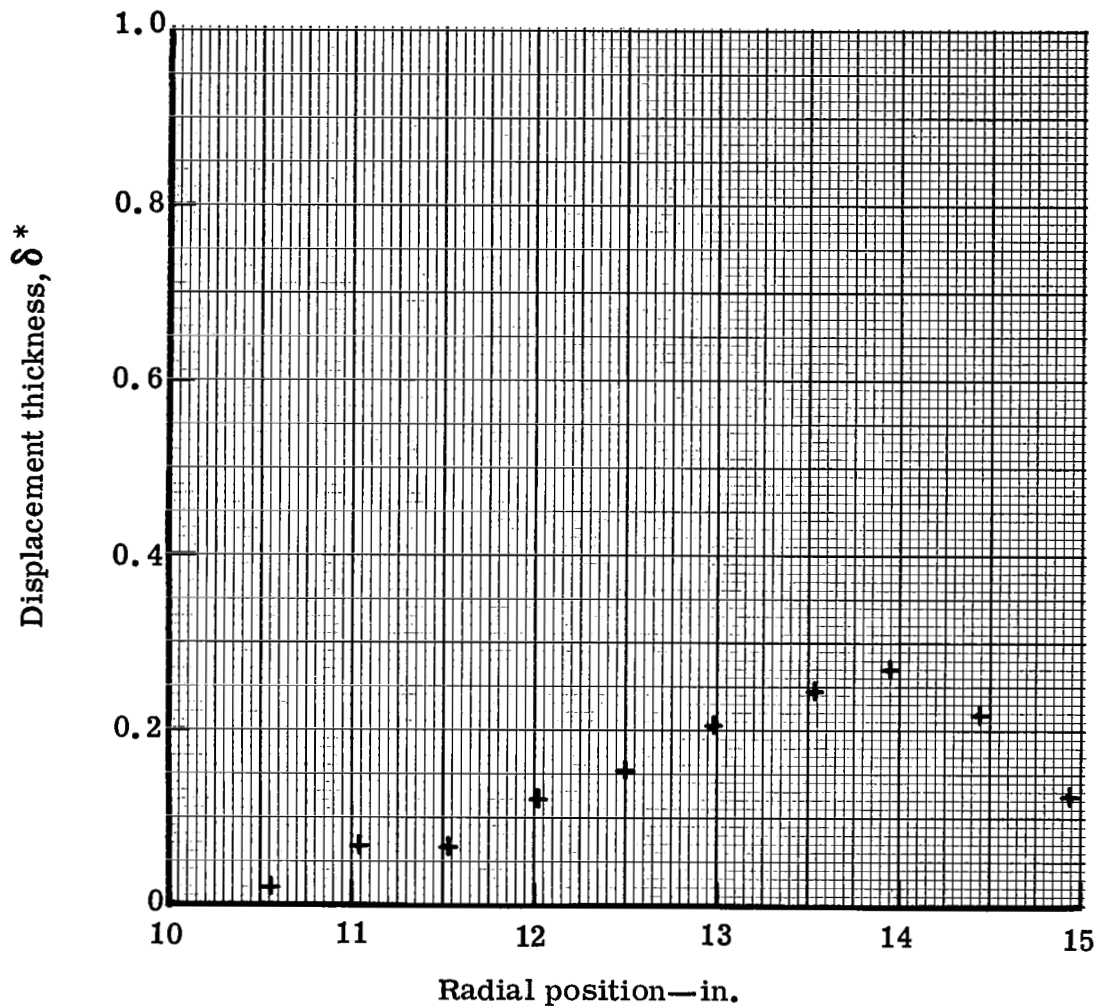
5315II-56

5315II-57

Figure 57. Co-rotating vane vortex generator exit wake survey—
displacement thickness distribution at station 3.
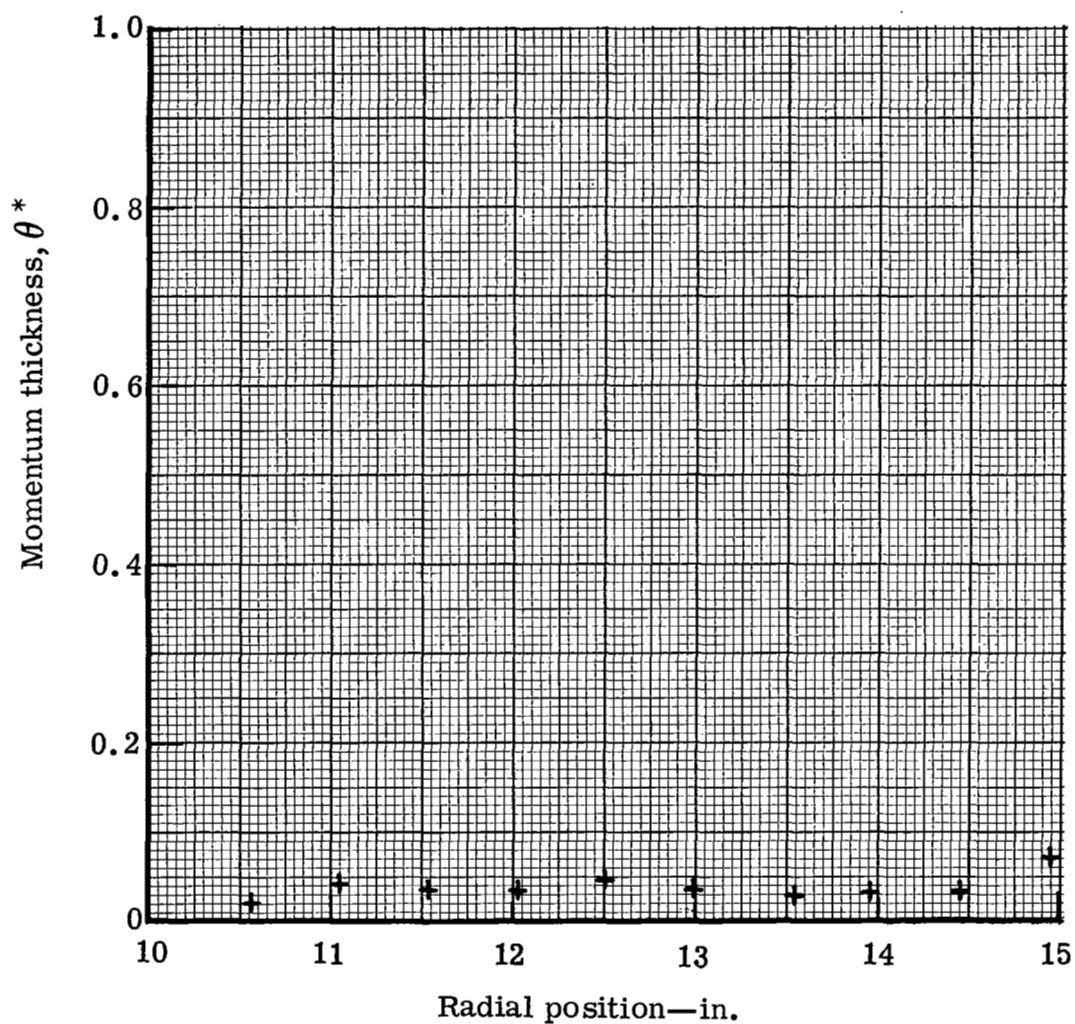
Figure 58. Co-rotating vane vortex generator exit wake survey—momentum thickness distribution at station 3.
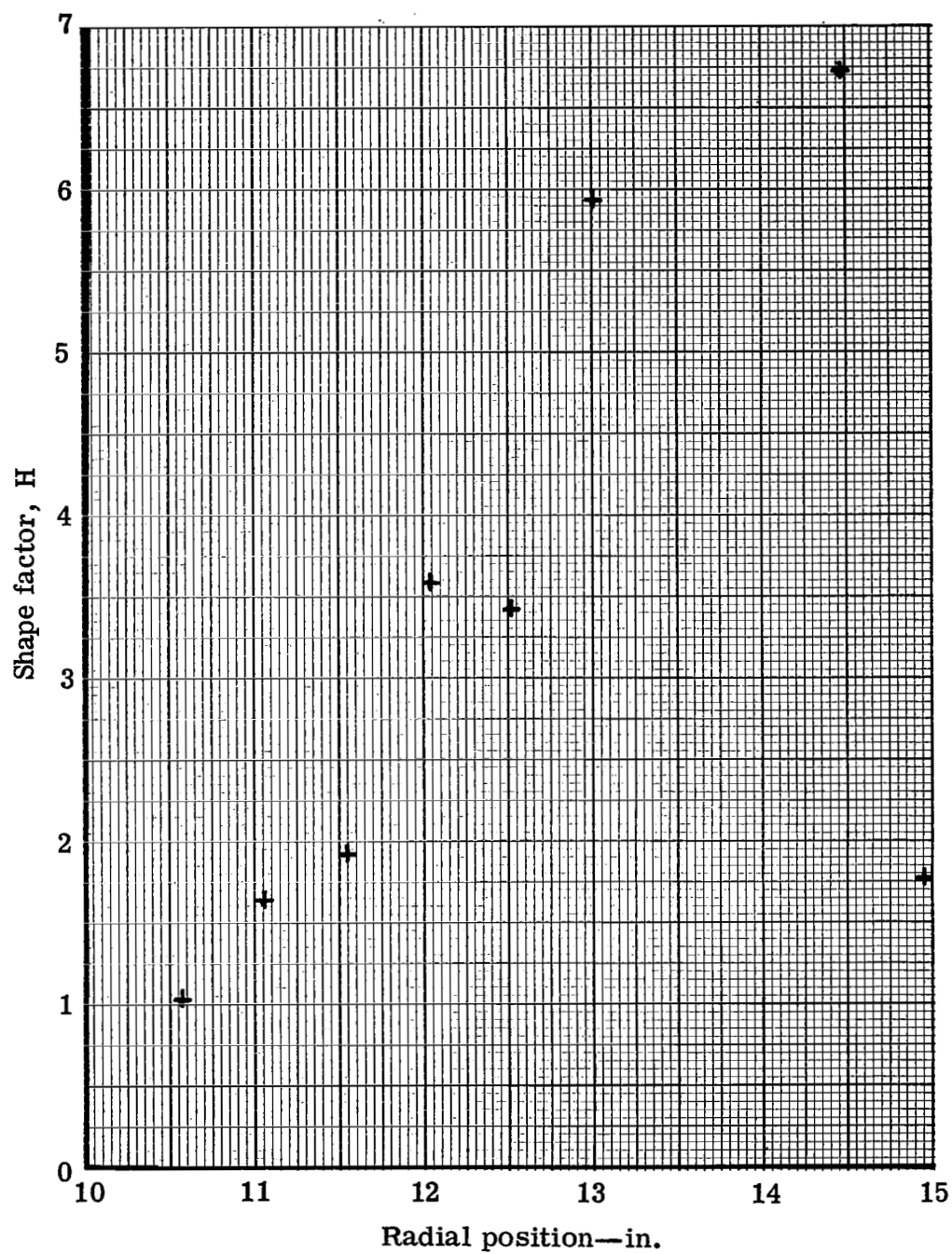
Figure 59. Co-rotating vane vortex generator exit wake survey—shape factor distribution at station 3.
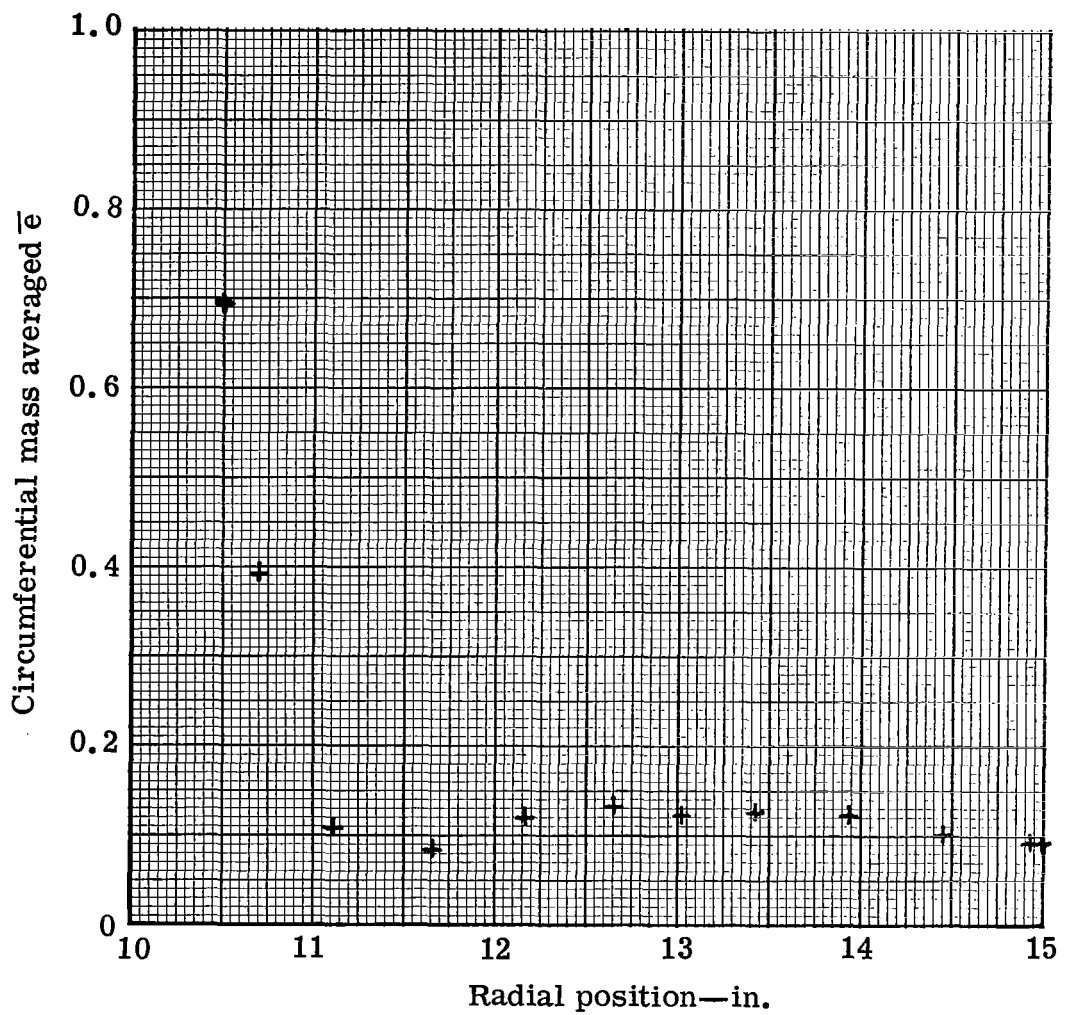
5315II-59

Figure 60.   Co-rotating vane vortex generator downstream wake
survey—kinetic energy loss coefficient distribution
at station 4.
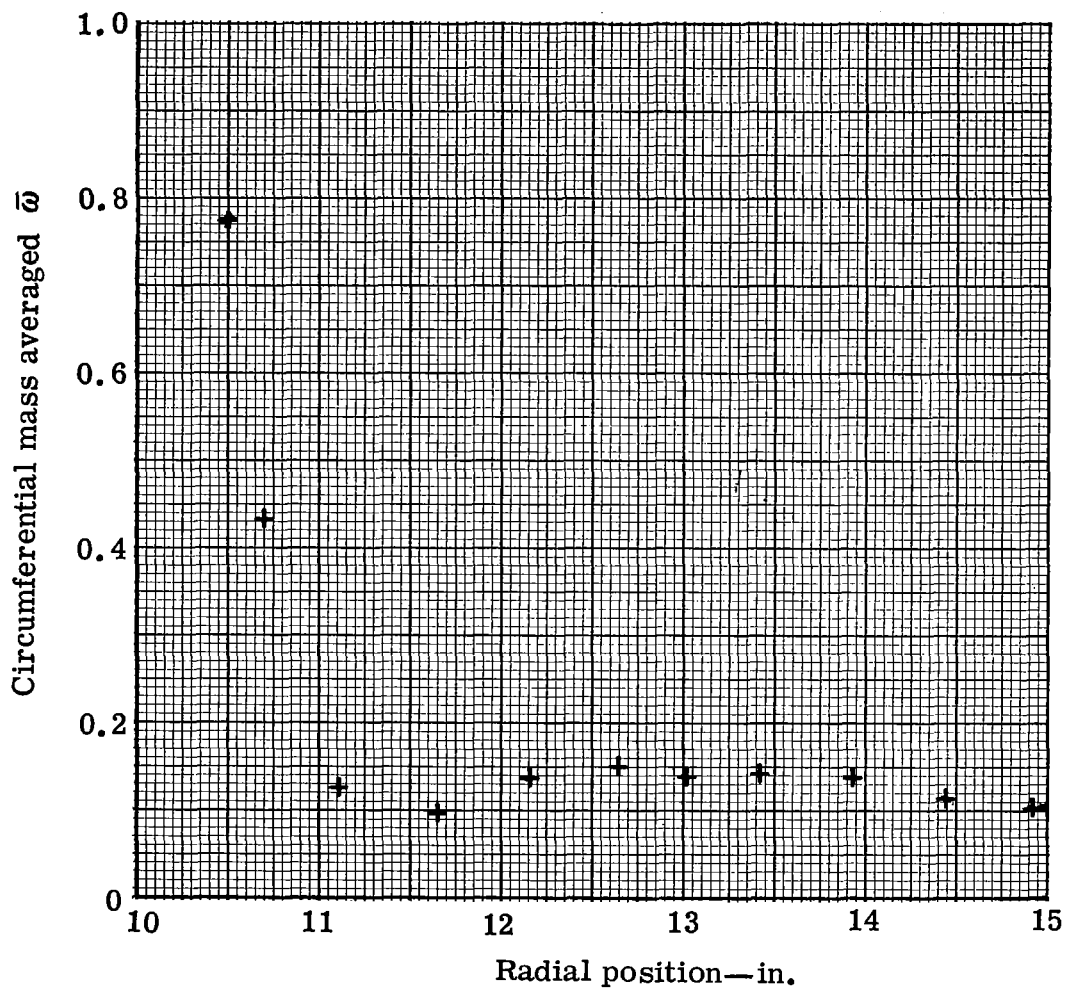
Figure 61. Co-rotating vane vortex generator downstream wake
survey—total pressure loss coefficient distribution
at station 4.
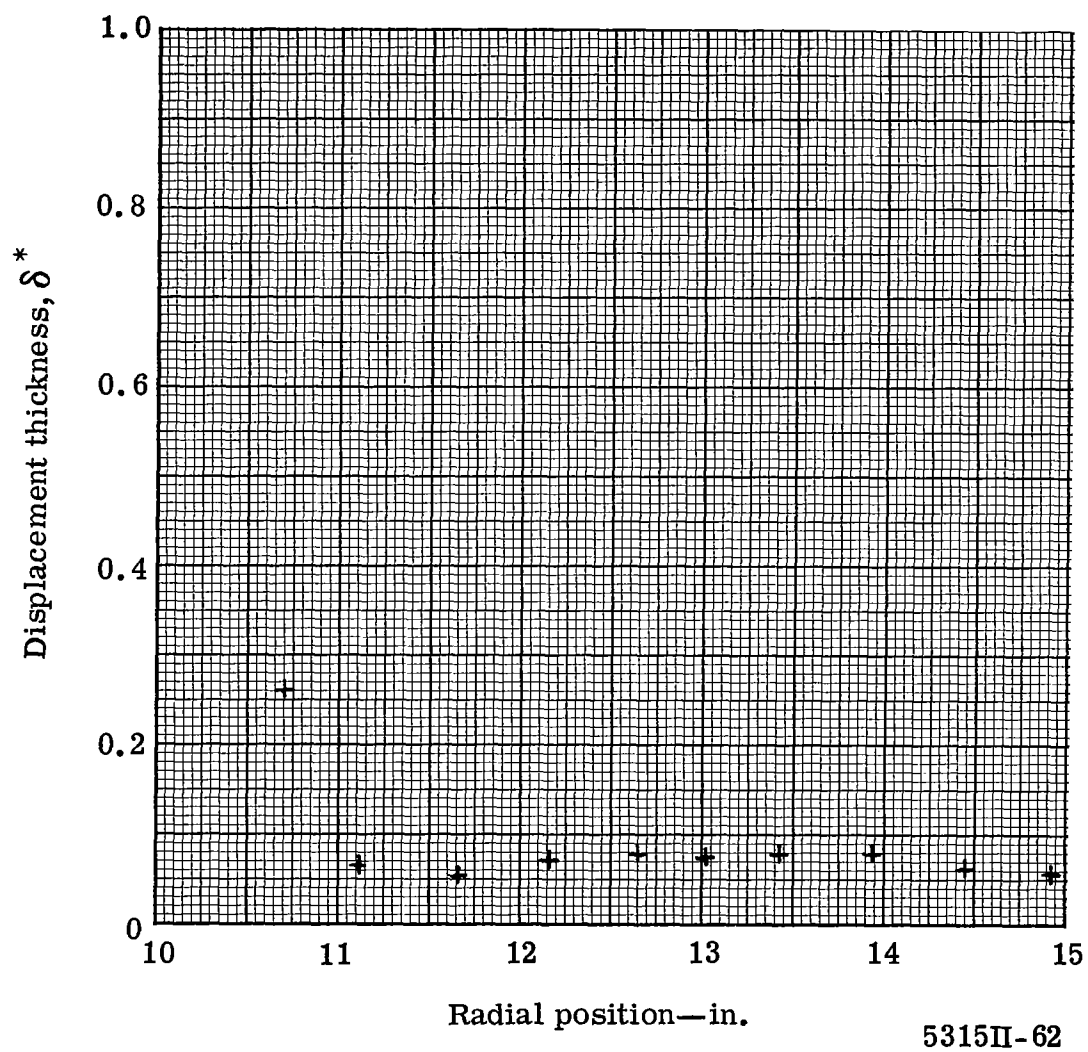
Figure 62. Co-rotating vane vortex generator downstream wake
survey—displacement thickness distribution at station 4.
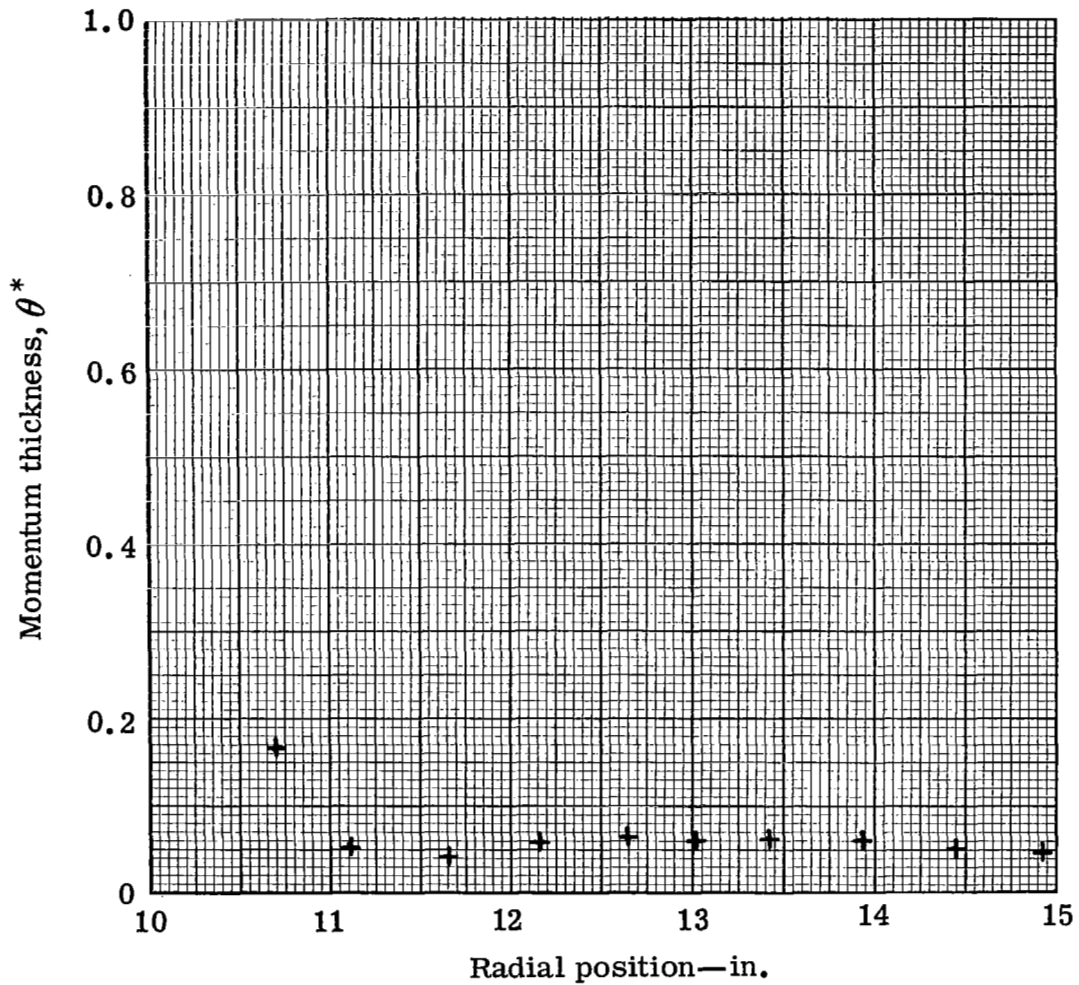
Figure 63. Co-rotating vane vortex generator downstream wake
survey—momentum thickness distribution at station 4.
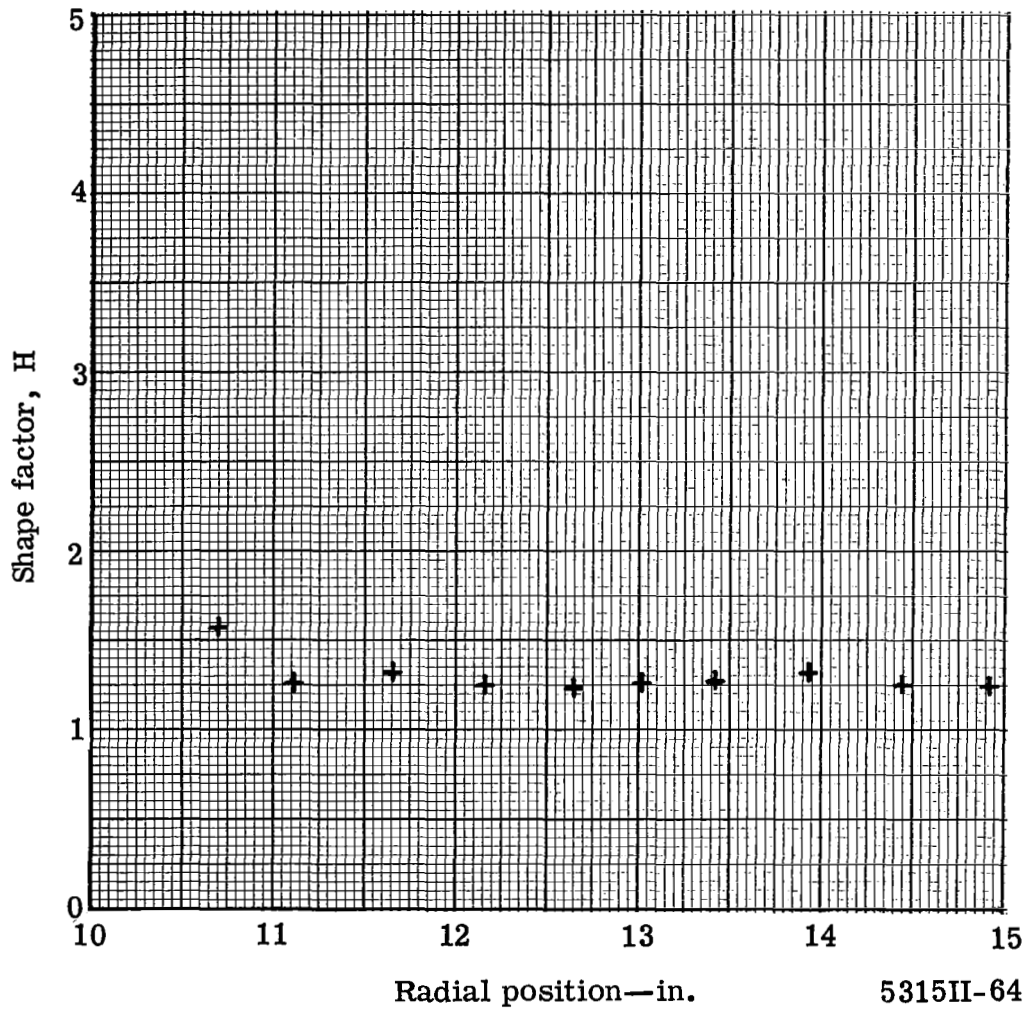
Figure 64. Co-rotating vane vortex generator downstream wake survey—shape factor distribution at station 4.

Triangular plow
vortex generators

...nerator blade configuration.
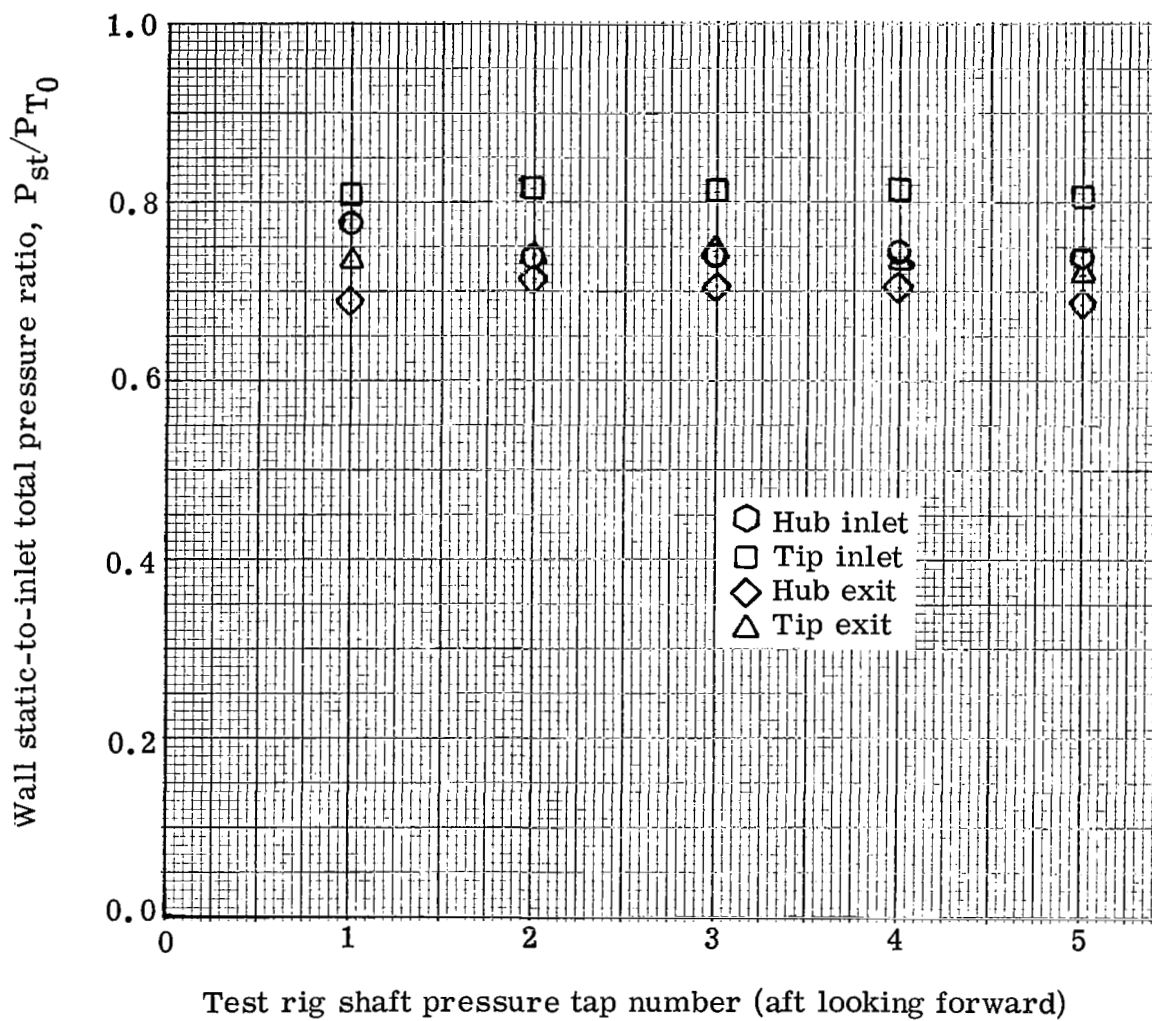
Figure 66. Circumferential variation of static pressure on inlet and exit hub and tip walls for triangular plow vortex generator blade.

5315II-66
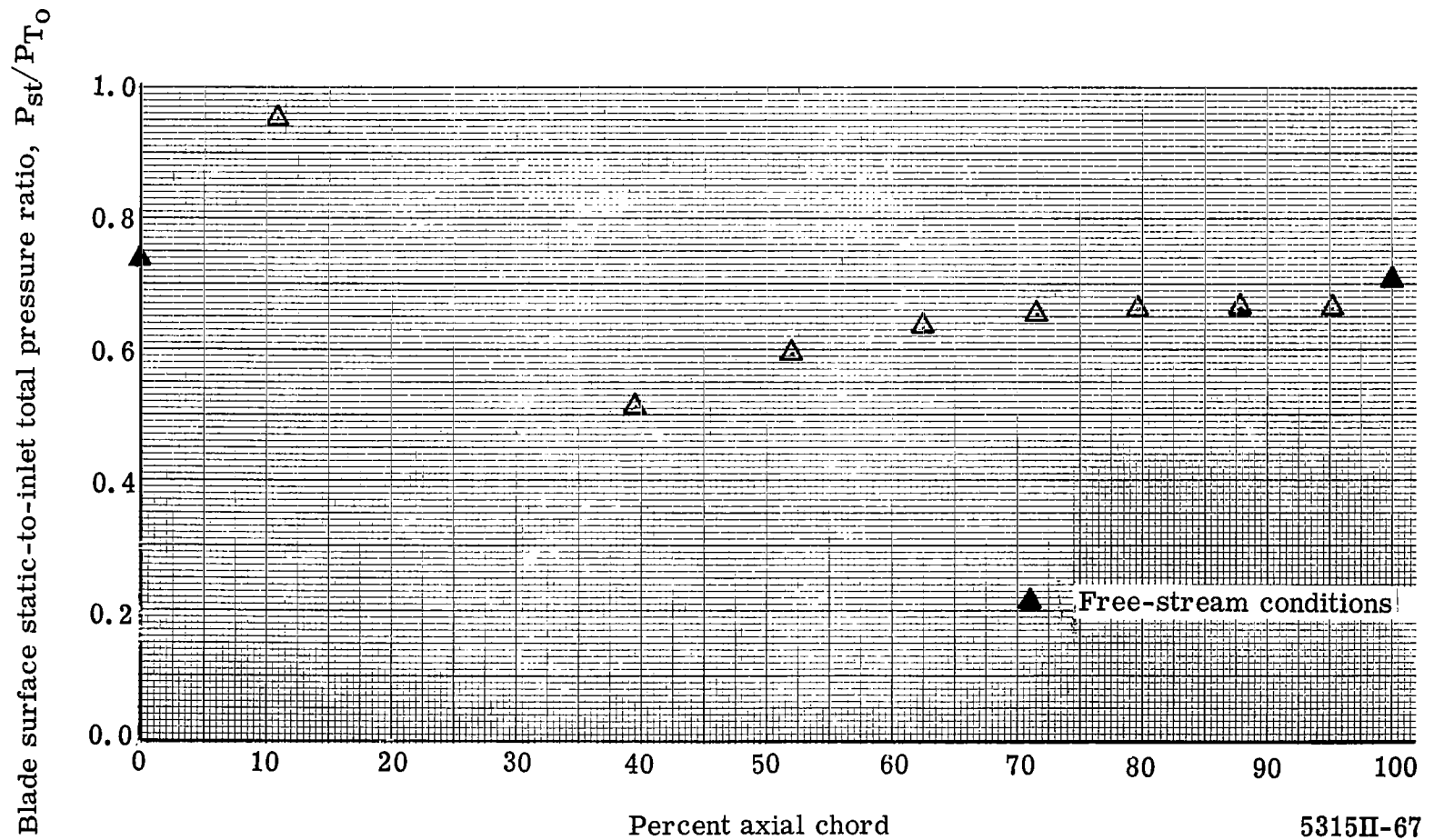
Figure 67. Measured surface static pressure distribution for the triangular plow
vortex generator blade hub section.

5315II-67
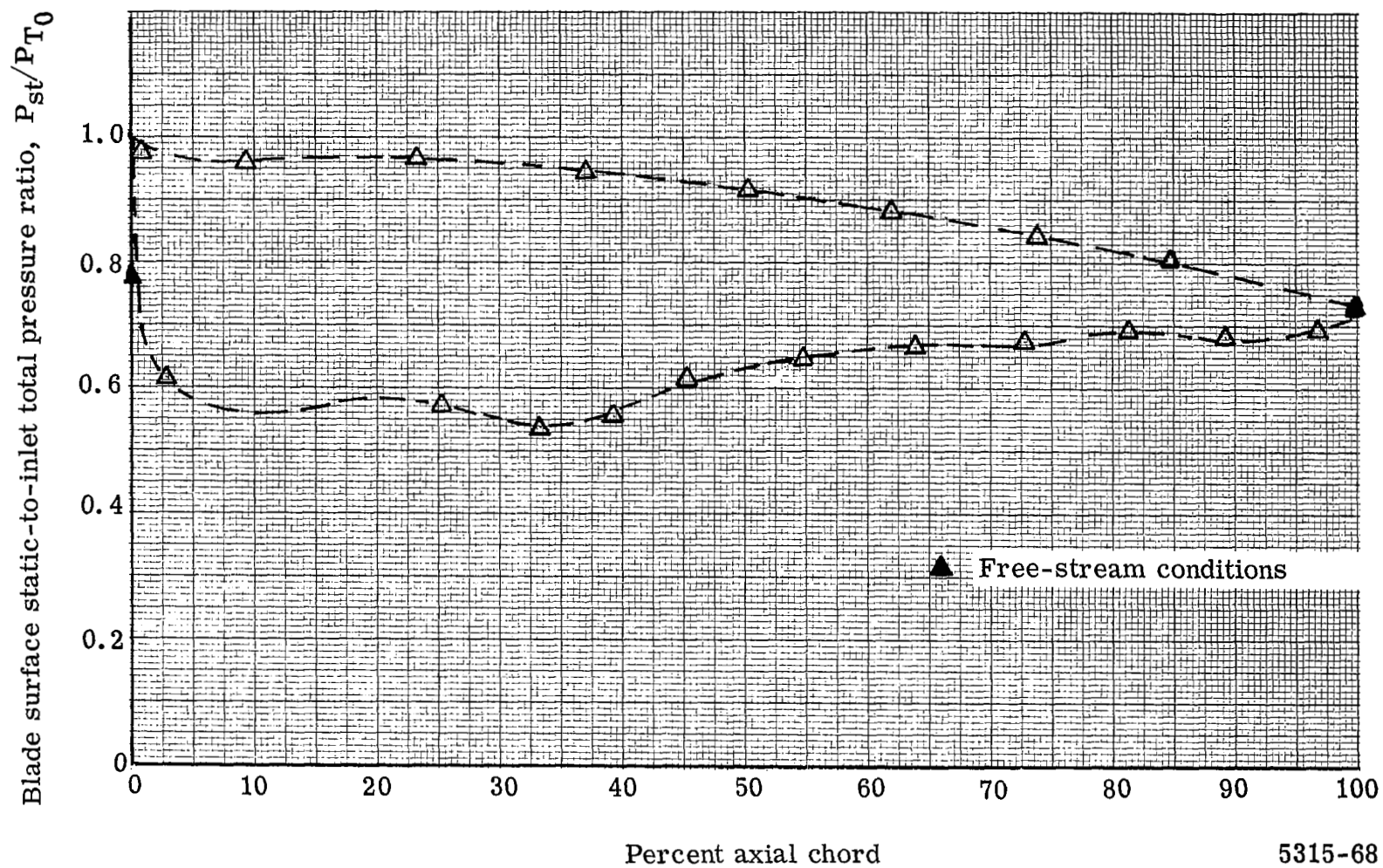
Figure 68. Measured surface static pressure distribution for the triangular plow vortex generator blade mean section.
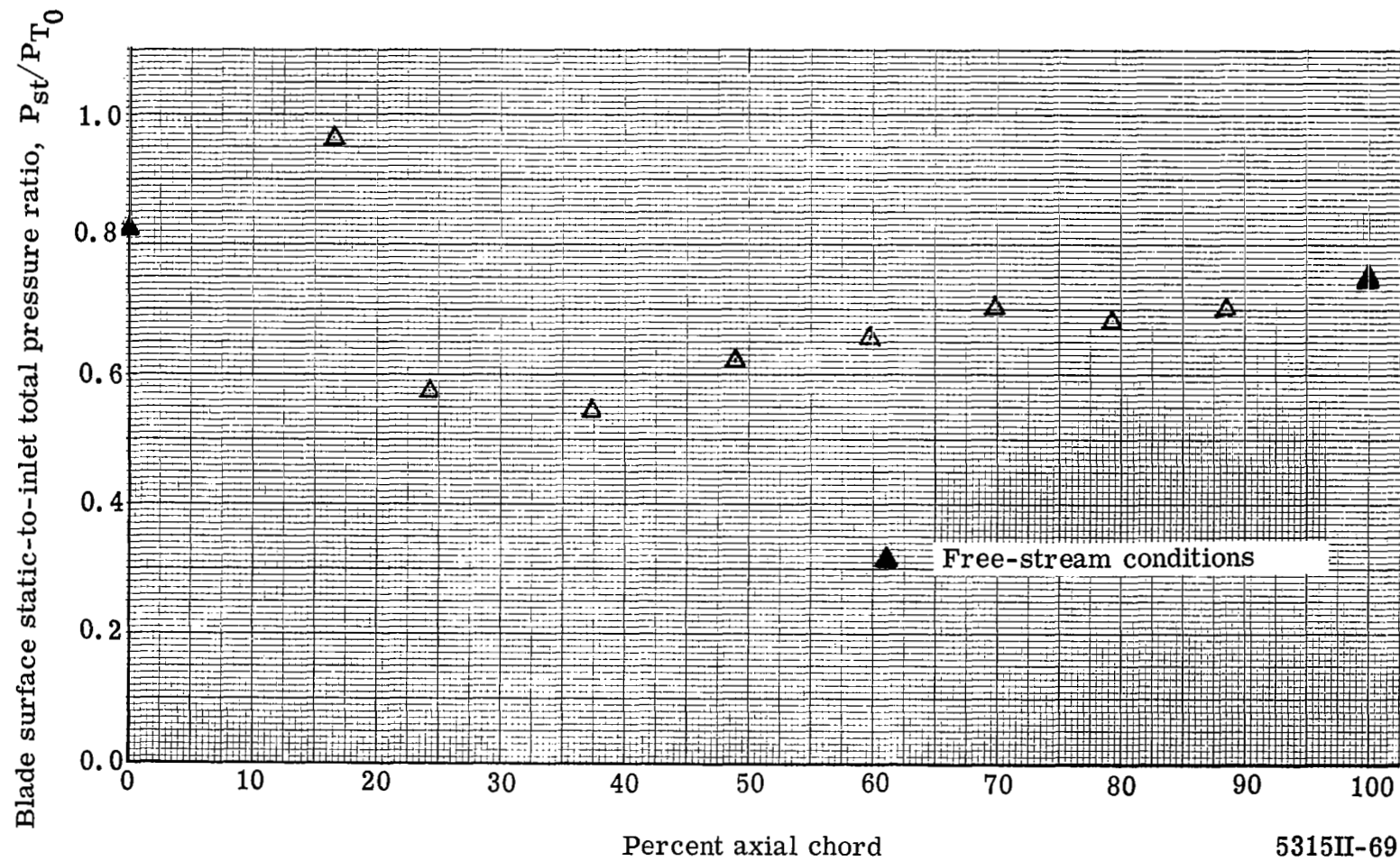
Figure 69. Measured surface static pressure distribution for the triangular plow
vortex generator blade tip section.

5315II-69

Vane No. 2
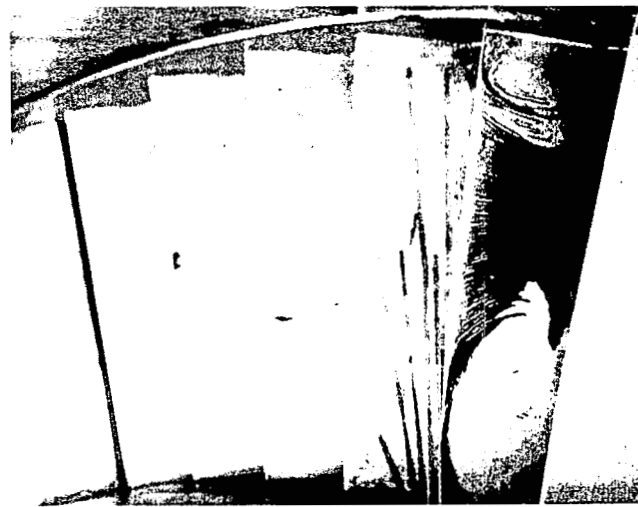
Vane No. 3

Vane No. 4

Vane No. 5

Figure 70. Triangular plow vortex generator blade flow visualization results for inlet hub static-to-total pressure ratio of 0.85 (above design value).

Vane No. 2

Vane No. 3

Vane No. 4

Vane No. 5

Figure 71. Triangular plow vortex generator blade flow visualization results for inlet hub static-to-total pressure ratio of 0.74 (design value).
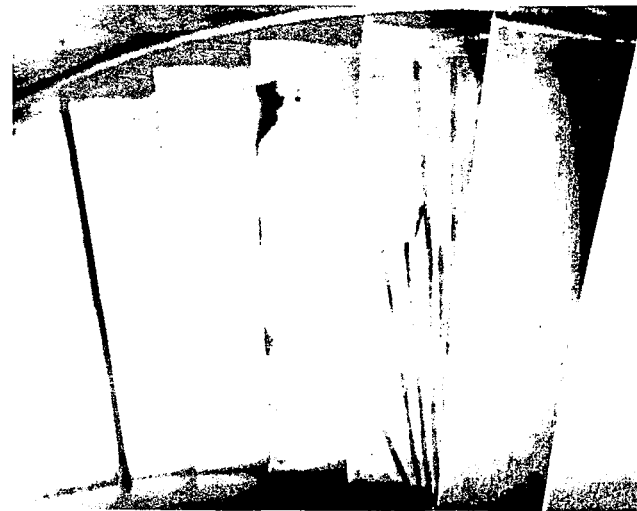
Vane No. 2   Vane No. 3
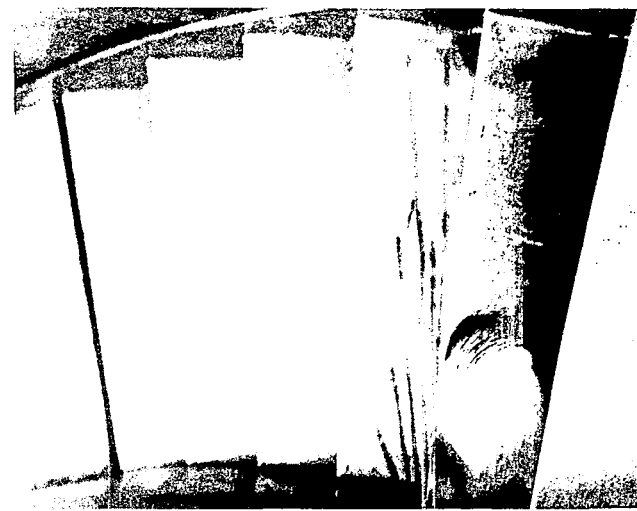
Vane No. 4   Vane No. 5

Figure 72.   Triangular plow vortex generator blade flow visualization results for
inlet hub static-to-total pressure ratio of 0. 62 (below design value).
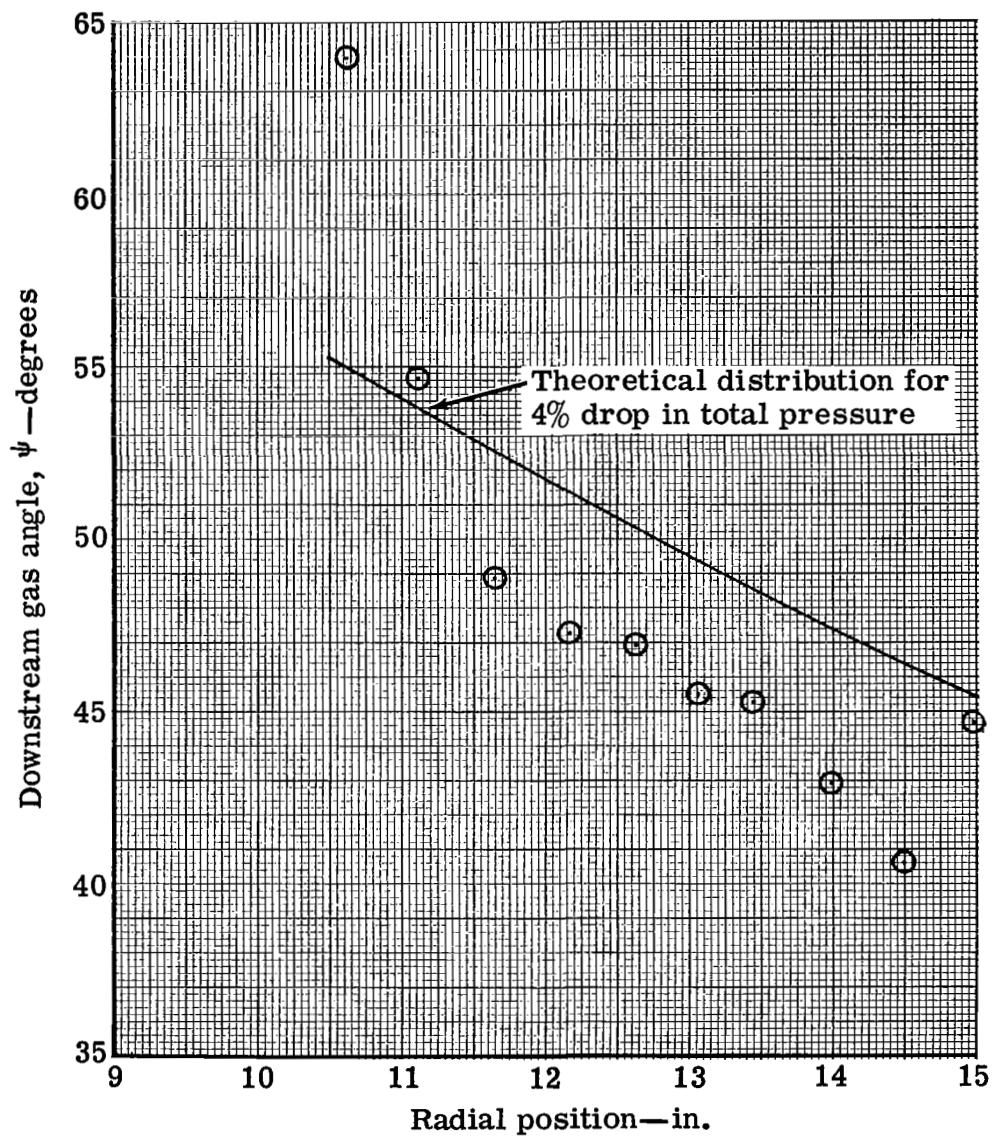
Figure 73. Measured and predicted radial variation of average downstream gas angle for triangular plow vortex generator blade.
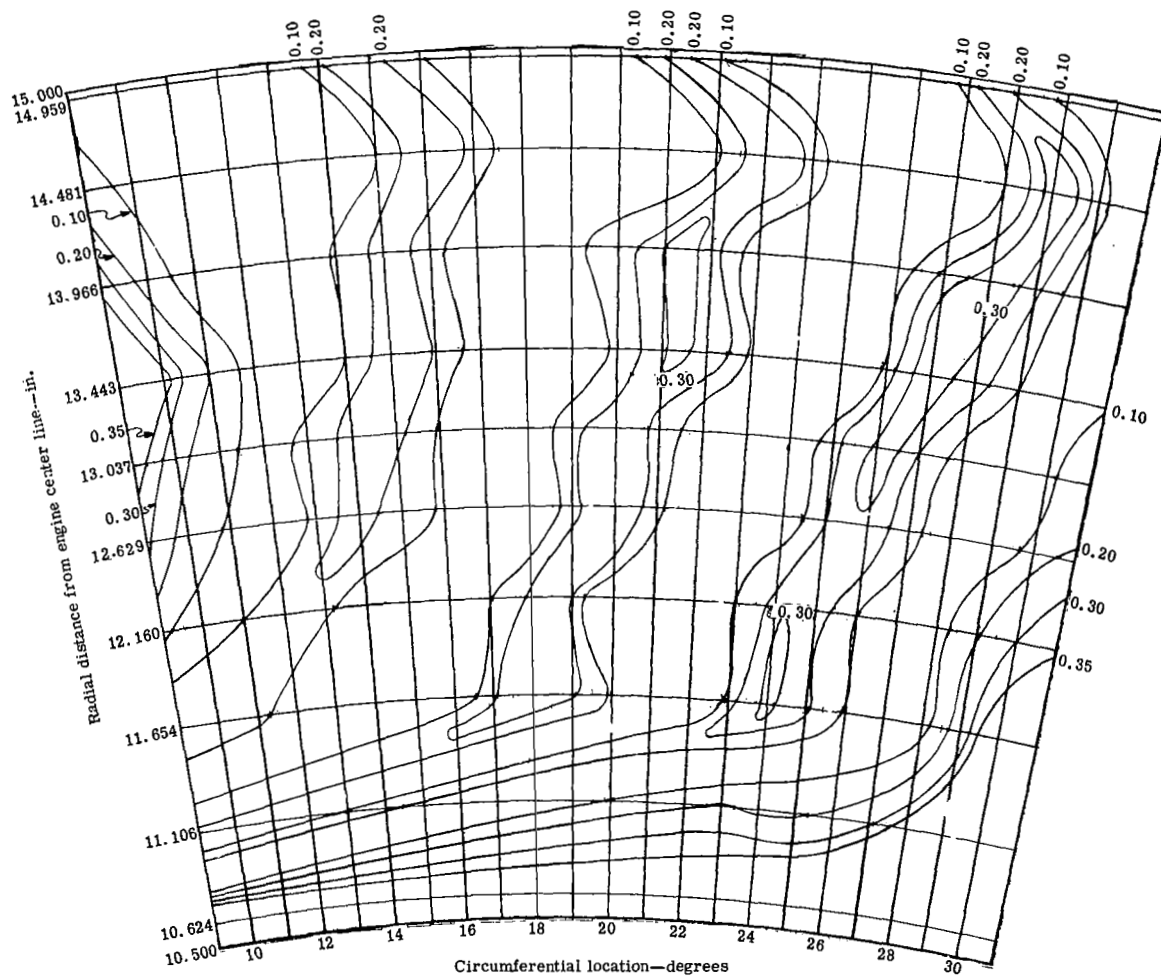
5315II-73

Figure 76. Contours of kinetic energy loss coefficient—triangular plow vortex generator downstream wake survey.
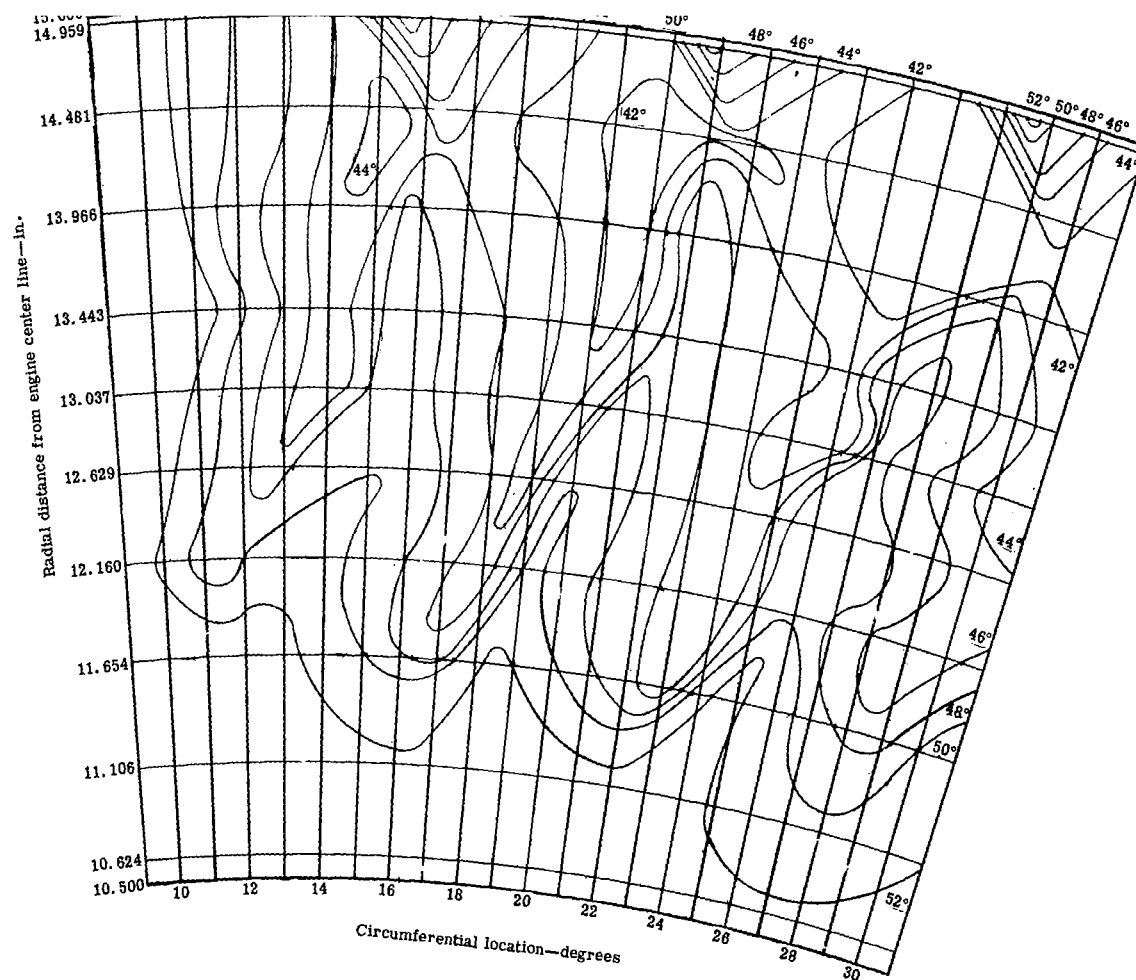
Figure 77. Contours of downstream gas angle—measured from axial–triangular plow vortex generator downstream wake survey.
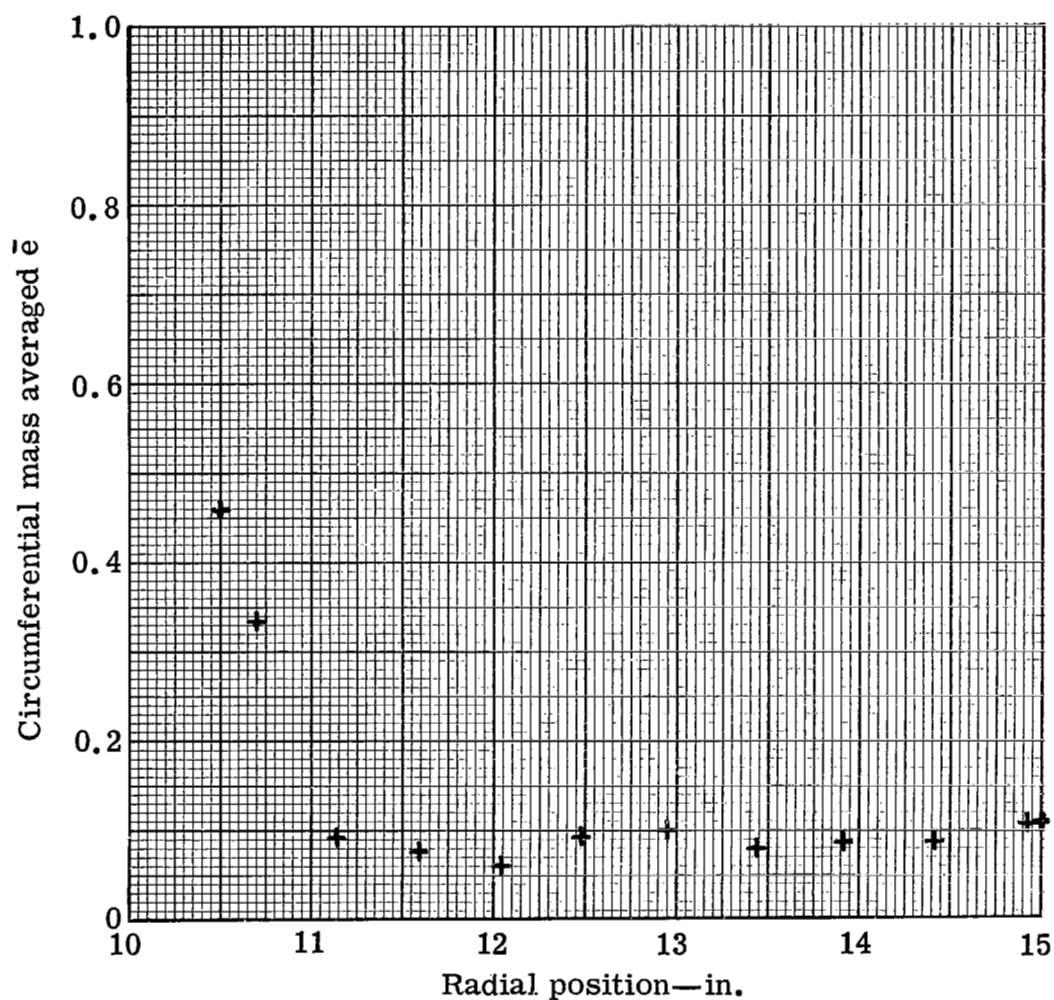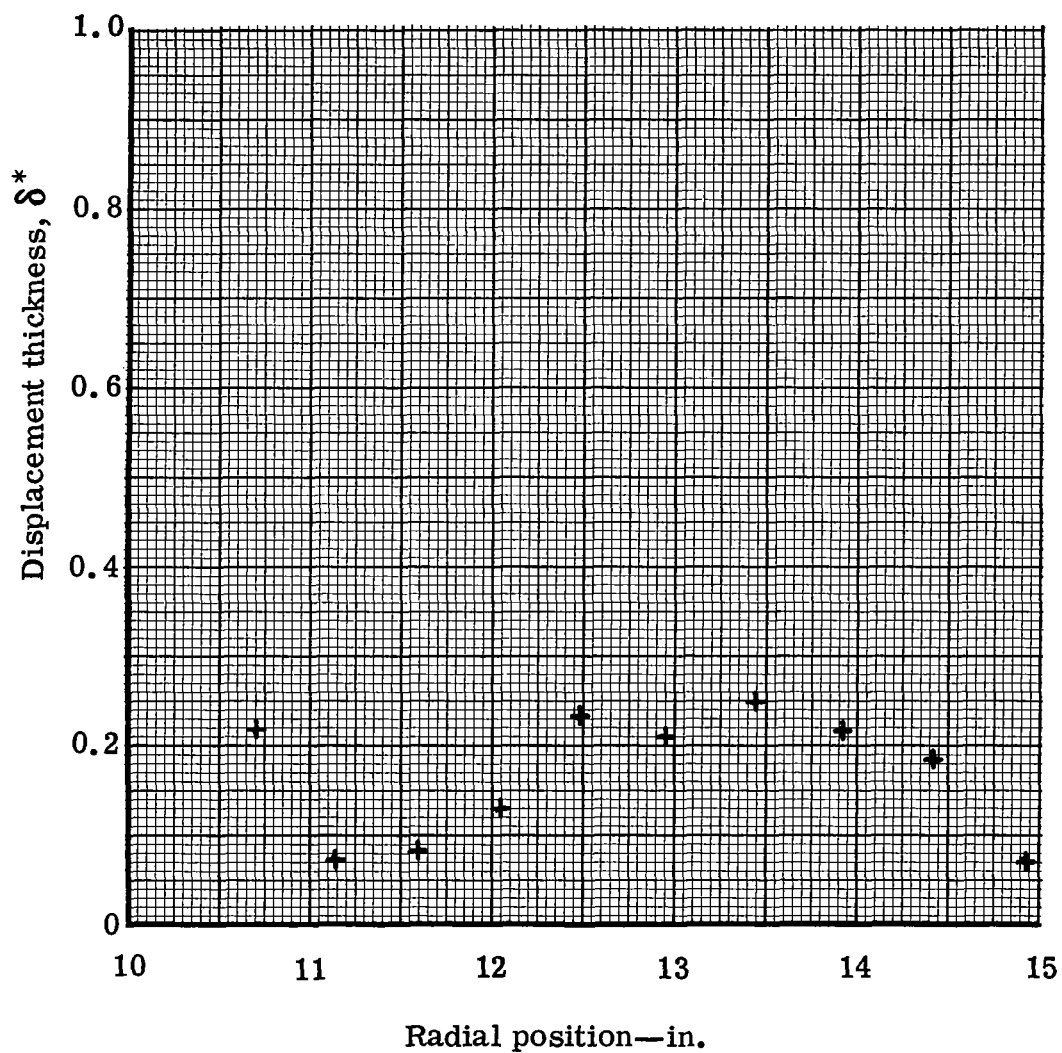
5315II-77

5315II-78

Figure 78. Triangular plow vortex generator blade exit wake
survey—kinetic energy loss coefficient
distribution at station 3.
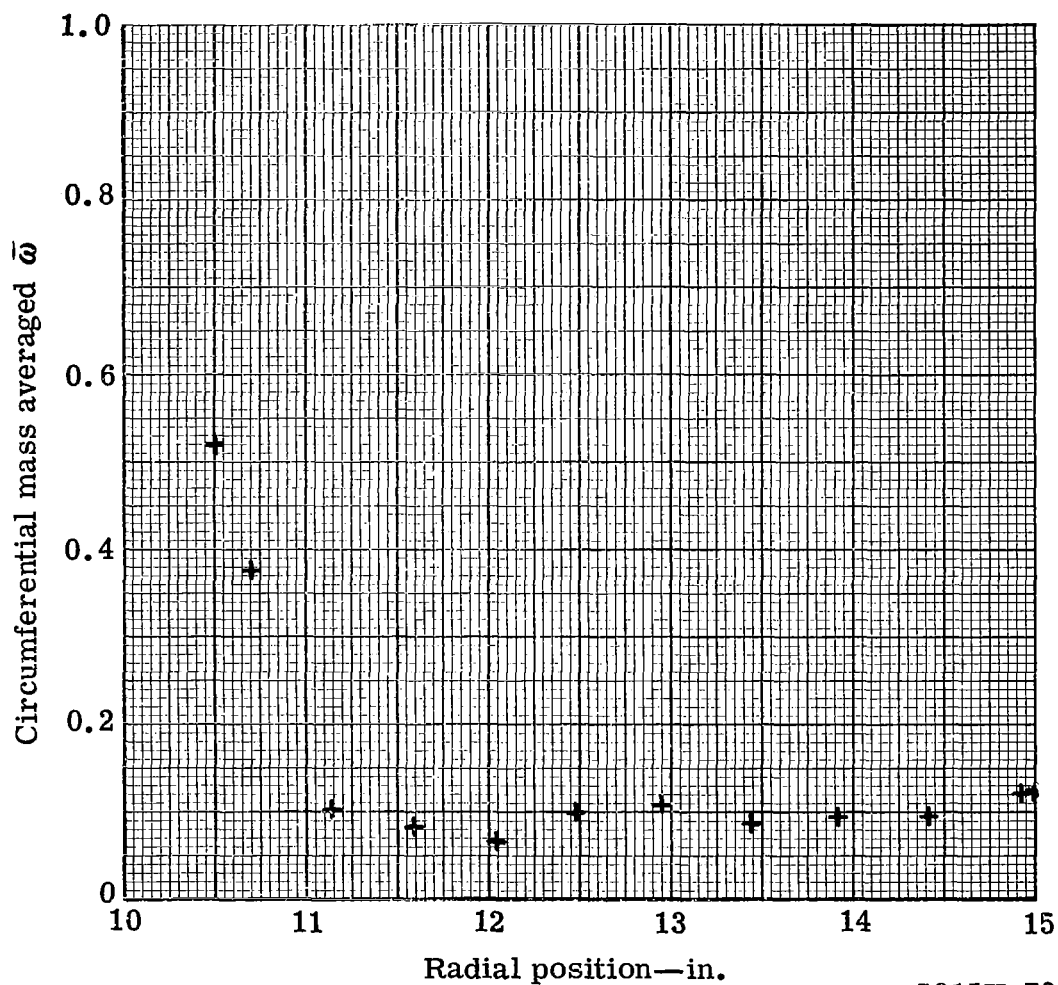
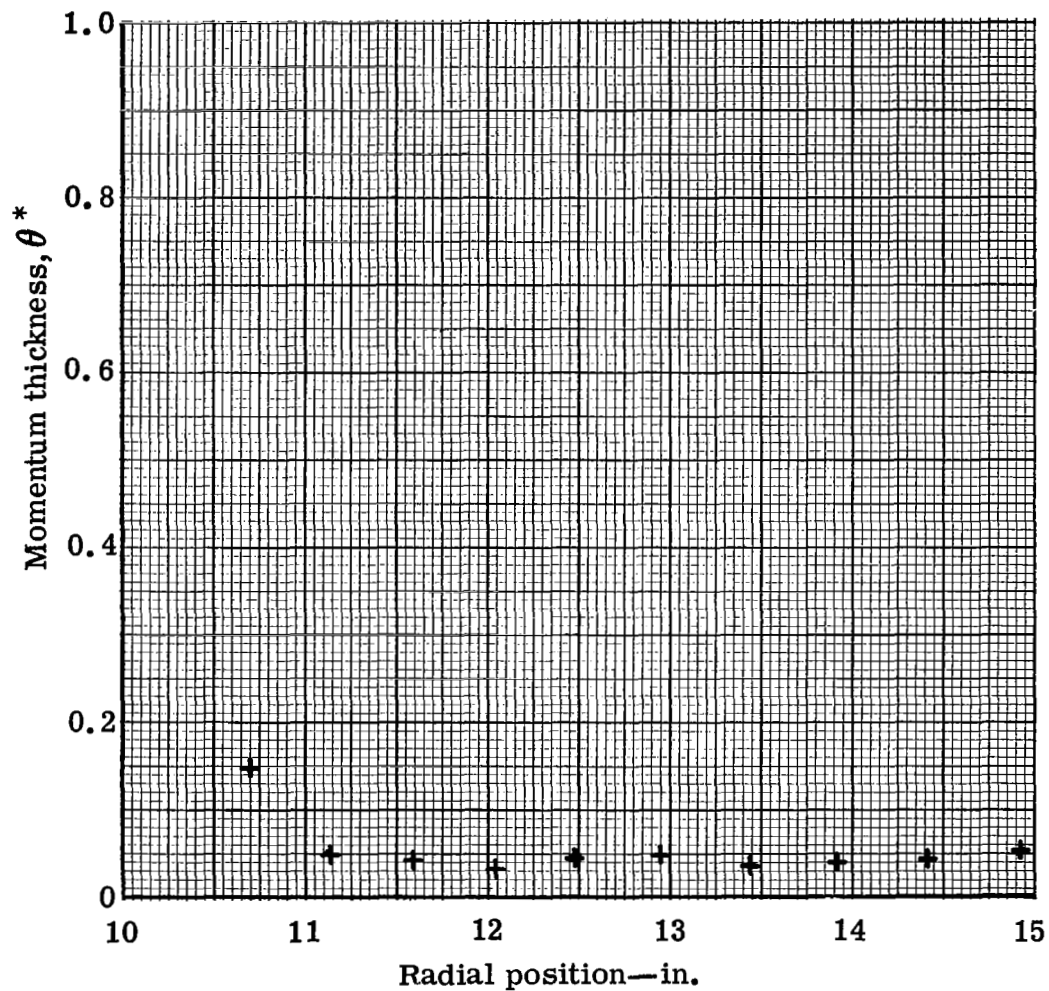Figure 79. Triangular plow vortex generator blade exit wake
survey—total pressure loss coefficient
distribution at station 3.

Figure 80. Triangular plow vortex generator blade exit wake
survey—displacement thickness distribution
at station 3.

Figure 81. Triangular plow vortex generator blade exit wake
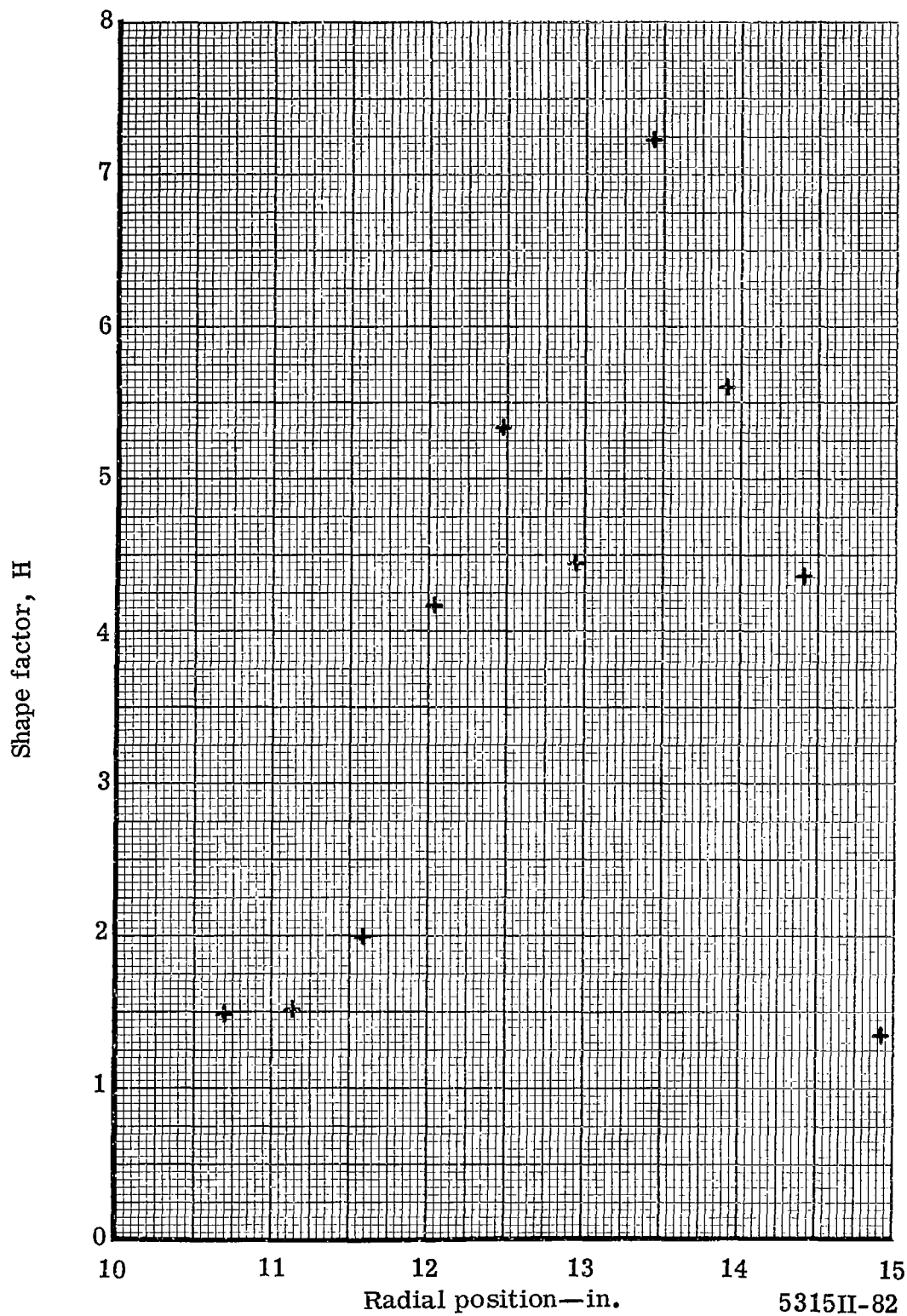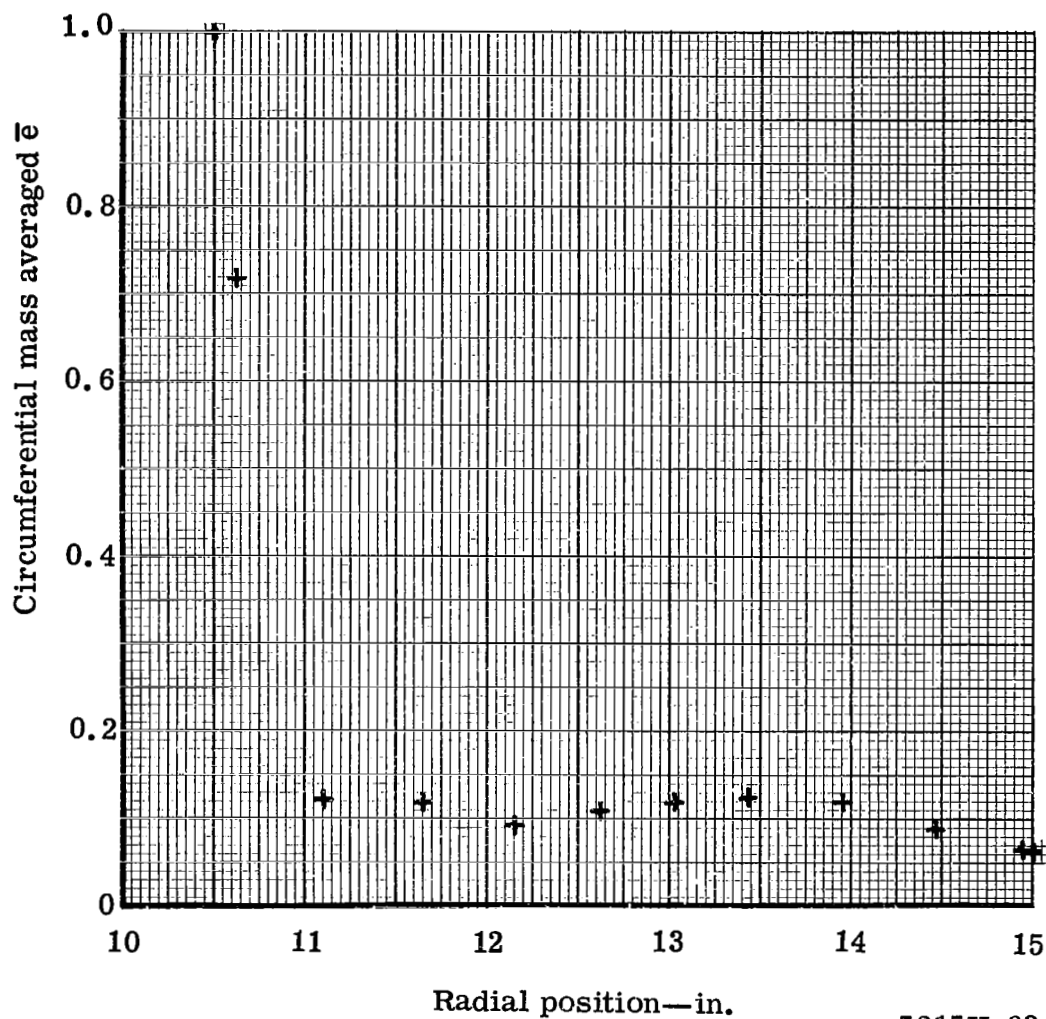survey—momentum thickness distribution
at station 3.
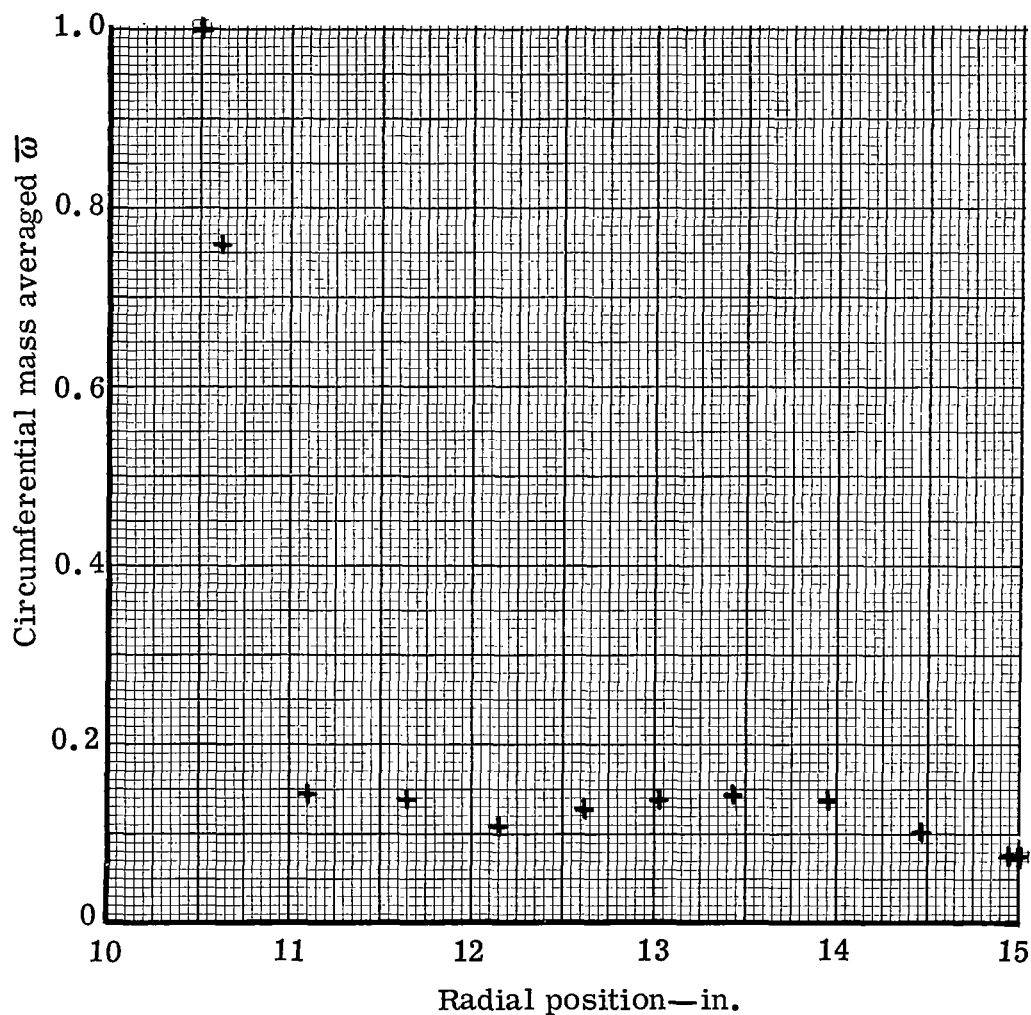
Figure 82. Triangular plow vortex generator blade exit wake survey—shape
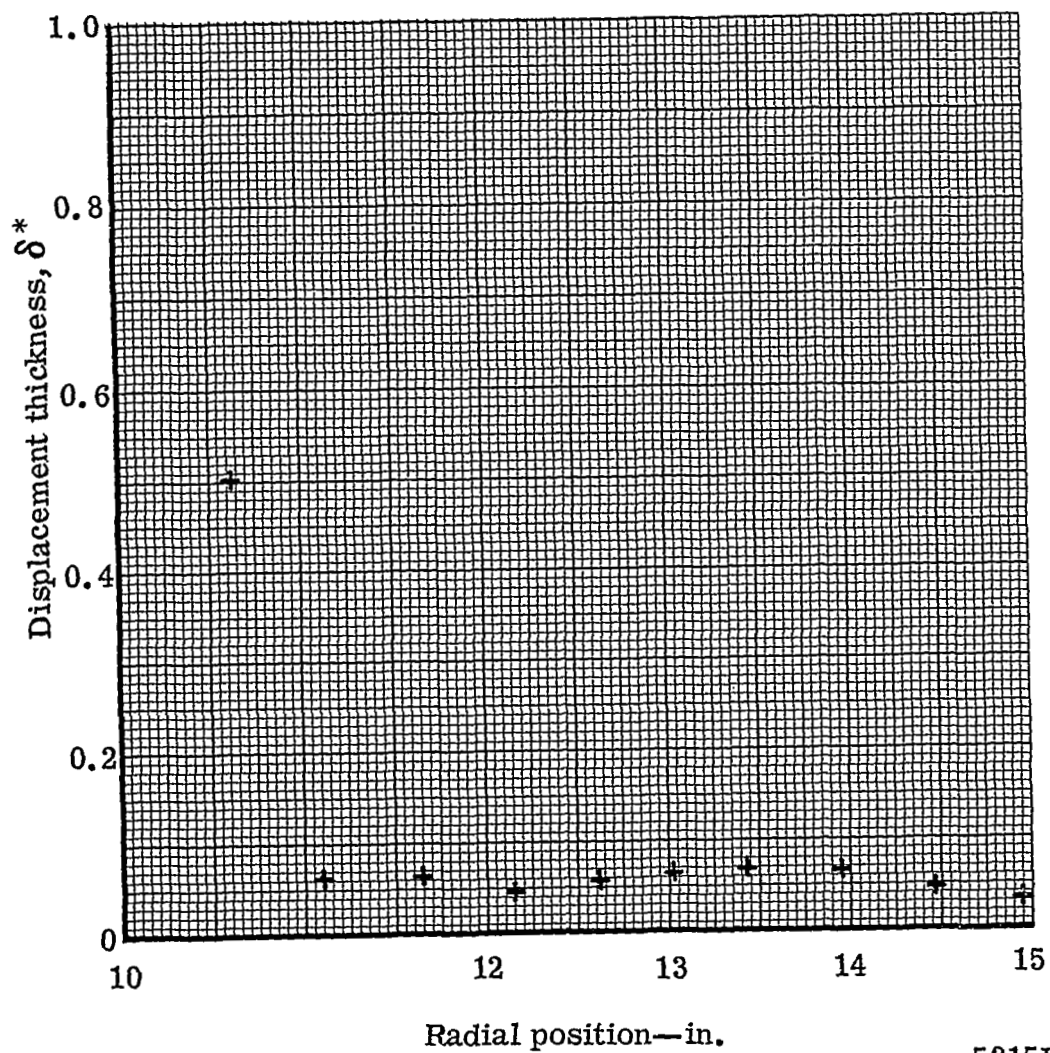factor distribution at Station 3.

Figure 83. Triangular plow vortex generator blade downstream wake survey—kinetic energy loss coefficient distribution at station 4.
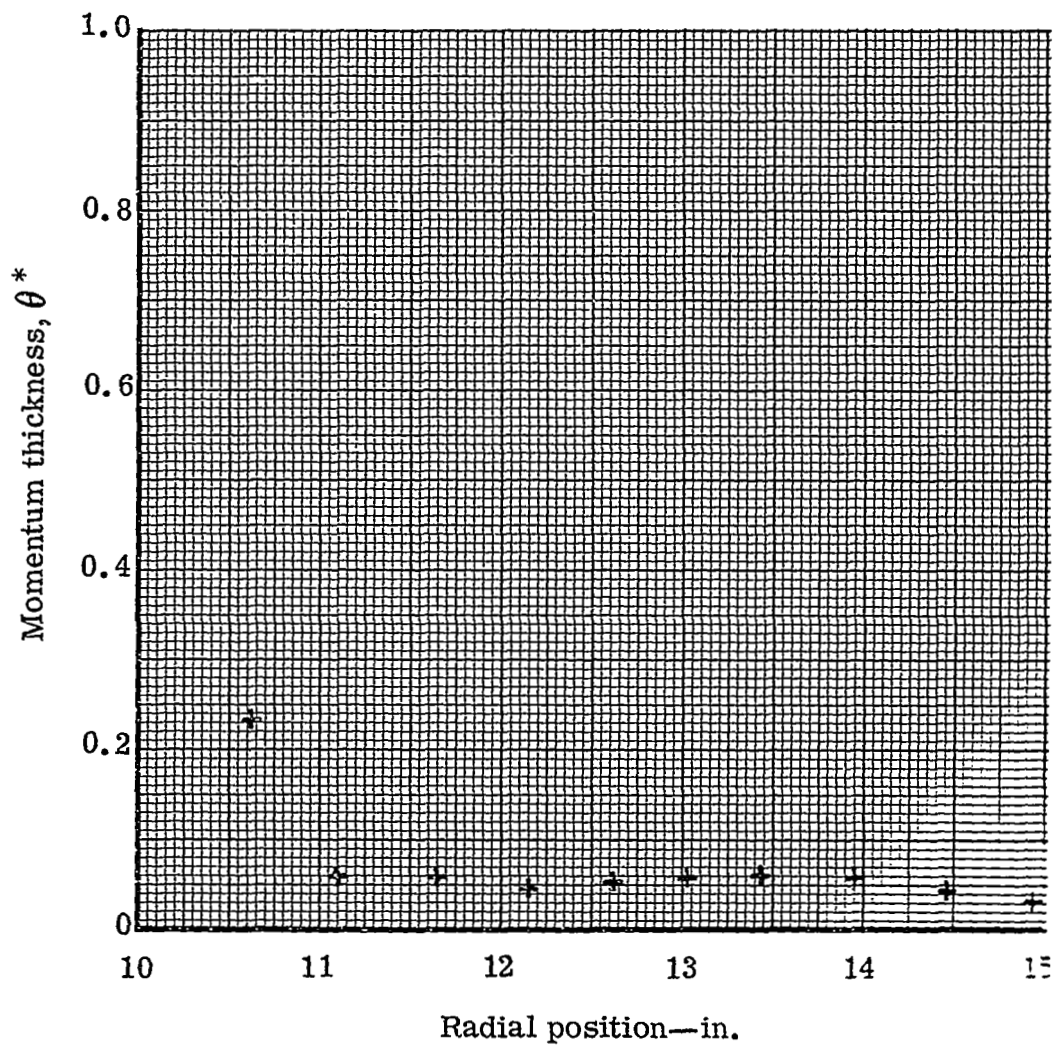
5315II-83

5315II-84

Figure 84. Triangular plow vortex generator blade downstream wake survey—total pressure loss coefficient distribution at station 4.

Figure 85. Triangular plow vortex generator blade downstream wake survey—displacement thickness distribution at station 4.

5315II-85

Figure 86. Triangular plow vortex generator blade downstream wake survey—momentum thickness distribution at station 4.
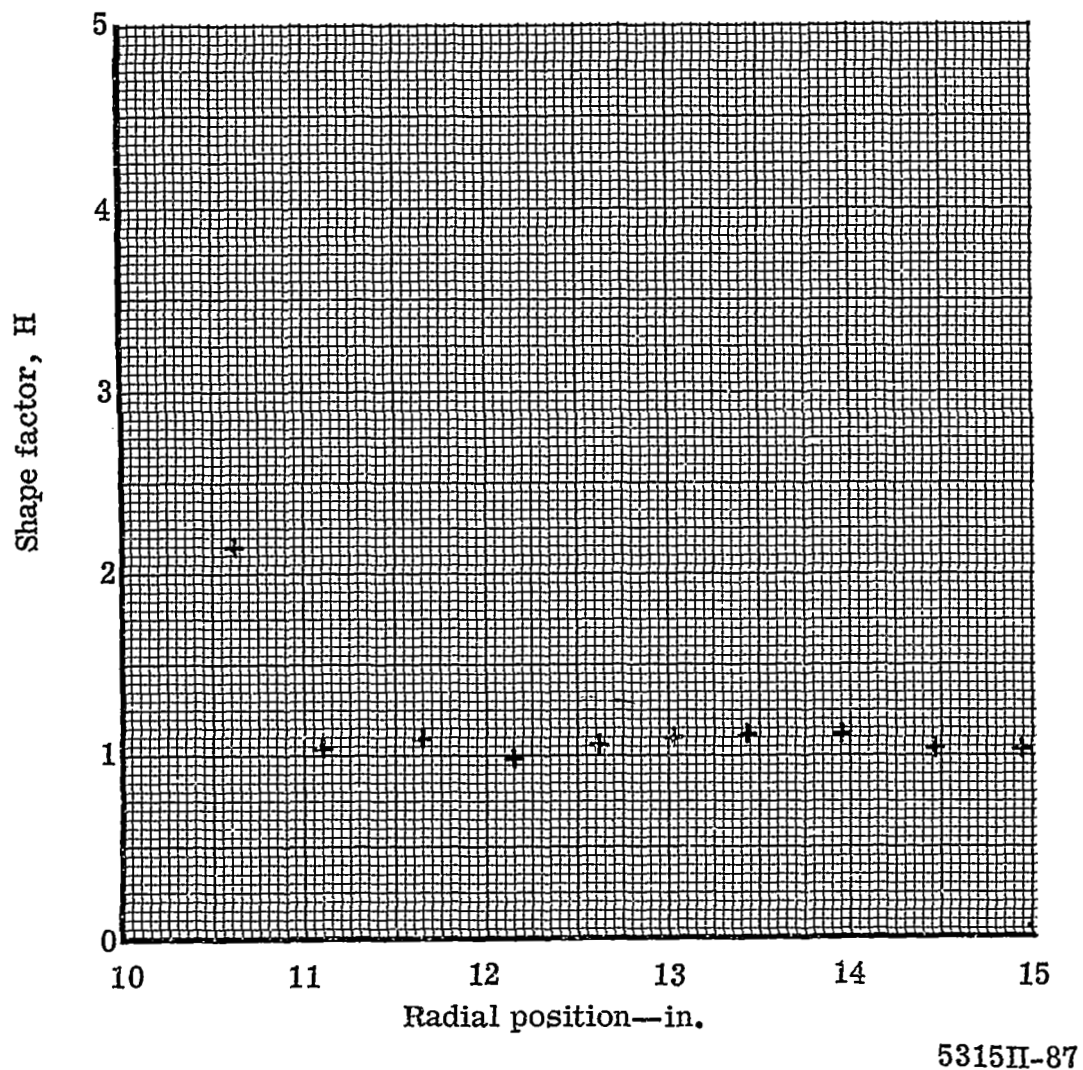
5315II-56

5315II-87

Figure 87.   Triangular plow vortex generator blade downstream wake
survey—shape factor distribution at station 4.